POLITECNICO DI TORINO

DEPARTMENT OF CONTROL AND COMPUTER ENGINEERING

Master of Science Degree in Mechatronic Engineering
MASTER THESIS

NMPC Orbit and Formation Control for the Next Generation Gravity Mission

Supervisor:
Prof. Carlo Novara

Candidate:
Patrizia Cotugno
Mat. 266790

Co-Supervisors:
Carlos N. Perez-Montenegro, PhD
Eng. Mattia Boggio
Eng. Sabrina Dionisio

ACADEMIC YEAR 2020/2021

«Remember to look up at the stars and not down at your feet. Try to make sense of what you see and wonder about what makes the universe exist. Be curious. And however difficult life may seem, there is always something you can do and succeed at. It matters that you don't just give up.».

- S. Hawking

Abstract

Since the beginning of this century, gravimetric missions have started to become one of the most interesting topics in the field of space research. The reason behind the growing attention paid to this type of missions is certainly to be found in its ambitious objective, which is the accurate measurement of the temporal variations of the Earth gravity field. As a matter of fact, the observation and monitoring of these variations could improve the understanding about some geophysical processes involving Earth's mass change phenomena, such as water cycles, glaciers formation and melting, tectonic plates displacement, etc.
The concept of Next Generation Gravity Mission (NGGM) has been proposed by ESA with the aim to raise the bar on the work started by the previous gravimetric missions, like GOCE and GRACE. Indeed, relying on the heritage gained from these two successful missions, NGGM sets its ambitious goal in the measurement of the temporal variations of the Earth's gravity field, over a long time span, with an unprecedented level of accuracy.
This thesis focuses on the formation control design, implementation, and simulation for the Next Generation Gravity Mission. NGGM formation consists of a group of two satellites, where each of them has to be drag-free controlled, in order to be ideally subject only to the gravity. The main aim of formation control is to counteract bias and drift of the residual drag-free accelerations while guaranteeing, at the same time, the long-term stability of the triangular virtual structure composed by the satellites' and Earth's Center of Masses. At this purpose, a Nonlinear Model Predictive Control (NMPC) framework for autonomous orbit and formation control is considered. The advantages of using this technique mainly consist in its ability to find an optimal control law managing at the same time state and input constraints and providing an online adaptation of the control action to possible variations of the process conditions. A key element of NMPC is an internal prediction model, used to find an optimal trajectory over a finite time interval. Here, an integrated formation control (IFC) model, based on a novel set of Hill-type equations, has been used. This model allows the description of both the formation altitude and inter-satellite distance, by defining a specific orbital reference frame called Formation Local Orbital Frame (FLOF).
The obtained results, from long-run simulations performed by means of an accurate nonlinear model, prove the validity of this control strategy and show its capability of guaranteeing the long-term stability of formation variables, although the use of a very approximated internal model and low command effort.
Further, to make a more realistic simulator, the difficulty that exists in the transmission of data between satellites is taken into account by assuming long sampling times of measurements due to the absence of a radio-frequency inter-satellite link. In this regard, the last part of this thesis is dedicated to the implementation of low-fidelity orbit propagators whose aim consists in computing, on board of each spacecraft, the companion satellite's orbit during the time intervals in which no real-time information is available. To reduce their computational complexity, these propagators approximate the effects of some forces while completely disregarding others. However, despite their simplicity, simulated results show that they well fit the proposed design scenario, without impinging the NMPC capability of guaranteeing formation long-term stability.

Contents

List of Figures

List of Tables

Chapter 1

Introduction

In the first decades of the XXI century an increasing attention has been devoted to the space gravimetric missions. The main purpose of this type of missions consists in determining with high accuracy and resolution the value of the Earth's gravity field while monitoring its changes in time and space. As a matter of fact, the Earth's gravitational field is not constant and homogeneous over the entire surface of our planet but it specifically depends on the mass distribution among all its layers. As a result, the measure of the gravity field could be an important instrument of information about the morphology and the density of all the different parts of the Earth, from its interiors to the crust, involving also the atmosphere [8]. Since the value of this measure is influenced by mass change phenomena, it results evident the reason that pushes the research to place ever greater emphasis on this type of studies. Indeed, mass changes phenomena are strictly linked with all the climate variables and their observation and monitoring enables the investigation on all those geophysical processes which involve water cycles, tectonic plates displacement, changes in the mass of ice sheets, ocean and atmosphere circulation, and so forth [15].
In order to observe mass distribution changes and transport in and between the different Earth's system layers (Atmosphere, Oceans, Hydrosphere, Cryosphere, and Solid Earth), the most direct way consists in measuring the temporal variations of the Earth gravity field over a long time span [15]. Further, thanks to this information, it is possible to develop a more comprehensive knowledge of the Earth's interior, improving applications in many disciplines such as geodesy, oceanography, glaciology, and many other fields [8],[15].
Gravity constraints the motion of Earth's satellites, both natural and artificial. Thus, studying the perturbations introduced in the orbits of artificial satellites gives us a good source of information to measure the gravitational field [8]. At this purpose, in the last 50 years different satellites dedicated to geodesy have been conceived. The first that fits inside this context is the LAGEOS (Laser Geodynamics Satellite), launched in 1976 [8]. It made use of very low altitude satellites and novel measurement techniques to provide a measure of the gravity field with good spatial and temporal resolution. Nevertheless, it is especially in the last 20 years that many steps forward have been made in this direction thanks to the progresses given by the successful European gravity missions GRACE (Gravity Recovery and Climate Ex-periment, launched in 2002) and GOCE (Gravity Field and steady-state Ocean Circulation Explorer, launched in 2009) [8].

The Next Generation Gravity Mission (NGGM) proposes itself as the heir of the missions mentioned so far as its main objective consists in the measurement of the temporal variations of the Earth's gravity field, over a long time span (namely a full solar cycle), with an unprecedented level of accuracy, both in terms of spatial and temporal resolution [10]. To accomplish its ambitious goal, NGGM makes good use of the enormous progresses made by the previous missions but also envisages the development of many technological innovations, as the usage of laser interferometry for the satellite-to-satellite tracking, and breakthrough solutions for Guidance, Navigation, and Control (GNC). In this framework, this thesis aims to make a contribution to the scientific phase of this mission by proposing an alternative strategy for the NGGM orbit and formation control.
In this first chapter, an overview about the concept of this mission and its technological heritage is presented. Further, an explanation about the control requirements and the state of art of the NGGM control unit is introduced in order to analyse the automatic control topics addressed until now and provide a good starting point to illustrate the alternative approach developed in work. Finally, the chapter ends by summarizing the main contributions given by this thesis and briefly describing how the work has been organized.

1.1 The Heritage of The Mission

Past and present gravity missions, such as GRACE and GOCE have prepared the ground for the NGGM, providing precious experience and good technological heritage for the development of the concepts on which this new type of mission is based. Specifically, GRACE has been one of the first space missions designed to track changes in the Earth's gravity field using two identical spacecrafts flying about 220 km apart in a near-polar low-Earth orbit [8], while GOCE employed a three-axis gradiometer to provide a new global and regional model of the static Earth's gravity field and valuable lessons on the drag-free system and control. In the first design phase, GOCE drag-free control encompassed six degrees of freedom with the aim to improve robustness versus the uncertainty given to environment and gradiometer response. Its design was composed by two ion thrusters for drag compensation and eight microthrusters for lateral drag and attitude control [8]. However, due to some problems, it became later necessary to move to a four degrees of freedom design, using ion thrusters for drag control and magnetic torquers for attitude control [8]. Besides GRACE and GOCE, it is worth considering in this hereditary background, also the GRACE Follow On mission (GRACE-FO, launched in 2018), whose intent was to provide continuity with the previous missions and similar quality data to those supplied by GRACE. Its contribution extended the time series of the time-variable gravity field initiated by GRACE by using the Laser Ranging Interferometer for the measure of the inter-satellite distance variation and consequently of the temporal variations of the Earth's gravitational field [1],[19].
Since 2003, the European Space Agency (ESA) has proposed some new initiatives in the gravimetry field, opening the way to the NGGM. The main objective of NGGM is the long term monitoring of the time-variable gravity field with unprecedented temporal resolution (weekly or better) and spatial resolution (comparable to the one provided by GOCE), possibly covering a time span of a complete solar cycle [10].

1.2 The Next Generation Gravity Mission

Since the objective of the Next Generation Gravity Mission is to measure small variations of the Earth's gravitational field, the most suitable technique resulted to be the low-Earth orbit satellite-to-satellite tracking (SST) [14]. This technique, illustrated in Figure 1.1, foresees the use of two satellites flying in loose formation such that it is possible to obtain the measure of the gravity field temporal variations simply by monitoring the inter-satellite distance fluctuations induced by gravity anomalies. The satellites are equipped with an optical link between them, capable to determine the acceleration differences [10].

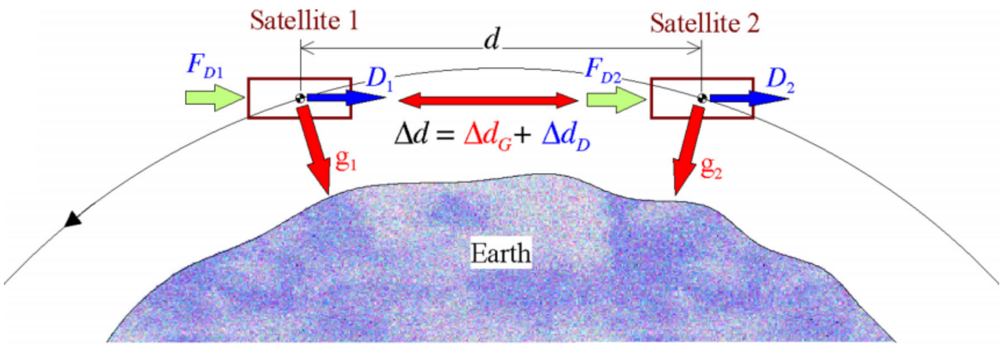

Figure 1.1: Principle of the SST Technique [8]

Following these main principles, the NGGM will consist in a formation of a pair of satellites, placed in a near-polar orbit at an altitude between 300 and 450 km. In order to take in consideration only the gravity acceleration component, all the non-gravitational terms need to be cancelled. Thus, each satellite must be controlled to be drag-free in order to counteract the atmospheric disturbances, the solar pressure and others unknown effects, making in this way the satellites ideally subject only to gravity force [11].
At this purpose, the first NGGM requirement consists in the development of a drag-free control algorithm able to remove all the non-gravitational accelerations. A second requirement concerns the orbit and formation control, needed to counteract bias and drift of the drag-free residual accelerations which can cause the divergence of the satellite formation [11]. Finally, one last requirement refers to the attitude and pointing control system which is needed to guarantee the alignment of both spacecrafts' optical axis to the satellite-to-satellite line with a micro-radian accuracy, and to ensure an orbital roll motion for tracking the Sun beam [11]. As already specified, this thesis work deals in particular with the second mission requirement, that is the orbit and formation control. Generally speaking, the expression "formation" refers to a group of cooperating satellites which perform their mission objectives working together and realizing their tasks in place of a unique, bigger, spacecraft [10]. The innovation of NGGM concept consists precisely in its objective of realizing a drag-free formation flying mission. Its formation is composed by two satellites, flying in a low-Earth orbit and acting as proof-masses immersed in the Earth's gravity field. This pair of drag-free satellites, placed at a certain distance, acts as a sort of gradiometer with a very long baseline [11].
The simplest mission scenario consists in a single pair of satellites flying on the same circular orbit with different true anomalies. This type of formation is called “in-line” or “pearl

string" formation [8] and is illustrated in Figure 1.2 (a). For the specific mission under assessment, a near-polar orbit has been considered as the most suitable to avoid blind spots around the poles in the geographic coverage [10]. With the in-line formation, the gravity field is sampled only in the tangential (along-track) direction and the measurements of gravity field are more sensitive to variations in the North-South direction then in Est-West direction, that implies an anisotropic signal structure [8].
Other possible, but more complex, types of formations are the Pendulum Formation and the Bender Constellation. In the following, we briefly explain the principles of these other two types of configurations but, for the sake of simplicity, in this thesis we will always refer only to the in-line formation as some latest studies have identified it as the best option [10]. The Pendulum Formation (Figure 1.2 (b)) foresees two satellites flying on two slightly separated but intersecting orbits characterized by different inclination or right ascension of the ascending node (RAAN) [11]. The advantage of this configuration consists in its ability to capture both along-track and cross-track gravity signals, but this benefit is counterbalanced by the additional design complexity and the particular spacecraft payload needed. Moreover, the only possibility to increase the temporal resolution of the gravity field monitoring consists in the addition of more satellite pairs to the constellation [8].
Finally, the Bender Constellation, depicted in Figure 1.2 (c), is composed by two pairs of in-line satellites, flying on circular orbits with polar and medium inclinations [3]. Its advantage is to be found in the fact that it allows a significant reduction of spatial and temporal aliasing and anisotropic errors by sampling the gravity fields in both North–South and East–West directions with an higher temporal frequency. Even in this case, the results can be further improved by enlarging the basic constellation with other satellite pairs.
In NGGM, the minimum altitude at which the formation can fly depends on its long-time duration (at least one solar cycle, i.e 11 years), propulsion performance and spacecraft mass (limited by the requirement of guaranteeing a dual launch by a small rocket) [8]. By analysing these constraints, it was estimated that the lower limit for the in-line formation is about 340 km of altitude, considering also that the lower the altitude, the higher the drag acceleration to be compensated, implying a more significant spacecraft power demand and propellant load [8].

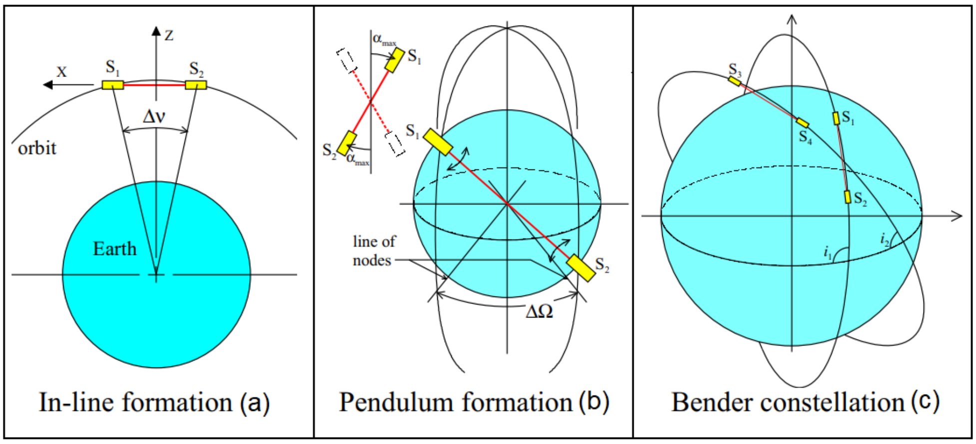

Figure 1.2: Satellite Orbital Configurations for NGGM [8]

1.3 The Mission Technology

For what concerns the technology used to satisfy the established requirements, numerous sensors are involved. The drag-free control requires one or more ultrasensitive accelerometers (as the ones tested in GOCE) in order to provide both linear and angular accelerations; the formation control makes use of a global navigation satellite system (GNSS) to provide the satellite position and velocity and, finally, the attitude and pointing control involves an inter-satellite laser interferometer and other optical sensors capable to provide the measure of the satellite-to-satellite mutual alignment variations [11]. The design of the laser ranging system, whose main task is the measure of the satellite-to-satellite distance fluctuations, is precisely driven by the inter-satellite distance [8].
The optimal nominal distance between the two satellites has been chosen equal to 100 km noting that the laser ranging noise increases with the distance [9]. Further, up to about 100 km, it is possible to adopt the Michelson-type heterodyne laser interferometer, designed and tested by Thales Alenia Space (TAS) in cooperation with the Italian Metrology Institute (INRIM). This kind of interferometer is based on a simple retro-reflector scheme and is adapted for long distance operations by using a 500 mW laser source [8]. The retro-reflector scheme acts by passively back-reflecting on one satellite the laser beam coming from the other one [18]. It is possible to cope with eventual failures by endowing both spacecrafts with the same metrology apparatus and exchanging the position of the two satellites [8]. Above 100 km distance, the retro-reflector concept can be replaced with the offset phase-locked transponder configuration, already tested on the GRACE-FO mission, based on the Laser Interferometer Space Antenna (LISA) [16]. Here, the laser beam generated on one satellite, is received by the other satellite, which makes use of its own laser source, phase-locked to the incoming beam, to regenerate and retransmit the laser beam back to the first satellite [8],[15].
Besides the laser interferometer, TAS and INRIM have also developed an auxiliary optical metrology system for driving the laser beam pointing and simplifying the acquisition of the optical link between the two spacecrafts [8]. This metrology system is composed by three optical heads, each one endowed by a large field of view and equipped with position sensors. Thanks to these optical heads, it is possible to measure the direction and the intensity of the incoming laser beam and reveal the lateral offset of the companion spacecraft with respect to the beam centre, by sampling the intensity of the incoming laser beam at three different points [8].
For the retro-reflector design, the set of sensors used to measure the non-gravitational accelerations makes use of the heredity left by GOCE, leveraging a system composed by four and two accelerometers for measuring respectively the linear non-gravitational accelerations and the angular accelerations about each axis [17]. These accelerometers are arranged around the optical bench of the laser interferometer such that the midpoint of the line connecting two opposite accelerometers is placed at the satellite CoM [8].

1.4 State of Art

This section is aimed at providing an overview about the most important scientific literature regarding the topics on which this thesis work is focused. The research arguments here presented are a good starting point to introduce the alternative approach developed for the NGGM formation control. At this purpose, the topics addressed in the following subsections aim at introducing in the reader a general knowledge about the organization of the overall NGGM control unit and to describe the Embedded Model Control (EMC) methodology, namely the control technique adopted in the current control unit.

1.4.1 The NGGM Control Unit

The system to be controlled, namely the plant, is the entire NGGM spacecraft formation, whereas the digital control unit concerns the NGGM AOCS, that accounts for attitude, formation and orbital control systems.
The NGGM control unit, illustrated in Figure 1.3, is organized in a multi-hierarchical structure where the orbit/formation together with the attitude/pointing controls represent two narrow-band outer loops whose aim is to provide the reference accelerations to the drag-free control, which constitutes a wide-band inner loop [10]. It is worth noticing that,

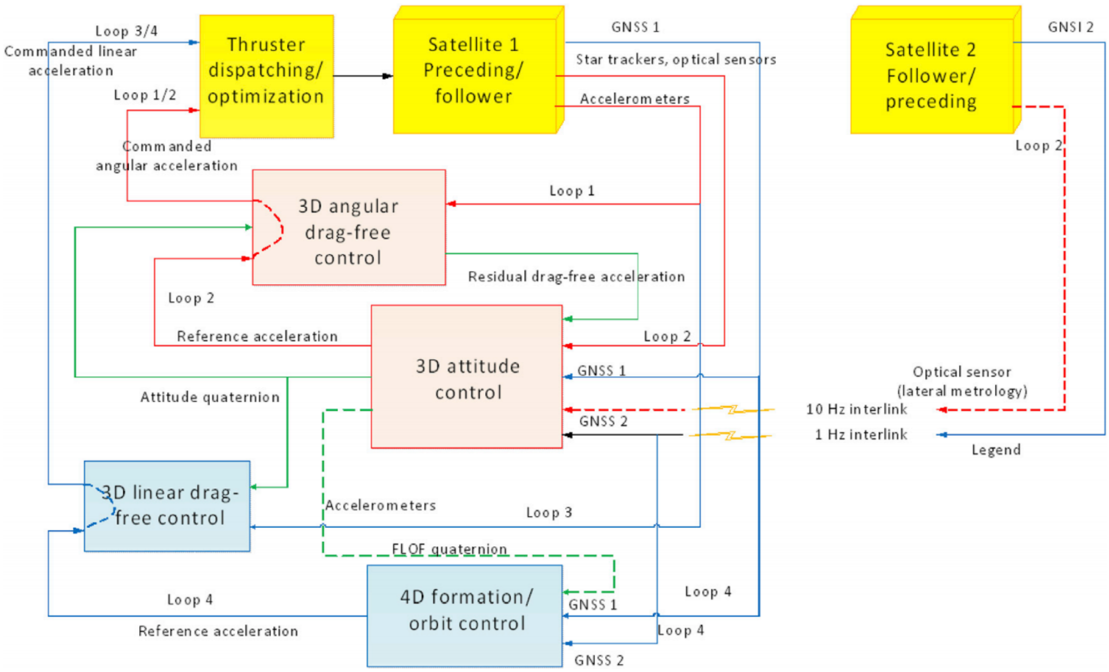

Figure 1.3: Block Diagram of the NGGM AOCS Architecture [11]

drag-free and attitude/formation controls should be actuated at different bands in order to avoid any possible interference between the different loops [11]. The current design of the NGGM AOCS relies on few important principles. First of all, the orbit and formation control is based on the definition of the so-called triangular virtual structure, that is in the system composed by the two satellites' and the Earth's center of masses (CoMs). This new modelling idea leads to the formulation of new CW-type equations through which to describe both the formation altitude and the inter-satellite distance [10]. Secondly, drag-free control is intended to make each satellite ideally affected only by local gravity. It is

possible to distinguish the linear drag-free, which aims at zeroing the non-gravitational accelerations, and the angular drag-free, whose purpose is to cancel the disturbance torques, such as gyrocopic effects, gravity gradient and aerodynamic torques [10]. Each satellite is controlled to be drag-free using the accelerometer concept that envisages the presence of free-falling masses actively suspended and maintained centred in a cage by means of an active suspension system. The measure of the non-gravitational effects to be zeroed by drag-free control is obtained from the value of the suspension force. At this purpose, NGGM drag-free control system adopts three pairs of proof-masses disposed in an orthogonal way in order to form a 3D gradiometer [10].
Notwithstanding, some secular (low frequency) residual accelerations will always affect the satellites orbit due to accelerometer errors. At this purpose, besides constraining the relative position of the two satellites, a second important objective of formation control is to counteract the bias and drift of the residual drag-free accelerations [11].
From the sensor and actuators point of view, the formation control is fed by the measurements coming from the GNSS, which are influenced by the differential acceleration and consequently by the differential gravity, namely the objective of this mission.
As above mentioned, the third part of NGGM control unit is composed by the attitude and pointing control system, whose aim is to guarantee the alignment of the satellites optical axis with the satellite-to-satellite line [11]. The control action is obtained disposing of proper optical sensors aimed to measure mismatch of the satellite's optical axis from the inter-satellite line [6]. Further, the pointing control has to be coordinated with the angular drag-free control, since this last constraints the frequency of pointing control by setting on it an upper bound [11].
Each satellite is equipped with the same optical metrology, whose sensors are able to measure the pitch and yaw tilt of the laser beam coming from the other satellite and with the same attitude sensors, such as Sun and Earth sensors and star trackers. In addition, the actuation system exploited by attitude/pointing control is the same that accounts for linear drag-free control, which is composed of eight small proportional thrusters, capable of few milli-Newton thrust [10].
The overall current control unit designed for NGGM mission makes use of the Embedded Model Control (EMC) methodology, described in the following section.

1.4.2 Embedded Model Control

The Embedded Model Control is an efficient and robust technique for model-based design. Its main advantage consists in the capability of stabilizing systems affected by parametric and structural uncertainties [4]. For this reason, this methodology seems one of the most suitable techniques to address the NGGM control problem using a very approximated model, namely the IFC model.
According to the Embedded Model Control, it is possible to distinguish three levels of models [4]:

1. The fine model, which is the more refined level, replaces the satellite systems and external environment and is composed by a mix of hardware and software components, written and coded by means of both continuous time (CT) and discrete time (DT) equations [10].

2. The design model, which is the DT conversion of the fine model, is formed by the controllable dynamics (to be included in the Embedded Model) and the neglected dynamics. The controllable dynamics encompasses three different types of disturbance signals: known disturbances that are not needed for controllability purposes, unknown disturbances that influences parametric uncertainty, and unpredictable disturbances due to causal uncertainty [10],[4].

3. The embedded model (EM), which is the real-time realization of the design model, is coded and embedded inside the control unit which runs in parallel with the plant [11]. Here the neglected dynamics is not considered, and no parameter estimation is performed, as the unknown disturbances are seen as part of the unpredictable disturbances [4].
   The EM is written with DT state equations online updated by command and noise in order to keep the controllable and disturbance state variables active, as they are the most relevant source of command synthesis [4]. The Embedded Model consists of the controllable dynamics developed in the design model and the disturbance dynamics, which allows to treat all the model errors, non-linear effects and parameter uncertainties as disturbances with a totally stochastic and parameter-free dynamics[10].

The EMC allows to proceed in a systematic way from the fine plant dynamics and control requirements to the Embedded Model, which is the central part of the control algorithm. As mentioned above, this technique is based on the interconnection of three parts: the controllable dynamics, the disturbance dynamics and the neglected dynamics. The first two parts are intended to be observable from plant measurements in order to derive the control algorithm, while stability and performance are influenced by the third part [4]. Consequently, the main design issue is to distinguish between driving noise and neglected dynamics, in order to perform disturbance update and rejection [4].
From a practical point of view, disturbance dynamics is obtained by means of pure DT integrators combined together and driven by arbitrary signals in order to obtain random drifts. This processes are non-stationary but their finite-time realization however encompass those of stationary processes with variable time constants longer then the realization time-span. In this way it is possible to obtain simple parameter-free models defined only by the number of integrators and their typology[4]. In addition, the disturbance dynamics is driven by a disturbance input which is retrieved in real-time from the model error (given by the difference between plant output and model output). For noise estimation is used an output-to-state feedback state observer, whose corresponding algorithm is called Noise Estimator (NE). This last, when closed around the Embedded Model takes the form of a state predictor and together with a reference generator, constitutes the Measurement Law[10].
The overall EMC architecture includes two main sets of feedback channels [4]:

1. The output-to-state feedback of the Noise Estimator, whose aim is to estimate the current noise.

2. The state-to-command feedback of the Control Law, in charge of providing commands one-step ahead.

1.5 Thesis Objective and Organization

The main objective of this thesis consists in exploring the possibility to apply a Nonlinear Model Predictive Control (NMPC) methodology for the NGGM orbit and formation control. The idea comes from the need of developing an optimal control law managing, at the same time, state and input constraints due to the numerous formation scientific requirements and the limited thruster range. Indeed, besides the formation requirements, also the very low thruster authority and the need to cancel the drag-free residual acceleration strongly constraint the problem under study. Being the NMPC an optimal control technique, it could be a suitable method to solve the problem, evaluating the possibility to improve the results obtained with the EMC methodology and proposing a valid alternative strategy. As a matter of fact, the implementation of different techniques is a key point in finding the best and most reliable strategy for the control of a space mission. Indeed, it is worth noticing that the development of a fully autonomous on-board orbit and formation control system is one of the novelties of NGGM since the previous missions, namely GOCE and GRACE, did not require on-board formation control but were managed by on-ground station activity. Thus, like EMC, also the NMPC technique strives to demonstrate the possibility to use an autonomous formation control which real time adapts its control action to the possible variations of the process condition.
Another research question and contribution addressed by this thesis work concerns the development of low-fidelity orbit propagators to cope with the difficulty that exists in the transmission of data between satellites due to the need of using long sampling times of measurements because of the absence of a radio-frequency inter-satellite link. In this regard, the simulator has been made more realistic by means of the implementation of orbit propagators able to compute, on board of each spacecraft, the companion satellite's orbit during the period of time that elapses between the arrival of one measurement data and the next.
The objectives described so far are addressed in six chapters, whose main topics are outlined below in order to provide in the reader a general understanding on how the work has been organized.
Chapter 1 has the intent to introduce the main topics involved in this thesis work, explaining the rationale behind gravimetric missions and then focusing the attention on the main features of the Next Generation Gravity Mission and the technological heritage involved. Beside this, the state of art of the NGGM control unit and the methodology currently adopted for control purposes is provided. Finally, the chapter ends with a brief explanation of the conventional notations adopted for the writing of this thesis.
Chapter 2 presents an overview about the nonlinear model developed in Simulink for the NGGM mission, explaining one by one the blocks which are involved and illustrating how the system components have been modelled to take into account all the atmospheric and gravity disturbances which affect the satellite formation. In addition, after a brief explanation of the different frames of reference involved in this study, a function able to provide the satellites' nominal attitude is introduced in place of the attitude and pointing control system. Finally some simulated results are presented.
Chapter 3 addresses the main aspects of the drag-free, placing the focus on the importance, for gravimetric mission, of having an accurate drag-free controller able to zero all

the disturbance forces and torques affecting the satellites. Further, the control EMC architecture developed for the drag-free control, already exploited for the GOCE space mission is presented and embedded in the nonlinear simulator. This chapter, as the previous one, ends with a section in which the relevant simulated results are summarized.
Chapter 4 is mainly devoted to the orbit and formation control. The main formation requirements are here reported and the development of an NMPC framework for the solution of the problem under study is presented. After a theoretical description of the Model Predictive Control methodology, two different models (HCW vs IFC) are explored as possible candidates for being used as internal prediction model of the control algorithm. After having identified the IFC as the most suitable one, the main concepts about the developed control architecture are outlined and the different NMPC configurations identified during the simulation campaign are presented with their relative results.
Chapter 5 deals with the introduction of low-fidelity orbit propagators to cope with the problem existing in the transmission of data between satellites due to the long sampling times of measurements. Specifically, different versions of orbit propagators are proposed in order to find the model that best computes the satellite's orbit facing the lack of data due to the absence of a radio-frequency inter-satellite link.
Finally, Chapter 6 mainly intends to summarize the achieved results and the still present critical points, concluding by illustrating what could be the possible future developments and research activities in this context.

1.6 Notation Rules

In the following, some notation conventions are specified in order to make the reader aware of the rules adopted to write this thesis and generate a universal language for its understanding.
Free 3D vectors, that are those vectors not defined in a specific frame of reference, are denoted by using an arrow upon their symbol, such as $\vec{v}$; coordinate vectors, instead, that are those vectors existing in a specific frame of reference, are written in bold style as $\boldsymbol{v}$, and finally the symbols referring to coordinate frames of reference are indicated by a subscript. For instance, considering an inertial frame of reference $\mathcal{I} = \{O, \vec{i}_1, \vec{i}_2, \vec{i}_3\}$, the coordinate vector of $\vec{v}$ in the inertial frame will be denoted as $\boldsymbol{v}_i$. The coordinates of a coordinate vector are written unbolded by specifying the components with a numeric subscript, such as v_j, j = 1,2,3, while the magnitude of a vector is specified by its unbolded name, such as v. The coordinate vectors are column vectors but when they are inserted in a text line the inline notation $\boldsymbol{v} = [v_1, v_2, v_3]$ is adopted.
For what concerns the quaternion notation, the italics style q is used. Its coordinates are ordered as per the Hamilton representation, with the real part q_0 that precedes the imaginary one $\boldsymbol{q}$ as in complex numbers. Thus, in vectorial form, a quaternion is represented as

$$q = \begin{bmatrix} q_0 \\ \boldsymbol{q} \end{bmatrix} = \begin{bmatrix} q_0 \\ q_1 \\ q_2 \\ q_3 \end{bmatrix} \tag{1.1}$$

1.7 Abbreviations

The main abbreviations, filed in alphabetical order, are collected in the following Table.

No.	Acronym	Meaning	No.	Acronym	Meaning
1	CoM	Center of Mass	17	INRIM	Italian Metrology Institute
2	CoP	Center of Pressure	18	LAGEOS	Laser Geodynamics Satellite
3	CT	Continuous Time	19	LEO	Low Earth Orbit
4	DT	Discrete Time	20	LISA	Laser interferometer Space Antenna
5	ESA	European Space Agency	21	LTI	Linear Time Invariant
6	EMC	Embedded Model Control	22	MPC	Model Predictive Control
7	EM	Embedded Model	23	NE	Noise Estimator
8	FLOF	Formation Local Orbital Frame	24	NGA NGA	National Geospatial Intelligence Agency
9	GE	Geocentric Equatorial	25 25	NGGM	Next Generation Gravity Mission
10	GOCE	Gravity Field and steady-state Ocean Circulation Explorer	26	NMPC	Nonlinear Model Predictive Control
11	GRACE	Gravity Recovery Climate Ex-periment	27	RAAN	Right Ascension of the Ascending Node
12	GRACE-FO	Grace Follow-On	28	RHC	Receding Horizon Control
13	GNC	Guidance, Navigation and Control	29	SST	Satellite-to-Satellite Tracking
14	GNSS	Global Navigation Satellite System	30	Sat-1	Satellite 1
15	HCW	Hill-Clohessy-Wiltshire	31	Sat-2	Satellite 2
16	IFC	Integrated Formation Control	32	TAS	Thales Alenia Space

Table 1.1: Main Abbreviations

Chapter 2

NGGM Nonlinear Model

The aim of this chapter is to provide an overview about the nonlinear model developed in Simulink for the NGGM mission, explaining one by one the blocks which constitute the plant and the disturbances involved in this study. The part of the simulator presented in this chapter does not consider the control system since the different parts of the control unit will be added one at a time in the following chapters in order to show how the controlled variables, in particular the Satellite-To-Satellite distance, react to the control action.
As shown in figure 2.1, the simulator is composed of three main blocks:

- Satellite 1
- Satellite 2
- Formation Variables

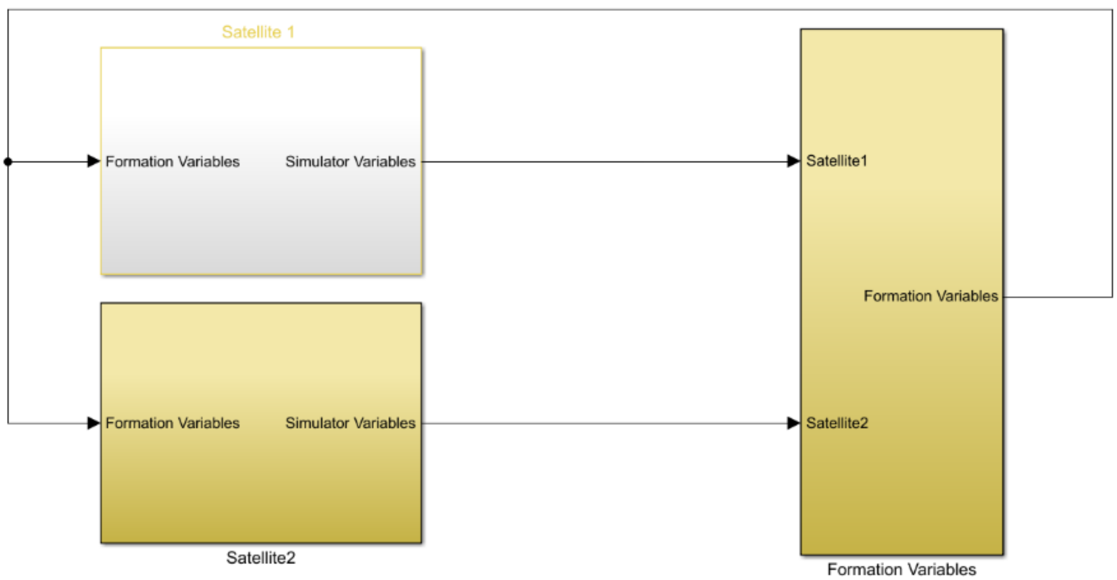

Figure 2.1: NGGM Nonlinear Model

The block "Formation Variables", as shown in Figure 2.2, takes as input the simulated variables of the two satellites and generates the nominal variables of the Formation Local Orbital Frame (FLOF), such as the formation radius, the formation distance, the angular velocity of the FLOF frame, the FLOF quaternion and so on.

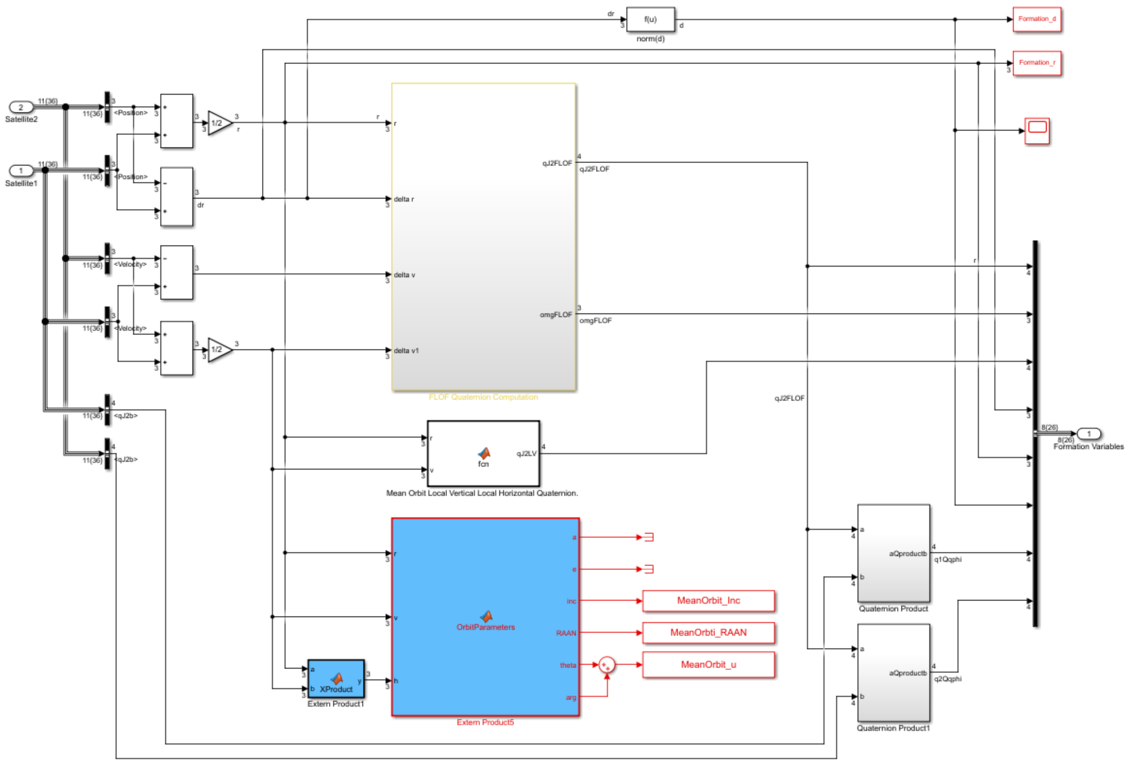

Figure 2.2: NGGM Formation variables

The blocks "Satellite1" and "Satellite2", instead, are identical and each of them includes three parts, as shown in Figure 2.3:

- Satellite
- Atmospheric and Gravity Disturbances
- Sensors

The block "Satellite" contains the satellite kinematics and dynamics and the orbital dynamics block which from the satellite position and velocity vectors derives the orbital elements. The block "Atmospheric and Gravity Disturbances" contains all those models devoted to compute the forces and torques acting on the satellite depending on the environment in which the spacecraft operates. Indeed, the overall forces and torques acting on the spacecraft will be the resultant of the interaction between the satellite and the outside world, and the control actions of the actuators.
The block "Sensors" contains the models of all the measurement instruments and metrology systems adopted by each spacecraft to measure and monitor the variables of interest.

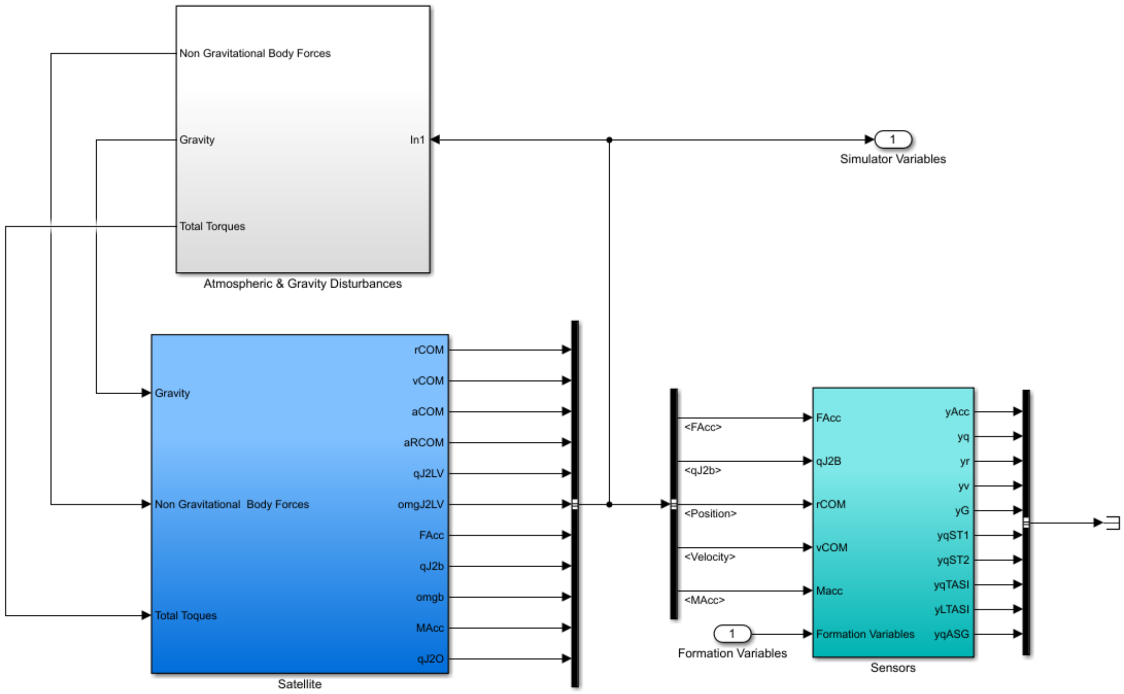

Figure 2.3: Satellite 1 Nonlinear Model

2.1 Satellite Kinematics and Dynamics

A spacecraft can be approximately described as a rigid body which moves with respect to some inertial frame. Its movement is composed by a translation of the body CoM and a rotation of the body about an axis passing through the CoM. The dynamic and kinematic equations are fundamental for spacecraft attitude control and can be seen as a series connection of two nonlinear systems (figure 2.4):

1. The dynamic equations define a system from $\boldsymbol{M}$ (sum of moments or torques) to $\boldsymbol{\omega}$ (angular velocity);
2. The kinematic equations define a system from $\boldsymbol{\omega}$ (angular velocity) to q (body quaternion) which is the output to control.

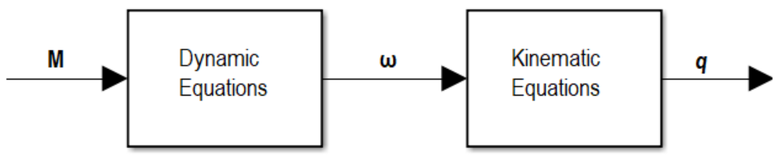

Figure 2.4: Satellite Kinematics and Dynamics

In the simulator, the satellite kinematics and dynamics block receives as input the gravity force, the non-gravitational body forces and the total torques from the atmospheric and gravity disturbance block. The total torques become the input of the attitude dynamics, which contains the dynamic equations, and returns the angular velocity and acceleration of the spacecraft in the body frame. The direction of the vector $\boldsymbol{\omega}$ represents the axis of rotation of the spacecraft and its magnitude is the speed of rotation. Given the inertia matrix J, the dynamic equations of a spacecraft come from the Euler moment equation:

$$J\dot{\boldsymbol{\omega}} = \boldsymbol{M} - \boldsymbol{\omega} \times J\boldsymbol{\omega} \tag{2.1}$$

which can be implemented with the block scheme in figure 2.5.
The angular velocity exiting from the attitude dynamics block is the input of the attitude kinematic equation, whose output is the body quaternion according to the equation

$$\dot{q} = \frac{1}{2} q \otimes \boldsymbol{\omega}^q \tag{2.2}$$

where $\boldsymbol{\omega}^q = (0, \boldsymbol{\omega})$ is the quaternion translation of the angular velocity vector $\boldsymbol{\omega}$.

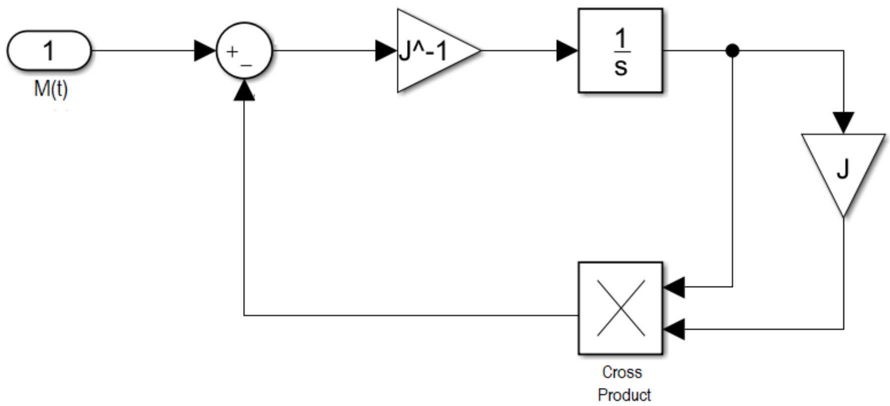

Figure 2.5: Implementation of the Euler Moment Equation

The body quaternion exiting from the attitude kinematic block is then used to perform a frame transformation (from body to inertial) of the non-gravitational body forces which, together with gravity forces, are used in the Orbit Dynamics block to compute the satellite CoM acceleration $\boldsymbol{a_{CoM}}$ and, by integration, the satellite CoM velocity $\boldsymbol{v_{CoM}}$ and position $\boldsymbol{r_{CoM}}$.
The CoM position and velocity, together with the angular momentum $\boldsymbol{h} = \boldsymbol{r_{CoM}} \times \boldsymbol{v_{CoM}}$ are finally used to obtain the six classical orbital elements $(a, e, inc, RAAN, \theta, arg)$, among which we find 5 indipendent quantities used to completely describe the orbit (a,e,ing,RAAN,arg), and one quantity (θ), used to define the spacecraft position on the orbit.

2.2 Orbital Dynamics

The objective of this section is to study the orbital dynamics, that is the translational motion of a mass in a gravitational field. This study is fundamental for spacecraft control and is based on celestial mechanics, in which are involved the following concepts:

- The Kepler's laws, which are empirical laws describing the motion of a body in unperturbed planetary orbits;
- The Newton's laws, which are general physical laws involving the three dynamic principles of motion and the universal gravitational law.

Going more into detail, the Kepler's laws state that:

1. The shape of the orbit of a planet that moves around the Sun is always elliptical;
2. The radius vector between planet and Sun sweeps out equal areas in equal time intervals, that means the areal velocity is constant;
3. The planetary orbital periods are always proportional to $\sqrt{r_m^3}$, where r_m is the mean distance between planet and Sun.

The above-mentioned Kepler's law can be derived from the more general Newton's law reported in the following:

1. First dynamics principle: a particle remains at rest or continues to move at a constant velocity, unless an external force perturbs its motion;
2. Second dynamics principle: the rate of change of momentum of a body over time is directly proportional to the force applied and occurs in the same direction as the applied force:

$$\boldsymbol{F} = m\frac{d\boldsymbol{v}}{dt} = m\boldsymbol{a} \tag{2.3}$$

3. Third dynamics principle: for any force $\boldsymbol{F}_{12}$ exerted by a particle 1 on a particle 2, there exist a force $\boldsymbol{F}_{21} = -\boldsymbol{F}_{12}$ exerted by particle 2 on particle 1.
4. Universal gravitational law: any two particles m_1 and m_2, placed at a certain distance, attract each other with a force

$$\boldsymbol{F} = G\frac{m_1 m_2 \boldsymbol{r}}{r^3} \tag{2.4}$$

   where $\boldsymbol{r}$ is the vector of magnitude $r = |\boldsymbol{r}|$ connecting the two particles and $G = 6.67 \times 10^{-11}\ Nm^2/kg^2$ is the universal constant of gravitation.

Inside the block "Satellite" of the nonlinear model in Figure 2.3 the orbital elements of the satellite motion are derived starting from the values of satellite's velocity and position. In particular, the orbital dynamics block receives as input only the gravity acceleration and the non gravitational body forces that are both involved in the computation of the satellite's acceleration:

$$\boldsymbol{a} = -\boldsymbol{g} + \frac{\boldsymbol{f}_{drag}}{m} + \frac{\boldsymbol{f}_{sun}}{m}. \tag{2.5}$$

The above quantity is then used to obtain the velocity and position vectors, namely $\boldsymbol{r}_{CoM}$ and $\boldsymbol{v}_{CoM}$, by means of two integrators; then, from these two variables the value of the body angular momentum $\boldsymbol{h}$ can be computed instant by instant as

$$\boldsymbol{h} = \boldsymbol{r}_{CoM} \times \boldsymbol{v}_{CoM}. \tag{2.6}$$

As a matter of fact, $\boldsymbol{r}_{CoM}$, $\boldsymbol{v}_{CoM}$ and $\boldsymbol{h}$ are all necessary for the derivation of the 6 orbital elements used to completely describe the orbit of the spacecraft and its position. Let's recall that knowing the 6 orbital elements is equivalent to know the velocity and position vectors of a spacecraft since they fully describe the body motion. In particular, these elements, collected in Table 2.1, are composed by 5 independent quantities (a,e,Ω,i,ω) which define the orbit of a body and 1 quantity (ν) which gives the body position on the orbit.

Element	Description	Range	Undefined
a: semimajor axis	Size	Depends on the conic section	never
e: eccentricity	Shape	$e = 0$: circle $0 < e < 1$: ellipse	never
i: inclination	Tilt angle between equatorial and orbital planes	$0 \leq i \leq 180°$	never
Ω: RAAN	Angle from vernal equinox to ascending node	$0 \leq \Omega \leq 360°$	when $i = 0°$ or $i = 180°$
ω: argument of perigee	Angle from ascending node to perigee	$0 \leq \omega \leq 360°$	when $i = 0°$, $i = 180°$ or $e = 0$
ν: true anomaly	Angle from perigee to the spacecraft position	$0 \leq \nu \leq 360°$	when $e = 0$

Table 2.1: Classical Orbital Elements

The elements mentioned above can be obtained from the known quantities as follows:

$$\boldsymbol{e} = \frac{1}{\mu}\boldsymbol{v}_{CoM} \times \boldsymbol{h} - \frac{\boldsymbol{r}_{CoM}}{r_{CoM}}, \qquad a = \frac{h^2}{(\mu(1-e^2))}, \qquad \cos i = \boldsymbol{K} \cdot \frac{\boldsymbol{h}}{h}$$
$$\cos\omega = \boldsymbol{I'} \cdot \frac{\boldsymbol{e}}{e}, \qquad \cos\Omega = \boldsymbol{I} \cdot \boldsymbol{I'}, \qquad \cos\nu = \boldsymbol{r}_{CoM} \cdot \frac{\boldsymbol{e}}{re} \tag{2.7}$$

where μ is the gravitational parameter and $\boldsymbol{I}$ and $\boldsymbol{K}$ define the coordinate vectors of the first and the third axis of the inertial geocentric equatorial frame which will be later described in detail in Section 2.5.

2.3 Atmospheric and Gravity disturbances

The block used to model the disturbances involved in this study is composed by two main contributions: one to derive the gravity force and torque and the other one to obtain the environmental forces and torques acting on the satellite.
Firstly, let's analyse the Atmospheric Disturbance block. This block takes as input the data coming from the Satellite Dynamics and Kinematics, and in particular the needed variables are the satellite position $\boldsymbol{r_{CoM}}$ and velocity $\boldsymbol{v_{CoM}}$.

2.3.1 Aerodynamic Drag

The Drag Model is used to derive the Aerodynamic Drag, that is the atmospheric friction opposing the spacecraft velocity vector [7]. Since it is proportional to the density, drag represents a significant disturbance force, especially in Low Earth Orbits as density decreases exponentially with the altitude. The atmospheric drag reduces the energy of the orbit and produces the decrease of the apogee height, reducing the eccentricity and therefore causing orbital decay.
The NGGM spacecraft can be considered made by several flat surfaces, each one identified by its normal unit vector and its centre. The actual model of the spacecraft is composed by 18 surfaces, which is a good trade-off considering that increasing the number of flat surfaces the computational load grows but forces and torque profiles, which show some discontinuities due to the finite dimension of each tile, can be smoothed by reducing the surfaces dimension.
Given the direction of the air flow, a tile is considered shadowed if its centre is not directly exposed to the current and, generally, its contribution in the resultant aerodynamic force and torque can be neglected. Only in the case of thermal effects, even the shadowed elements must be considered since they can give a not null contribution.
The contribution given by each tile depends on the element surface, the relative wind velocity and the air density. Indeed, the Drag Model block takes as input the body wind velocity and the body angular rate and computes the relative velocity of each flat surface; then, the contributions of all the surfaces are combined to obtain the overall drag forces and torques.
For each flat surface element, given the relative direction of the air flow, drag and lift forces, or alternatively normal and tangential forces, are computed as follows [7]:

$$\begin{aligned} \vec{D}_A &= -\frac{1}{2}\rho V^2 A C_D \vec{u}_V, \qquad & \vec{L}_A &= -\frac{1}{2}\rho V^2 A C_L \vec{u}_Z; \\ \vec{N}_A &= -\frac{1}{2}\rho V^2 A C_N \vec{n}_A, \qquad & \vec{T}_A &= -\frac{1}{2}\rho V^2 A C_T \vec{t}_A; \end{aligned} \tag{2.8}$$

where C_D, C_L, C_N, C_T are respectively the drag, lift, normal and tangential coefficients, A $[m^2]$ is the surface area, ρ $[kg/m^3]$ is the air density, V $[m/s]$ is the airflow velocity and $\vec{u}_V, \vec{u}_Z, \vec{n}_A, \vec{t}_A$ are respectively the drag, lift, normal and tangent unit vectors.
The Drag Model needs as input the atmospheric density which is obtained by the Density Model. Since air density is not constant and it is complex to write it with an equation, we make use of a sort of look up table (the density NASA model) that gives as output the value of the air density for each position $\boldsymbol{r_{CoM}}$. In order to indicate exactly the position of the

satellite CoM, we need to use a clear and universal reference system. Thus, the Geodetic function is used to transform $\boldsymbol{r_{CoM}}$ into geodetic coordinates i.e. longitude, latitude and height. In addition, even if the position is exactly known, being the models always affected by uncertainty, we need also to consider such uncertainty by adding a filtered noise to the output of the look up table.
To compute the aerodynamic coefficients, the kind of interaction between the body and the air flow must be considered, eventually taking into account the momentum transfer between the gas particle and the surface element. This interaction is described by the collision of the air molecules with the surface. The velocity $\vec{V}$ of such molecules is given by two contributions: the avarage relative velocity $\vec{V_R}$ of the air with respect to the spacecraft and the thermal velocity $\vec{V_a}$ of the particle: $\vec{V} = \vec{V_R} + \vec{V_a}$.
Therefore, we can distinguish two models [7]:

1. Hyper-thermal model: $\vec{V_a}$ is assumed negligible with respect to $\vec{V_R}$, the particles move in straight lines parallel to the airflow and only those surfaces directly invested by the airflow contribute to the definition of the aerodynamic coefficients. The hyper-thermal flow occurs when $V_R/V_a \geq 10$;

2. Thermal model: $\vec{V_a}$ is assumed comparable with respect to $\vec{V_R}$, the particles motion is not parallel to the airflow direction and also the shadowed surfaces contribute to the definition of the aerodynamic coefficients. The thermal flow occurs when $V_R/V_a < 10$.

The ratio $S = V_R/V_a$ is called molecular speed ratio and is the ratio of the spacecraft relative velocity modulus to the speed of air V_a at temperature T_a. Further, the kind of interaction influences also the momentum exchange. A particle hitting a surface gets trapped by the surface itself transferring its momentum, but it can be eventually re-emitted by the surface along a direction and with a velocity which depends on the type of collision [7]. Two limit cases can be distinguished:

1. Specular reflection: the particles are re-emitted along a specular direction without momentum variation (perfect elastic collision).

2. Diffused reflection: the particles are scattered in all the directions, according to the cosine law, with a velocity depending on a probabilistic law.

The coefficients σ_n and σ_t are introduced to take into account the relative importance of diffused reflection with respect to specular reflection [7].
The aerodynamic coefficients are obtained in the following way:

Hyper-Thermal Model

$$
\begin{aligned}
C_L &= 2\Big[(2-\sigma_n-\sigma_t)\cos\theta + \sigma_n \frac{V_b}{V_R}\Big]\sin\theta\cos\theta \\
C_D &= 2\Big[(2-\sigma_n-\sigma_t)\cos^2\theta + \sigma_n \frac{V_b}{V_R}\cos\theta + \sigma_t\Big]\cos\theta
\end{aligned}
\tag{2.9}
$$

Thermal Model

$$C_L = 2\Big[\frac{2-\sigma_n}{S\sqrt{\pi}}\cos\theta - \frac{\sigma_t}{S\sqrt{\pi}}\cos\theta + \frac{\sigma_n}{2S^2}\sqrt{\frac{T_b}{T_a}}\Big]\sin\theta exp(-S^2\cos^2\theta)+$$
$$+\Big[(2-\sigma_n)(\frac{1}{2S^2}+\cos^2\theta) - \sigma_t\cos^2\theta + \frac{\sigma_n}{S}\frac{\sqrt{\pi}}{2}\cos\theta\sqrt{\frac{T_b}{T_a}}\Big]\sin\theta(1+erf(S\cos\theta))$$
$$C_D = 2\Big[\frac{2-\sigma_n}{S\sqrt{\pi}}\cos^2\theta + \frac{\sigma_t}{S\sqrt{\pi}}\sin^2\theta + \frac{\sigma_n}{2S^2}\cos\theta\sqrt{\frac{T_b}{T_a}}\Big]exp(-S^2\cos^2\theta)+$$
$$+\Big[(2-\sigma_n)(\frac{1}{2S^2}+\cos^2\theta) + \sigma_t\sin^2\theta + \frac{\sigma_n}{S}\frac{\sqrt{\pi}}{2}\cos\theta\sqrt{\frac{T_b}{T_a}}\Big]\cos\theta(1+erf(S\cos\theta)) \tag{2.10}$$

where V_b and T_b are respectively the body velocity and temperature and $erf(x)$ is the error function:

$$erf(x) = \frac{2}{\sqrt{\pi}}\int_0^x e^{-t^2}\,dt \tag{2.11}$$

In the non-linear simulator presented here, the thermal model has been adopted as it is conservative with respect to the hyper-thermal and allows to consider the worst case.
The point in which the drag force is applied is called Centre of Pressure (CoP). Therefore, the drag force produces also a torque having magnitude proportional to the lever arm, that is the distance between CoM and CoP. Nevertheless, the CoP is not a fixed point and its position is determined a posteriori. Thus, the CoP can be approximated by the CoA; this approximation is conservative in the sense of aerodynamic stability.
In the simulator the drag forces and torques are multiplied by a respective flag. In our study we set to zero the flag which multiplies the drag torque in order to consider for simplicity only the drag force.

2.3.2 Solar Pressure

The second important atmospheric disturbance to be considered in this study is the solar radiation pressure, that is the mechanical pressure exerted upon the spacecraft surfaces due to the exchange of momentum between the spacecraft and the electromagnetic field [7]. The effects of this disturbance are modelled in the simulator by means of the Sun Model. The concept of solar radiation pressure revolves around the idea that electromagnetic waves are massless, but exhibit mass-like properties [7]. The photons in the light emitted from the sun move at light velocity and have momentum. Since they have momentum, when they hit an other object, such as a spacecraft, they transfer momentum to it, causing a boost in its velocity. However, the momentum carried by these photons is extremely small. Thus, the perturbing force isn't really observed in low earth orbit (LEO) spacecrafts but becomes more significant for higher orbits.
The input of the Sun Model is the spacecraft position $\boldsymbol{r_{CoM}}$ because in order to compute the sun forces and torques, the spacecraft and sun positions in both inertial and body frame are needed; the last one is obtained with a reference frame transformation from Inertial to Body using the disturbance attitude quaternion, given by a quaternion product between

the LORF quaternion and the quaternion error. The sun position is needed because only the surfaces that are directly exposed to the sun must be taken in consideration.
The effect of solar pressure is computed considering the solar flux hitting each surface of the spacecraft. Thus, for each surface is defined the solar pressure force $\vec{F}_{rk}$, which is applied in the surface CoP, and is computed considering the contribution of specular reflections, diffuse reflections and total absorption [7]. Indeed, an incident electromagnetic wave can interact with a surface in four different modes:

1. pure absorption: radiation is completely absorbed by the surface;
2. specular reflection: radiation is specularly reflected;
3. diffuse reflection: radiation is diffusely reflected in any direction;
4. transmission: radiation is transmitted through the surface.

The sum of the fractions of the different modes (represented respectively by suitable coefficients C_a, C_s, C_d, and C_t) must be equal to 1 [7]:

$$C_a + C_s + C_d + C_t = 1 \tag{2.12}$$

However, since most of the spacecraft surfaces are optically opaque, it is possible to assume $C_t \cong 0$.
The electromagnetic radiation pressure can be computed in magnitude as the ratio of the source irradiance Φ $[W/m^2]$ to the speed of light in vacuum c $[m/s]$:

$$p = \frac{\Phi}{c} \tag{2.13}$$

At the Sun-Earth distance the magnitude of the solar radiation is $\Phi_{sun} = 1371 \pm 10\ W/m^2$ and the corresponding solar radiation pressure is $p = 4.6 \times 10^6\ Pa$.
By denoting with $\vec{n}$ the outward normal of an infinitesimal area dA, $\vec{s}$ the opposite direction of the incoming wave and α the incidence angle, the elementary radiation force $d\vec{F}_r$ relative to the elementary area dA is:

$$\begin{aligned} d\vec{F}_r &= -p\cos\alpha dA(C_d(\vec{s} + 2\vec{n}/3) + C_a\vec{s} + 2C_s\cos\alpha\vec{n}) \\ &= -p\cos\alpha dA((1 - C_s)\vec{s} + 2(C_s\cos\alpha + C_d/3)\vec{n}) \end{aligned} \tag{2.14}$$

It is worth to notice that the formula written above is valid only for the surfaces exposed to the solar irradiation, i.e. only when $\cos\alpha = \vec{n} \cdot \vec{s} \geq 0$ [7]. In the other case, that is when $\cos\alpha < 0$, the elementary radiation force $d\vec{F}_r$ is null [7]. Consequently, we can introduce a coefficient called *illumination* that varies between 0 and 1 depending on how the surface is exposed to the solar radiations.
The spacecraft surface is subdivided into $n = 18$ planar surfaces of area A_k, with $k = 1, \ldots, n$. Therefore, the overall sun force and torque are computed by summing the contributions of all the 18 surfaces as follows:

$$\begin{aligned} \vec{F}_r &= \sum_{k=1}^{n} illumination_k * \vec{F}_{rk} \\ \vec{M}_r &= \sum_{k=1}^{n} \vec{r}_{cp_k} \times (illumination_k * \vec{F}_{rk}) \end{aligned} \tag{2.15}$$

where the CoP of the k-th surface is denoted with $\vec{r}_{cp_k}$ and the k-th surface force is obtained in the following way, upon denoting the surface normal with $\vec{n}_k$, the incidence angle with α_k and the diffusion and specular coefficients with C_{dk} and C_{sk} [7]:

$$\vec{F}_{rk} = \iint_{A_k} d\vec{F}_{rk} = -p((1 - C_{sk})\vec{s}_k + 2(C_{sk}max(\cos\alpha_k,0) + C_{dk}/3)\vec{n}_k)max(\cos\alpha_k,0)A_k \tag{2.16}$$

In our simulator, the reflection model adopted is totally reflective and poor reflectivity is attributed to the solar arrays.

2.3.3 Gravity Disturbance

The Earth gravity field interacts with the satellite generating a force that applied in the CoM determines the body orbit, and a torque that acts as an attitude perturbation. This disturbance is modelled in the simulator by means of the Gravity Model which takes as input the spacecraft position $\boldsymbol{r_{CoM}}$ and gives as output the gravity force and torque.

Gravity Force

The gravity force is obtained by means of a Simulink block called "Spherical Harmonics", which is part of the Aerospace Blockset library. This block implements a spherical harmonic representation of planetary gravity at a specific location based on planetary gravitational potential and provides a good way to represent the spherical harmonic expansion of the Earth gravitational field outside of its surface [7]. The planetary model used in our specific case is EGM2008, that is the latest Earth spherical harmonic gravitational model from National Geospatial-Intelligence Agency (NGA). This block is needed to consider more accurate gravity values than those obtained by the spherical gravity model, which ideally assumes the Earth mass concentrated in its centre as in a central force field.
In this case, the gravity acceleration $\vec{g}(\vec{r})$ at a point P located at a distance $\vec{r}$ from the Earth CoM is given by the formula

$$\vec{g}(\vec{r}) = -Gm_0\frac{\vec{r}}{r^3} \tag{2.17}$$

where $m_0 = 5.972 \times 10^{24}$ $[kg]$ is the Earth mass and $G = 0.3986 \times 10^{15}$ $[m^3/s^2]$ is the Earth universal gravitational constant.
Nevertheless, it is worth considering that the Earth is not a perfect sphere and its mass is not uniformly distributed. Indeed, in the realistic situation, the Earth mass is spatially distributed within a radius r_0, with $r_0 < r$, and the Earth is an oblate spheroid, flattened at the poles, with a difference between the two semi-axes of 21 km; thus, the mass distribution must be accounted for by decomposing m_0 into infinitesimal masses in position $\vec{s}$ from the Earth CoM and then summing all the contributions given by these elementary masses [7].
Since the gravity force is conservative, that is a function of the distance $|\vec{r} - \vec{s}|$, it is convenient to obtain the gravity acceleration in P as the negative gradient of the gravitational potential [7], defined as:

$$U(\vec{r}) = G\iiint_V \frac{dm}{|\vec{r} - \vec{s}|} \tag{2.18}$$

where $dm = \rho(\vec{s})d^3\vec{s}$ is an infinitesimal mass element of density $\rho(\vec{s})$, $|\vec{r} - \vec{s}|$ is the relative position of P, and V is the volume of the Earth [7]. Thus, the gravity acceleration can be obtained by

$$\vec{g}(\vec{r}) = -\nabla U(\vec{r}) = \Big(\frac{\partial U}{\partial x}, \frac{\partial U}{\partial y}, \frac{\partial U}{\partial z}\Big) \tag{2.19}$$

The vectors $\vec{r}$ and $\vec{s}$ can be expressed in spherical coordinates, respectively as $[r, \lambda, \theta]$ and $[s, \lambda_s, \theta_s]$, where the first component is the vector module, the second component is the polar (or zenith) angle and the third component is the azimuthal angle [7]. The Cartesian coordinates in the Earth-Centered-Earth-Fixed frame (ECEF) of the two vectors are:

$$\boldsymbol{r} = \begin{bmatrix} r_1 \\ r_2 \\ r_3 \end{bmatrix} = r \begin{bmatrix} \sin\theta\cos\lambda \\ \sin\theta\sin\lambda \\ \cos\theta \end{bmatrix}, \qquad \boldsymbol{s} = s \begin{bmatrix} \sin\theta_s\cos\lambda_s \\ \sin\theta_s\sin\lambda_s \\ \cos\theta_s \end{bmatrix} \tag{2.20}$$

With this notation it is possible to rewrite the mass element dm in Eq. 2.18 as

$$dm = \rho(\vec{s})d^3\vec{s} = \rho(s, \lambda_s, \theta_s)s^2 \sin\theta_s ds d\lambda_s d\theta_s. \tag{2.21}$$

Now, lets consider the case $r > s = |\vec{s}|$, that is when the point P, for instance the spacecraft CoM, is outside the Earth surface [7]. In this case, Eq. 2.18 may be expanded into the following series of spherical harmonics, also called Legendre polynomials:

$$\frac{1}{|\vec{r} - \vec{s}|} = \frac{1}{r\sqrt{1 + \frac{s^2}{r^2} - 2\frac{s}{r}\cos\alpha}} = \frac{1}{r}\sum_{k=0}^{\infty}\Big(\frac{s}{r}\Big)^k P_k(\cos\alpha) \tag{2.22}$$

where $\cos\alpha = \frac{\vec{r}\cdot\vec{s}}{rs} = \cos\theta\cos\theta_s + \sin\theta\sin\theta_s\cos(\lambda - \lambda_s)$, and the function $P_k(x)$ comes from the Rodrigues formula:

$$P_k(x) = \frac{1}{2^k k!}\frac{d^k(x^2-1)^k}{dx^k} \tag{2.23}$$

which can be used to obtain the following low-degree Legendre polynomials:

$$\begin{aligned} P_0(\cos\alpha) &= 1 \\ P_1(\cos\alpha) &= \cos\alpha \\ P_2(\cos\alpha) &= \frac{1}{2}(3\cos^2\alpha - 1) \\ P_3(\cos\alpha) &= \frac{1}{2}(5\cos^3\alpha - 3\cos\alpha) \\ P_4(\cos\alpha) &= \frac{1}{8}(35\cos^4\alpha - 30\cos^2\alpha + 3). \end{aligned} \tag{2.24}$$

From the Legendre polynomials addition theorem, it is allowed to rewrite $P_k(\cos\alpha)$ as:

$$P_k(\cos\alpha) = P_k(\cos\theta)P_k(\cos\theta_s) + Q_k(\theta, \theta_s, \lambda - \lambda_s) \tag{2.25}$$

where $Q_k(\theta, \theta_s, \lambda - \lambda_s)$ is a sequence of other Legendre functions:

$$Q_k(\theta, \theta_s, \lambda - \lambda_s) = 2\sum_{j=1}^{k} \frac{(k-j)!}{(k+j)!} \times \cos\left(j(\lambda - \lambda_s)\right) P_j^k \cos\theta P_j^k(\cos\theta_s) \tag{2.26}$$

and $P_k^j(x)$ is given by:

$$P_k^j(x) = (1-x^2)^{j/2} \frac{d^j}{dx^j} P_k(x) = \frac{(1-x^2)^{j/2}}{2^k k!} \frac{d^{k+j}}{dx^{k+j}} (x^2-1)^k \tag{2.27}$$

where k is the degree, j is the order and $P_k^0(x) = P_k(x)$.
We can now insert these formulas inside the Eq. 2.18 obtaining a new expression for the gravitational potential:

$$\begin{aligned} U(\vec{r}) &= \frac{\mu}{r}\Big[1 + \sum_{k=2}^{\infty}\sum_{j=0}^{k}\Big(\frac{R_e}{r}\Big)^k P_k^j \cos\theta (C_k^j \cos j\lambda + S_k^j \sin j\lambda)\Big] \\ &= \frac{\mu}{r}\Big[1 - \sum_{k=2}^{\infty}\Big(\frac{R_e}{r}\Big)^k J_k P_k \cos\theta + \sum_{k=2}^{\infty}\sum_{j=1}^{k}\Big(\frac{R_e}{r}\Big)^k P_k^j \cos\theta (C_k^j \cos j\lambda + S_k^j \sin j\lambda)\Big] \end{aligned} \tag{2.28}$$

where $\mu = Gm_0$ is the Earth gravitational parameter, R_e is the Earth equatorial radius and C_k^j, S_k^j and $J_k = -C_k^0$ are coefficients obtained from satellite observations.
The functions

$$\begin{aligned} &\frac{1}{r^{k+1}} P_k^j \cos\theta \cos j\lambda \\ &\frac{1}{r^{k+1}} P_k^j \cos\theta \sin j\lambda \end{aligned} \tag{2.29}$$

are called Spherical Harmonics.
On the basis of the values of k and j we can distinguish three types of harmonics, as shown in Figure 2.6:

1. The ***zonal*** harmonics are those with $j = 0$. The superposition of these harmonics is useful to describe variations in latitude, not depending on longitude. Indeed, zonal harmonics divide the sphere into k latitudinal zones.

2. The ***sectorial*** harmonics are those with $k = |j|$. They divide the globe into $2j$ vertical sectors by means of $2j$ meridians.

3. The ***tesseral*** harmonics are those with $k \neq j$ and $j \neq 0$. Tesseral harmonics vanishes at $2j$ meridians of longitude and $k - j$ parallels of latitude.

Summing up, the degree k gives the total number of nodal lines and the order j decides how this number is distributed over nodal meridians and parallels. The higher the degree and the order, the finer the details that can be represented.
Coming back to the ideal case, in which we have considered the Earth as a perfect sphere with density $\rho(\vec{s})$ constant in space, it is possible to obtain the formula written in Eq. 2.17,

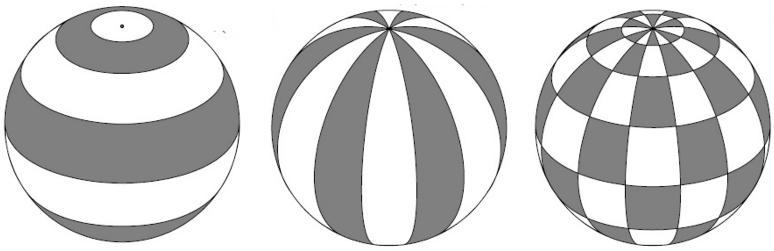

Figure 2.6: Types of Spherical Harmonics: (a) Zonal, (b) Sectorial, (c) Tesseral

by means of the spherical harmonic expansion noting that, under these ideal assumptions, $J_k = C_k^j = S_k^j = 0$, that implies:

$$U(\vec{r}) = \frac{\mu}{r}, \qquad \vec{g}(\vec{r}) = -\mu\frac{\vec{r}}{r^3} \tag{2.30}$$

In a more realistic situation, being $\rho(\vec{s})$ not constant but symmetric about the z axis, $C_k^j = S_k^j = 0$, implying

$$U(\vec{r}) = \frac{\mu}{r}\Big[1 - \sum_{k=2}^{\infty}\Big(\frac{R_e}{r}\Big)^k J_k P_k \cos\theta\Big] \tag{2.31}$$

where J_k are the zonal harmonic coefficients.
In our Gravity Model we have considered a degree $k = 30$ in order to have an efficient and accurate high-degree spherical harmonic representation of the gravity field.

Gravity Gradient Torque

As previously said, a second contribution given by the Earth gravity field is the gravity gradient torque. This torque is due to the nonuniform gravity forces acting on extended bodies [7]. Let's denote the position of an elementary body mass with respect to the body CoM with $\vec{s} = \vec{r} - \vec{r}_c$ where $\vec{r}$ is the mass position and $\vec{r}_c$ is the spacecraft CoM position [7].The moment about the spacecraft CoM is given by

$$\vec{M}_g = \int_B \vec{s} \times \vec{g}(\vec{r})\, dm \tag{2.32}$$

where B is the body volume [7].
By defining the gravity tensor $U_b(\boldsymbol{r}_c) = \nabla \boldsymbol{g}(\boldsymbol{r}_c)$, we can expand the gravity acceleration around the spacecraft CoM in the following way [7]:

$$\vec{g}(\vec{r}) = \vec{g}(\vec{r}_c) + \nabla\vec{g}(\vec{r}_c)\vec{s} + \dots \tag{2.33}$$

Now, using the previous equations and recalling that by definition of CoM $\int_B \vec{s}\, dm = 0$, we can express the coordinate vector $\boldsymbol{M}_g$ as

$$\boldsymbol{M}_g = \Big(\int_B \boldsymbol{s}\, dm\Big) \times \boldsymbol{g}(\boldsymbol{r}_c) + \int_B \boldsymbol{s} \times U_b(\boldsymbol{r}_c)\boldsymbol{s}\, dm = \int_B \boldsymbol{s} \times U_b(\boldsymbol{r}_c)\boldsymbol{s}\, dm \tag{2.34}$$

that in matrix form becomes

$$\boldsymbol{M}_g = \int_B \begin{bmatrix} 0 & -s_3 & s_2 \\ s_3 & 0 & -s_1 \\ -s_2 & s_1 & 0 \end{bmatrix} \begin{bmatrix} U_{11}s_1 & U_{12}s_2 & U_{13}s_3 \\ U_{21}s_1 & U_{22}s_2 & U_{23}s_3 \\ U_{31}s_1 & U_{32}s_2 & U_{33}s_3 \end{bmatrix} dm. \tag{2.35}$$

The integral in Eq. 2.35 can be substituted considering the inertia matrix J of the mass distribution with respect to the body axes [7]. To this purpose, let's recall the expression of J as function of the mass element position with respect to the body CoM:

$$J = \int_B (\boldsymbol{s}^T \boldsymbol{s} I_3 - \boldsymbol{s}\boldsymbol{s}^T)\, dm. \tag{2.36}$$

Replacing the inertia matrix J inside Eq. 2.35 it is possible to obtain a more general expression of the gravity gradient torque as a function of the matrix J and the gravity tensor $U_b(\boldsymbol{r}_c)$ as follows [7]:

$$\boldsymbol{M}_g = \begin{bmatrix} (J_{33} - J_{22})U_{23} + (U_{22} - U_{33})J_{23} + U_{12}J_{13} - U_{13}J_{12} \\ (J_{11} - J_{33})U_{13} + (U_{33} - U_{11})J_{13} + U_{23}J_{12} - U_{12}J_{23} \\ (J_{22} - J_{11})U_{12} + (U_{11} - U_{22})J_{12} + U_{13}J_{23} - U_{23}J_{13} \end{bmatrix}. \tag{2.37}$$

This time, in order to simplify the formula in Eq. 2.37, we assume to consider only the spherical gravity term. From Eq. 2.30, we recall that, with this assumption, the gravity acceleration is $\boldsymbol{g}(\boldsymbol{r}_c) = -(\mu/r_c^3)\boldsymbol{r}_c$, where $r_c = |\vec{r}_c|$.
Since the Jacobian matrix of $\boldsymbol{r}_c$ is the identity matrix and the gradient of $r_c^3 = (\boldsymbol{r}_c^T\boldsymbol{r}_c)^{3/2}$ is $3\boldsymbol{r}_c^T(\boldsymbol{r}_c^T\boldsymbol{r}_c)^{1/2} = 3\boldsymbol{r}_c^T\boldsymbol{r}_c$, the following expression for the gravity tensor holds:

$$U_b(\boldsymbol{r}_c) = -\mu\left(\frac{I_3}{r_c^3} - \frac{3}{r_c^5}\begin{bmatrix} r_{1c}^2 & r_{1c}r_{2c} & r_{1c}r_{3c} \\ r_{1c}r_{2c} & r_{2c}^2 & r_{2c}r_{3c} \\ r_{1c}r_{3c} & r_{2c}r_{3c} & r_{3c}^2 \end{bmatrix}\right) = \frac{3\mu}{r_c^5}\left(\boldsymbol{r}_c\boldsymbol{r}_c^T - \frac{\boldsymbol{r}_c^T\boldsymbol{r}_c}{3} I_3\right). \tag{2.38}$$

With the gravity tensor expression written above, the Eq. 2.37 becomes:

$$\boldsymbol{M}_g = \frac{3\mu}{r_c^5}\begin{bmatrix} (J_{33} - J_{22})r_{2c}r_{3c} + (r_{2c}^2 - r_{3c}^2)J_{23} + r_{1c}(r_{2c}J_{13} - r_{3c}J_{12}) \\ (J_{11} - J_{33})r_{3c}r_{1c} + (r_{3c}^2 - r_{1c}^2)J_{13} + r_{2c}(r_{3c}J_{12} - r_{1c}J_{23}) \\ (J_{22} - J_{11})r_{1c}r_{2c} + (r_{1c}^2 - r_{2c}^2)J_{12} + r_{3c}(r_{1c}J_{23} - r_{2c}J_{13}) \end{bmatrix} \tag{2.39}$$

where r_{1c}, r_{2c} and r_{3c} are the coordinates of the vector $\boldsymbol{r}_c$ expressed in the body frame [7]. Finally, to rewrite the Eq. 2.39 in a more compact way, it can be proven that in case of spherical gravity and for an arbitrary inertia matrix J, the gravity gradient torque can be computed as [7]:

$$\boldsymbol{M}_g = \frac{3\mu}{r_c^3}\frac{\boldsymbol{r}_c}{r_c} \times J\frac{\boldsymbol{r_c}}{r_c} = \frac{3\mu}{r_c^5}\boldsymbol{r}_c \times J\boldsymbol{r}_c. \tag{2.40}$$

2.4 Sensors

This paragraph briefly illustrates the operating principles and models of the most common orbit and attitude sensors. The term sensor is here used to represent an instrument mounted on the satellite whose aim is to measure a certain quantity. Starting from physical principles, the aim is to derive a measurement model that consists of the error model plus the sensor dynamics.
Spacecraft sensors may roughly be subdivided into three main categories:

1. Inertial navigation sensors, such as accelerometers and gyroscopes. These sensors are able to detect acceleration and angular rate variations, without any field-of-view for observing external electromagnetic sources and any link with ground stations and other satellites. In particular, accelerometers are compulsory for drag-free control purposes because they measure the non-gravitational forces acting on a spacecraft that must be counteracted by propulsion actuators.

2. Position and navigation sensors, such as the Global Navigation Satellite System [GNSS]. These sensors observe the motion of the spacecraft CoM with respect to the GNSS constellation and measures the spacecraft position and velocity. In our nonlinear model the only navigation sensor that has been considered is the GPS since it represent a standard model for all the other GNSS constellations.

3. Attitude sensors, such as Sun and Earth sensors, star trackers and magnetometers. These last, together with position sensors, are complementary to the inertial ones since they are used to correct trajectories affected by drift and reset the inertial sensor drift to zero. Attitude sensors observe the spacecraft orientation with respect to a reference frame given by visible objects, such as stars or planets, and so they need a field-of-view for receiving the light emitted by such objects.

The sensors modelled in our nonlinear simulator are:

- Accelerometers to measure the non-gravitational body accelerations
- GPS to measure the spacecraft position and velocity
- Star trackers to measure the satellite attitude quaternion
- Acquisition and pointing metrology system developed by TAS

All sensors are modelled by summing a noise to the clean signal. For instance, in the accelerometer model, there is a filtered high frequency noise to which are added bias and drift. This noise is given by a random number processed by a second order low-pass-filter in order to represent the low frequency variations which implies a non-constant bias. Moreover, in the model we can notice also the presence of some integrators with feedback used as filters in order to consider the sensor finite bandwidth.
Star trackers, instead, are the most accurate attitude sensors and directly provide a measure of the spacecraft attitude quaternion. Since they measure attitude errors, the noise to be added to the clean signal in this case is given by an additional rotation. The sensor is modelled by a quaternion product between the clean attitude quaternion and a filtered noise which is expressed in quaternion form. Sometimes two quaternion products must be considered, the first one to take into account the star tracker assembly errors and the second one to account for the error given by additional rotations.

2.5 Frames of Reference

After having described the main parts composing the NGGM nonlinear model, it is worth to mention which are the main reference frames exploited in this model in order to represent variables. In particular, two of them are observational frames, used to describe the motion of the system, while the last one is referred to as "body frame", and it is defined for each satellite in order to describe its attitude.

Inertial Frame of Reference

The first relevant reference frame is the observer's inertial frame. We recall that an Inertial frame of reference is a reference frame in which the Newton's first law of motion holds. This means that, in an inertial frame, a physical object, with zero net force acting on it, will persist in its state of rest or uniform rectilinear motion until it is perturbed. In a purely kinematic definition, a frame $R = \{O, \vec{i}, \vec{j}, \vec{k}\}$ is *inertial* when the origin O is not accelerating and its axes are not rotating. Several reference frames may be associated to elliptic orbits in order to specify the positions of celestial objects. In this thesis, the observer's inertial frame that has been considered is the Geocentric Equatorial (GE) frame $R_{ge} = \{C_E, \vec{I}, \vec{J}, \vec{K}\}$ frozen at some date. This frame is centred in the Earth CoM C_E, not rotating with the Earth and independent of the spacecraft orbit. To define it, the undisturbed orbital plane described by the Earth revolution about the Sun must be considered. This inertial plane is called "ecliptic", and is the plane where the unitary vectors $\vec{I}$ and $\vec{J}$ lies. The normal

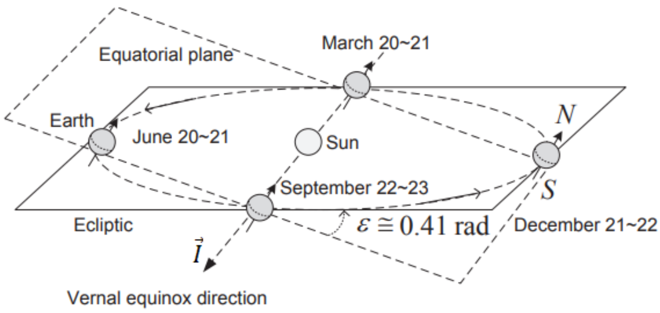

Figure 2.7: Ecliptic Plane, Earth-Sun Orbit and Equatorial Plane [7]

to the ecliptic plane points in the same direction of the Earth's North Pole and defines the direction of the unitary vector $\vec{K}$. Then, $\vec{I}$ is selected to be aligned with the ecliptic and equatorial plane intersection and is defined as the Earth-Sun direction at the vernal equinox, as shown in the Figure 2.7. Finally, $\vec{J}$ is selected as $\vec{J} = \vec{K} \times \vec{I}$ and lies on the equatorial plane. Figure 2.8 represents the Geocentric Equatorial frame.

Formation Local Orbital Frame

The NGGM formation is composed by a pair of satellites which perform the mission objectives working together. These two spacecrafts form with the Earth a triangular virtual structure, whose vertices are the satellites and the Earth CoMs.
It follows that the second relevant reference frame, called "Formation Local Orbital Frame" (FLOF), is the one used to define the formation dynamics and to describe the motion between the two satellites, whose positions from the origin of the inertial frame, i.e. the Earth CoM, is identified by the vectors $\vec{r_1}$ and $\vec{r_2}$. The centre of this frame is the middle

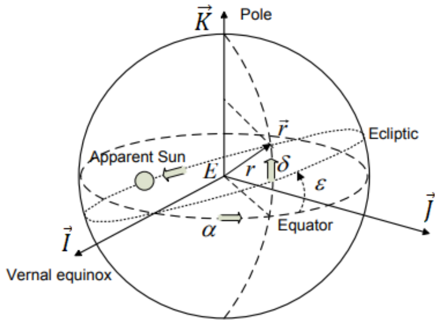

Figure 2.8: Geocentric Inertial Equatorial Frame [7]

point between the two satellites, i.e. the formation centre. In order to define the FLOF axes we introduce the following quantities:

$$\begin{aligned} \Delta\vec{r} &= \vec{r_1} - \vec{r_2} \\ \vec{r} &= \frac{\vec{r_1} + \vec{r_2}}{2} \end{aligned} \tag{2.41}$$

where $\Delta\vec{r}$ represents the relative distance between the satellites, and $\vec{r}$ stands for the mean formation radius. Therefore, the FLOF axes, as illustrated in Figure 2.9, are defined as:

$$\begin{aligned} \vec{o_1} &= \frac{\Delta\vec{r}}{d} \\ \vec{o_2} &= \frac{\frac{\vec{r}}{r} \times \vec{o_1}}{\sin\theta} \\ \vec{o_3} &= \vec{o_1} \times \vec{o_2} = \frac{\Delta\vec{r}}{d} \times \frac{\frac{\vec{r}}{r} \times \frac{\Delta\vec{r}}{d}}{\sin\theta} = \frac{1}{\sin\theta}\left(\left(\frac{\Delta\vec{r}}{d} \cdot \frac{\Delta\vec{r}}{d}\right)\frac{\vec{r}}{r} - \left(\frac{\Delta\vec{r}}{d} \cdot \frac{\vec{r}}{r}\right)\frac{\Delta\vec{r}}{d}\right) \\ &= \frac{1}{\sin\theta}\left(\frac{\vec{r}}{r} - \cos\theta\frac{\Delta\vec{r}}{d}\right) \end{aligned} \tag{2.42}$$

where d is the norm of the relative distance, r is the norm of the mean formation radius and θ is the angle between $\vec{r}$ and $\vec{o_1}$.

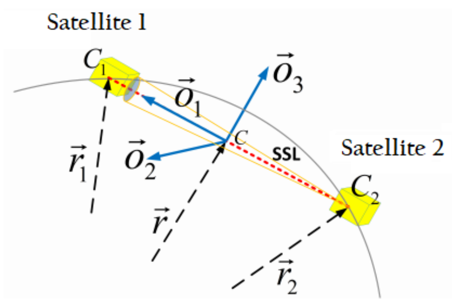

Figure 2.9: FLOF Coordinate Axis [10]

Spacecraft Body Frames of Reference

This section aims to describe the spacecraft body reference frame, that is a frame rotating with the spacecraft and with the origin in its CoM. Therefore, the definition of two body reference frames, i.e. one for each satellite, is needed. In our case, the first axis of the body frame, also called "sensor axis", is defined as aligned with the outcoming laser beam, while the third axis is assumed to be normal to the solar panels plane.
Thanks to the attitude and pointing control system, the body reference frames are guaranteed to be such that their sensor axis, which coincides with the spacecraft's optical axis, is aligned to the satellite-to-satellite line. Indeed, the nominal attitude of the two satellites is the one that guarantees they always point towards each other. In order to get to this in real conditions, it is necessary to implement a spacecraft attitude control.

2.6 Nominal Attitude

Since the main objective of this thesis is the development of a new kind of control system for the NGGM formation, from now on it is better to carry out all the analyzes and simulations without taking into account the errors due to the attitude and pointing control system. The idea is to substitute, for both satellites, the attitude dynamics with a function that provides a nominal attitude, that makes the spacecrafts be always oriented towards each other without the need to implement an attitude and pointing control system.
By introducing a function for the nominal attitude, we assume the presence of a closed-loop control, whose aim, as previously specified, is to guarantee the alignment of each spacecraft's optical axis to the satellite-to-satellite line.
The function to be implemented must provide as output, for each satellite, a reference quaternion that represents the nominal rotation needed to maintain time by time each spacecraft aligned with the inter-satellite line. Moreover, the same function must also provide the spacecraft angular velocity vector needed for the disturbance analysis.
For each spacecraft the nominal attitude is introduced as a set of unitary orthogonal vectors

$$\begin{aligned} &\{\vec{I_1}, \vec{J_1}, \vec{K_1}\} \\ &\{\vec{I_2}, \vec{J_2}, \vec{K_2}\} \end{aligned} \tag{2.43}$$

which represent the axes of the two nominal body frames of reference, centered respectively in the CoMs of Satellite 1 (Sat-1) and Satellite 2 (Sat-2). Therefore, the two nominal reference frames are defined as

$$\begin{aligned} R_1 &= \{C_1, \vec{I_1}, \vec{J_1}, \vec{K_1}\} \\ R_2 &= \{C_2, \vec{I_2}, \vec{J_2}, \vec{K_2}\} \end{aligned} \tag{2.44}$$

The only important requirement for the definition of these body frames is that the two satellites must point towards each other, thus we can orient the $\vec{I_2}$ axis of Sat-2 towards Sat-1, and conversely the $\vec{I_1}$ axis of Sat-1 in the opposite direction with respect to $\vec{I_2}$. Since, by definition, the $\vec{o_1}$ axis of the FLOF frame is pointing towards Sat-1 along the inter-satellite line, the body frame of Sat-2 can be chosen equal to the FLOF frame, defining its axes in the same way of the FLOF axes:

$$
\begin{aligned}
\vec{I_2} &= \frac{\Delta\vec{r}}{d} \\
\vec{J_2} &= \frac{\frac{\vec{r}}{r} \times \vec{o_1}}{\sin\theta} \\
\vec{K_2} &= \vec{I_2} \times \vec{J_2} = \frac{\Delta\vec{r}}{d} \times \frac{\frac{\vec{r}}{r} \times \frac{\Delta\vec{r}}{d}}{\sin\theta} = \frac{1}{\sin\theta}((\frac{\Delta\vec{r}}{d} \cdot \frac{\Delta\vec{r}}{d})\frac{\vec{r}}{r} - (\frac{\Delta\vec{r}}{d} \cdot \frac{\vec{r}}{r})\frac{\Delta\vec{r}}{d}) \\
&= \frac{1}{\sin\theta}(\frac{\vec{r}}{r} - \cos\theta\frac{\Delta\vec{r}}{d})
\end{aligned}
\tag{2.45}
$$

Therefore, the axes of Sat-2 body frame are oriented as depicted in Figure 2.10 (b):

- $\vec{I_2}$ lies along the satellite-to-satellite direction and points towards Sat-1
- $\vec{J_2}$ is perpendicular to the triangle plane
- $\vec{K_2}$ forms with the previous axes a right handed frame

Consequently, to obtain the nominal attitude of Sat-1, the axes of its body frame must be defined as shown in Figure 2.10 (a):

- $\vec{I_1}$ lies along the satellite-to-satellite direction, pointing towards Sat-2
- $\vec{J_1}$ is perpendicular to the triangle plane, in the opposite direction with respect to $\vec{J_2}$
- $\vec{K_1}$ forms a right handed frame with $\vec{I_1}$ and $\vec{J_1}$.

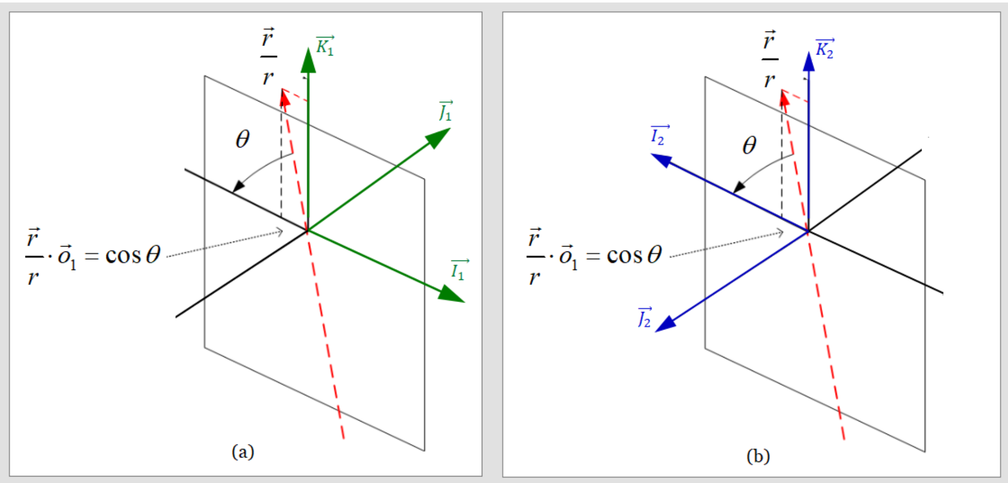

Figure 2.10: Nominal Attitude of Satellite 1 (a) and Satellite 2 (b)

From Figure 2.10 (a) it is easy to see that the nominal attitude of Sat-1 can be obtained rotating the axes of Sat-2 body frame of 180° about the $\vec{K_2}$ axis.

To this purpose, let's call $\mathbf{K_{2i}} = \begin{bmatrix} k_{2ix} \\ k_{2iy} \\ k_{2iz} \end{bmatrix}$ the vector $\vec{K_2}$ expressed in the inertial frame and let's define the DCM matrix T which allows the rotation of each axis of Sat-2 body frame of an angle β=180° about $\mathbf{K_{2i}}$:

$$T = \begin{bmatrix} k_{2ix}^2(1-c\beta)+c\beta & k_{2ix}k_{2iy}(1-c\beta)-k_{2iz}s\beta & k_{2ix}k_{2iz}(1-c\beta)+k_{2iy}s\beta \\ k_{2ix}k_{2iy}(1-c\beta)+k_{2iz}s\beta & k_{2iy}^2(1-c\beta)+c\beta & k_{2iy}k_{2iz}(1-c\beta)-k_{2ix}s\beta \\ k_{2ix}k_{2iz}(1-c\beta)-k_{2iy}s\beta & k_{2iy}k_{2iz}(1-c\beta)+k_{2ix}s\beta & k_{2iz}^2(1-c\beta)+c\beta \end{bmatrix} \tag{2.46}$$

Using the notation $\mathbf{I_{1i}}$,$\mathbf{J_{1i}}$,$\mathbf{K_{1i}}$ and $\mathbf{I_{2i}}$,$\mathbf{J_{2i}}$,$\mathbf{K_{2i}}$ respectively for Sat-1 and Sat-2 axes in the inertial frame, the following relation holds:

$$\begin{aligned} \mathbf{I_{1i}} &= T\mathbf{I_{2i}} \\ \mathbf{J_{1i}} &= T\mathbf{J_{2i}} \\ \mathbf{K_{1i}} &= T\mathbf{K_{2i}} \end{aligned} \tag{2.47}$$

It is worth noticing that, since $\mathbf{K_{2i}}$ is the axis of rotation, it is the only vector which remains unchanged by the T matrix above defined, and so it follows that $\mathbf{K_{1i}} = \mathbf{K_{2i}}$.
The axes of the two satellites in the inertial frame define two rotation matrices that represent the rotations needed to guarantee their nominal attitude:

$$\begin{aligned} R_1 = \begin{bmatrix} \mathbf{I_{1i}} & \mathbf{J_{1i}} & \mathbf{K_{1i}} \end{bmatrix} = \begin{bmatrix} i_{1ix} & j_{1ix} & k_{1ix} \\ i_{1iy} & j_{1iy} & k_{1iy} \\ i_{1iz} & j_{1iz} & k_{1iz} \end{bmatrix} \\ R_2 = \begin{bmatrix} \mathbf{I_{2i}} & \mathbf{J_{2i}} & \mathbf{K_{2i}} \end{bmatrix} = \begin{bmatrix} i_{2ix} & j_{2ix} & k_{2ix} \\ i_{2iy} & j_{2iy} & k_{2iy} \\ i_{2iz} & j_{2iz} & k_{2iz} \end{bmatrix} \end{aligned} \tag{2.48}$$

Finally, by using the formulas which allow to represent a rotation in quaternion form, it is possible to obtain the two spacecrafts nominal attitude quaternions.
The nominal attitude of the two satellites above defined, together with the formation triangular structure is depicted in Figure 2.11.

2.6.1 Satellites' Angular Rate

After having described the nominal attitude of the two body frames, it is worth to define also their angular rates, needed for the derivation of the disturbance forces and torques. The angular rate of each satellite is composed by two contributions; indeed, each body frame is centred in the spacecraft CoM which rotates on the orbit around the Earth, and is affected by an additional rotation to always maintain the nominal attitude.
Let's start with the definition of the angular rate of Sat-2 body frame $R_2 = \{C_2, \vec{I_2}, \vec{J_2}, \vec{K_2}\}$ about its own axes.
In order to determine the components of $\vec{\omega_2} = \omega_{2x}\vec{I_2} + \omega_{2y}\vec{J_2} + \omega_{2z}\vec{K_2}$, we can consider an infinitesimal rotation about each axis. For instance, let's analyse what happens applying

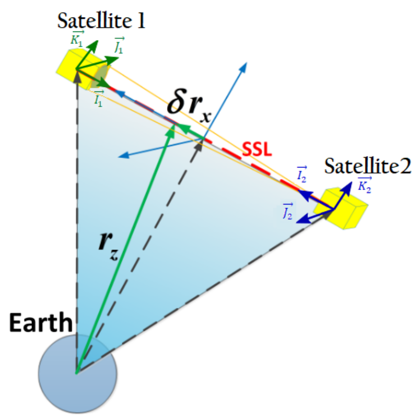

Figure 2.11: Formation Triangle and Satellites Nominal Attitude [11]

an infinitesimal rotation $d\delta$ about $\vec{J_2}$. This operation causes a rotation of the other two axes $\vec{I_2}$ and $\vec{K_2}$. The variation of $\vec{I_2}$ can be expressed in the following way:

$$\frac{d\vec{I_2}}{dt} = \lim_{\Delta t \to 0} \frac{\vec{I_2}(t+\Delta t) - \vec{I_2}(t)}{dt} \tag{2.49}$$

Then, rewriting $\vec{I_2}(t+\Delta t)$ as the sum of its projections on $\vec{I_2}$ and $\vec{K_2}$ and recalling that for small angles $\cos(\Delta\delta) \sim 1$ and $\sin(\Delta\delta) \sim \Delta\delta$, we obtain:

$$\begin{aligned} \frac{d\vec{I_2}}{dt} &= \lim_{\Delta t \to 0} \frac{\cos(\Delta\delta)\vec{I_2} - \sin(\Delta\delta)\vec{K_2} - \vec{I_2}(t)}{dt} = \lim_{\Delta t \to 0} -\frac{\Delta\delta \vec{K_2}}{\Delta t} = -\frac{d\delta \vec{K_2}}{dt} = \\ &= -\omega_{2y}\vec{K_2} \implies \omega_{2y} = -\frac{d\vec{I_2}}{dt} \cdot \vec{K_2} = -\dot{\vec{I_2}} \cdot \vec{K_2} \end{aligned} \tag{2.50}$$

In the same way, considering the variation of $\vec{K_2}$ due to an infinitesimal rotation $d\delta$ about the $\vec{J_2}$ axis, the component ω_{2y} can be also obtained in the following way,

$$\omega_{2y} = \frac{d\vec{K_2}}{dt} \cdot \vec{I_2} = \dot{\vec{K_2}} \cdot \vec{I_2} \tag{2.51}$$

Thus, repeating the process with the other two axes, i.e. considering infinitesimal rotations $d\delta$ about $\vec{I_2}$ and $\vec{K_2}$, the following set of fundamental equations is obtained:

$$\begin{aligned} \omega_{2x} &= \frac{d\vec{J_2}}{dt} \cdot \vec{K_2} = \dot{\vec{J_2}} \cdot \vec{K_2} = -\frac{d\vec{K_2}}{dt} \cdot \vec{J_2} = -\dot{\vec{K_2}} \cdot \vec{J_2} \\ \omega_{2y} &= -\frac{d\vec{I_2}}{dt} \cdot \vec{K_2} = -\dot{\vec{I_2}} \cdot \vec{K_2} = \frac{d\vec{K_2}}{dt} \cdot \vec{I_2} = \dot{\vec{K_2}} \cdot \vec{I_2} \\ \omega_{2z} &= \frac{d\vec{I_2}}{dt} \cdot \vec{J_2} = \dot{\vec{I_2}} \cdot \vec{J_2} = -\frac{d\vec{J_2}}{dt} \cdot \vec{I_2} = -\dot{\vec{J_2}} \cdot \vec{I_2} \end{aligned} \tag{2.52}$$

These equations allow to write the angular rate of Sat-2 body frame as $\vec{\omega_2} = \omega_{2x}\vec{I_2} + \omega_{2y}\vec{J_2} + \omega_{2z}\vec{K_2}$.

Going more into detail, to determine the components ω_{2x}, ω_{2y} and ω_{2z}, it is necessary to compute the derivative of the axis vectors:

$$
\begin{aligned}
\dot{\vec{I_2}} &= \frac{\Delta\vec{v}}{d} - \frac{\dot{d}}{d}\vec{I_2} \\
\dot{\vec{J_2}} &= \frac{d}{dt}\Big(\frac{\frac{\vec{r}}{r}\times\vec{I_2}}{\sin\theta}\Big) \\
&= \frac{1}{\sin\theta}\Big(\frac{\vec{v}}{r} - \frac{\dot{r}\vec{r}}{r^2}\Big)\times\vec{I_2} + \frac{1}{sin\theta}\frac{\vec{r}}{r}\times\dot{\vec{I_2}} - \frac{\frac{\vec{r}}{r}\times\vec{I_2}}{\sin^2\theta}\cos\theta\dot{\theta} \\
&= \frac{1}{sin\theta}\frac{\vec{v}}{r}\times\vec{I_2} + \frac{1}{sin\theta}\frac{\vec{r}}{r}\times\Big(\frac{\Delta\vec{v}}{d} - \frac{\dot{d}}{d}\vec{I_2}\Big) - \frac{\dot{r}}{r}\vec{J_2} - \vec{J_2}\frac{\cos\theta}{\sin\theta}\dot{\theta} \\
&= \frac{1}{sin\theta}\frac{\vec{r}}{r}\times\frac{\Delta\vec{v}}{d} - \Big(\frac{\dot{r}}{r} + \frac{\dot{d}}{d} + \frac{\cos\theta}{\sin\theta}\dot{\theta}\Big)\vec{J_2} + \frac{1}{\sin\theta}\frac{\vec{v}}{r}\times\vec{I_2} \\
\dot{\vec{K_2}} &= \dot{\vec{I_2}}\times\vec{J_2} + \vec{I_2}\times\dot{\vec{J_2}}
\end{aligned}
\tag{2.53}
$$

Then, using the formulas written in the Equation 2.52, the three components of Sat-2 angular rate, expressed with respect of its own axes, are:

$$
\begin{aligned}
\omega_{2x} &= \dot{\vec{J_2}}\cdot\vec{K_2} \\
&= \Big(\frac{1}{sin\theta}\frac{\vec{r}}{r}\times\frac{\Delta\vec{v}}{d} - \Big(\frac{\dot{r}}{r} + \frac{\dot{d}}{d} + \frac{\cos\theta}{\sin\theta}\dot{\theta}\Big)\vec{J_2} + \frac{1}{\sin\theta}\frac{\vec{v}}{r}\times\vec{I_2}\Big)\cdot\vec{K_2} \\
&= \frac{1}{\sin^2\theta}\Big(\frac{\vec{r}}{r}\times\frac{\Delta\vec{v}}{d} + \frac{\vec{v}}{r}\times\frac{\Delta\vec{r}}{d}\Big)\cdot\Big(\frac{\vec{r}}{r} - \cos\theta\frac{\Delta\vec{r}}{d}\Big) \\
&= \frac{1}{\sin^2\theta}\Big(\frac{\vec{r}}{r}\cdot(\frac{\vec{v}}{r}\times\frac{\Delta\vec{r}}{d}) - \cos\theta\frac{\Delta\vec{r}}{d}\cdot(\frac{\vec{r}}{r}\times\frac{\Delta\vec{v}}{d})\Big) \\
&= \frac{1}{\sin^2\theta}\Big((\frac{\vec{v}}{r} - \cos\theta\frac{\Delta\vec{v}}{d})\cdot(\frac{\Delta\vec{r}}{d}\times\frac{\vec{r}}{r})\Big) \\
&= -\frac{1}{\sin\theta}\Big((\frac{\vec{v}}{r} - \cos\theta\frac{\Delta\vec{v}}{d})\cdot\vec{J_2}\Big) \\
\omega_{2y} &= -\dot{\vec{I_2}}\cdot\vec{K_2} = -\Big(\frac{\Delta\vec{v}}{d} - \frac{\dot{d}}{d}\vec{I_2}\Big)\cdot\vec{K_2} = -\frac{\Delta\vec{v}}{d}\cdot\vec{K_2} \\
\omega_{2z} &= \dot{\vec{I_2}}\cdot\vec{J_2} = \Big(\frac{\Delta\vec{v}}{d} - \frac{\dot{d}}{d}\vec{I_2}\Big)\cdot\vec{J_2} = \frac{\Delta\vec{v}}{d}\cdot\vec{J_2}
\end{aligned}
\tag{2.54}
$$

With the same procedure, it is possible to compute the angular rate of Sat-1 body frame $R_1 = \{C_1, \vec{I_1}, \vec{J_1}, \vec{K_1}\}$ about its own axes. Recalling that $\vec{I_1} = -\vec{I_2}$, $\vec{J_1} = -\vec{J_2}$ and $\vec{K_1} = \vec{K_2}$ the derivative of the axis vectors are obtained as follows:

$$
\begin{aligned}
\dot{\vec{I_1}} &= \frac{d}{dt}(\vec{I_1}) = \frac{d}{dt}(-\vec{I_2}) = -\frac{d}{dt}(\vec{I_2}) = -\dot{\vec{I_2}} \\
\dot{\vec{J_1}} &= \frac{d}{dt}(\vec{J_1}) = \frac{d}{dt}(-\vec{J_2}) = -\frac{d}{dt}(\vec{J_2}) = -\dot{\vec{J_2}} \\
\dot{\vec{K_1}} &= \frac{d}{dt}(\vec{K_1}) = \frac{d}{dt}(\vec{K_2}) = -\dot{\vec{K_2}}
\end{aligned}
\tag{2.55}
$$

Finally, using again the formulas written in the Equation 2.52, the three components of the Sat-1 angular rate, expressed with respect of its own axes, are:

$$\begin{aligned} \omega_{1x} &= \dot{\vec{J_1}} \cdot \vec{K_1} = -\dot{\vec{J_2}} \cdot \vec{K_2} = -\omega_{2x} \\ \omega_{1y} &= -\dot{\vec{I_1}} \cdot \vec{K_1} = -(-\dot{\vec{I_2}}) \cdot \vec{K_2} = \dot{\vec{I_2}} \cdot \vec{K_2} = -\omega_{2y} \\ \omega_{1z} &= \dot{\vec{I_1}} \cdot \vec{J_1} = (-\dot{\vec{I_2}}) \cdot (-\vec{J_2}) = \dot{\vec{I_2}} \cdot \vec{J_2} = \omega_{2z}. \end{aligned} \tag{2.56}$$

It is noticeable that the first two components above computed are different in sign from the corresponding ones of Sat-2 due to the way in which we have defined the satellites' nominal attitude. However, actually, the angular rates of the two satellites can be represented by the same vector if expressed in the same frame of reference:

$$\begin{aligned} \vec{\omega_1} &= \omega_{1x}\vec{I_1} + \omega_{1y}\vec{J_1} + \omega_{1z}\vec{K_1} \\ &= -\omega_{2x}(-\vec{I_2}) - \omega_{2y}(-\vec{J_2}) + \omega_{2z}\vec{K_2} \\ &= \omega_{2x}\vec{I_2} + \omega_{2y}\vec{J_2} + \omega_{2z}\vec{K_2} = \vec{\omega_2} \end{aligned} \tag{2.57}$$

2.7 Simulations with Nominal Attitude

After having defined the satellites' nominal attitude and angular rate, we can substitute the spacecraft dynamic and kinematic blocks with a MATLAB function which takes as input the satellite's position and velocity and gives as output the reference body quaternion and the angular rate. As previously said, this function is used in place of the attitude and pointing control system in order to always guarantee the satellites' nominal attitude and to avoid considering in our study all the attitude errors.

In the following, some simulated results are presented, concerning in particular the satellite-to-satellite distance in order to highlight how its behaviour varies after the introduction of the satellites' nominal attitude. The simulation was performed with the system in free evolution, without yet considering any active control system. The objective is to show how fast the two satellites diverge from the nominal orbit, and consequently how much the satellite-to-satellite distance diverges from its nominal value $d_{nom} = 100\ km$, due to the system instability. The expected result is that the distance between the two satellites, after introducing the nominal attitude, will diverge slower than before. Indeed, before forcing the nominal attitude, the two satellites were subject only to the disturbing torques and forces which caused a very fast divergence from the satellites' nominal position. With the introduction of this function instead we assume the presence of a perfect control action which counteracts the disturbing torques, giving the satellites the right rotation to maintain the alignment of their optical axis with the inter-satellite line.

Figure 2.12 represents the comparison of the satellite-to-satellite distance behaviour before and after the introduction of this function. Looking at the simulated result we can notice that, as expected, forcing the nominal attitude the divergence of the distance from the nominal value is significantly slower than before. The simulation was performed over a period of 150 orbits.

Figure 2.13 depicts separately the two cases under study , highlighting when the distance plots reach a limit of the 10% from the distance nominal value.

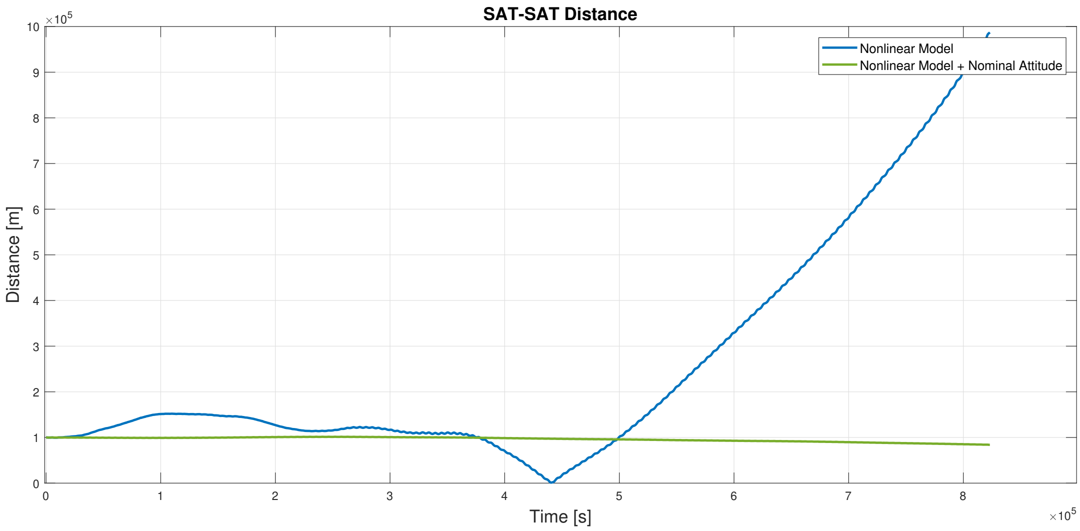

Figure 2.12: No-Control vs Nominal Attitude

The line in green, that represents the plot of the formation distance with nominal attitude, shows a divergence of the 10% from the nominal value at a time more or less equal to 126 orbits, indeed considering that an orbital period lasts for 5487 s, at $t = 6.916 \times 10^5$ s the satellite-to-satellite distance reduces up to 90 km. Contrariwise, the line in blue, that represents the plot of the formation distance without nominal attitude, reaches the limit of the 10% from the nominal value, or rather arrives at 110 km, after just 3.892×10^4 s, that means after only 7 orbits.

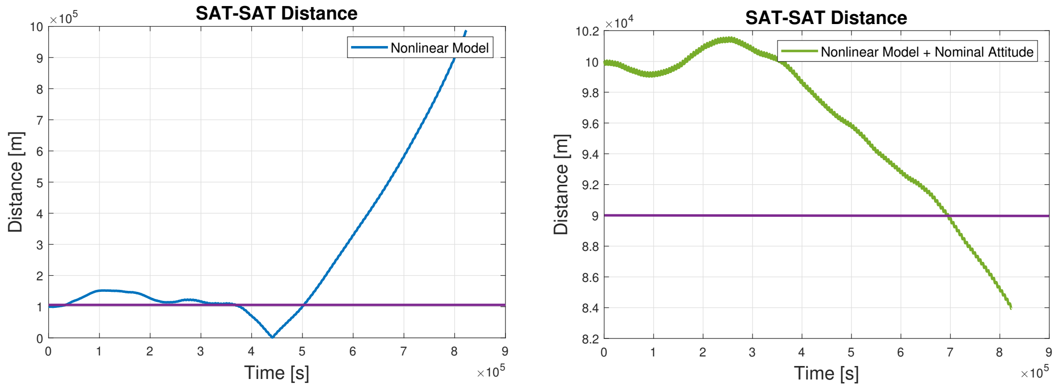

Figure 2.13: Bound of 10% From the Nominal Value

Chapter 3

Drag-Free Control

This chapter is intended to generally explain the concepts behind the drag-free control. As already mentioned, after GOCE and GRACE, all the future missions about Earth gravimetry will make use of satellite formations composed by free-falling proof-masses. The rationale behind this concept is the need to make the distance variations not subject to non-gravitational disturbances and consequently able to identify any kind of variation in the planetary local gravity field. For this purpose, the satellites must be controlled to be drag-free [10].

The drag-free control is designed as a faster inner loop with respect to the attitude and formation control, which takes as input the measurement of external non-gravitational accelerations (both linear and angular). Indeed, looking at the actuation system, both the commanded force and torques are supplied by a thruster assembly driven by quite precise measurements coming from GOCE-class accelerometers, as proof of the numerous common points with the previous missions [10].

In order to take into account both linear and angular non-gravitational disturbances, within this study we will distinguish between linear and angular drag-free control. These two problems are here addressed using the EMC perspective.

The main objective of the linear drag-free control is to make the satellites free-falling flying masses [10]. This objective can be achieved by estimating and then rejecting, by means of a proper actuation system, the disturbance forces acting upon the satellites. Similarly, the main objective of the angular drag-free control is to zero all the disturbance torques affecting the satellites [11].

Despite the several contact points with GOCE, NGGM can rely on the progresses made in the field of propulsion systems and thanks to the technological improvement its satellites will be made three-axially drag-free, differently from GOCE's satellites which have only one drag-free axis, namely the along-track one [10].

Finally, it is worth to point out that the linear and the angular drag-free controls make use of the same models and control schemes with the only difference in the values used to properly tune the control gains. For this reason, here we will take into account only the linear drag-free control.

This chapter starts providing a general understanding about drag-free modelling and control, basing on the experience gained from GOCE mission, and finally ends showing some simulated results.

3.1 Drag-Free Concept

In NGGM implementation, the linear drag-free control makes use of some proof-masses (also called test-masses), inserted within a cage inside the spacecraft. These test-masses are positioned according to some geometry to create a multi-directional gradiometer [10]. They are the most important element for the development of a drag-free control system.
The linear drag-free control can be realized exploiting two possible different strategies. The first strategy employs a free moving proof-mass placed within a cage and consists in using the control law to command the spacecraft in order to track and centre in the cage the proof-mass. Thus, instead of directly cancelling the non-gravitational forces, the satellite is here controlled to be drag-free by forcing it to maintain the test-mass in the right position and attitude inside the cage [10]. The control algorithm is fed by sensors which estimate the proof-mass position and is actuated by a thruster assembly mounted on the cage. The drawback of this technique consists in the practical impossibility for the satellite to track more than one proof-mass [10].
The second strategy instead, makes use of the accelerometer concept, illustrated in Figure 3.1. This technique consists in controlling the spacecraft to be drag-free by directly estimating and rejecting the non-gravitational forces. In this way, since the spacecraft is made drag-free, the motion of the proof-masses, that in this case can be also more than one, is shaped only by the gravity force [10]. Indeed, with this solution, the system is able to leverage many proof-masses at the same time, positioning them in a certain configuration in order to form a gradiometer [10].
With this second strategy, the test-mass is hooked with an active suspension system that keeps the mass in its central position and uses the suspension force to measure the non-gravitational effects and feed the control law [10].
To talk about the control perspective, let's firstly define with $\boldsymbol{r}$ and $\boldsymbol{v}$ the spacecraft radius and velocity vectors. The following standard dynamic equations hold:

$$\begin{aligned}\dot{\boldsymbol{r}}(t) &= \boldsymbol{v} \\ \dot{\boldsymbol{v}}(t) &= \boldsymbol{g}(\boldsymbol{r}(t)) + \mathcal{R}_b^i \frac{\boldsymbol{F}_u(t) + \boldsymbol{F}_d(t)}{m}\end{aligned} \tag{3.1}$$

Consequently, the drag-free control ideally implies:

$$\boldsymbol{a}(t) = \frac{\boldsymbol{F}_u(t) + \boldsymbol{F}_d(t)}{m} = 0 \tag{3.2}$$

where $\boldsymbol{g}(\boldsymbol{r}(t))$ is the gravitational acceleration, $\boldsymbol{a}(t)$ are the external non-gravitational accelerations, while $\boldsymbol{F}_u(t)$ and $\boldsymbol{F}_d(t)$ are, respectively, the drag-free command force and the non-gravitational forces, coming from environment disturbances and atmospheric drag.
However, despite the introduction of the drag-free control, $\boldsymbol{a}(t)$ cannot be exactly equal to zero, due to the practical impossibility to perfectly reject all the non-gravitational effects [11]. This problem let us to introduce the concept of drag-free residual non-gravitational acceleration, that according to the NGGM requirements, must be constrained to remain very limited, both in terms of time and frequency [10].

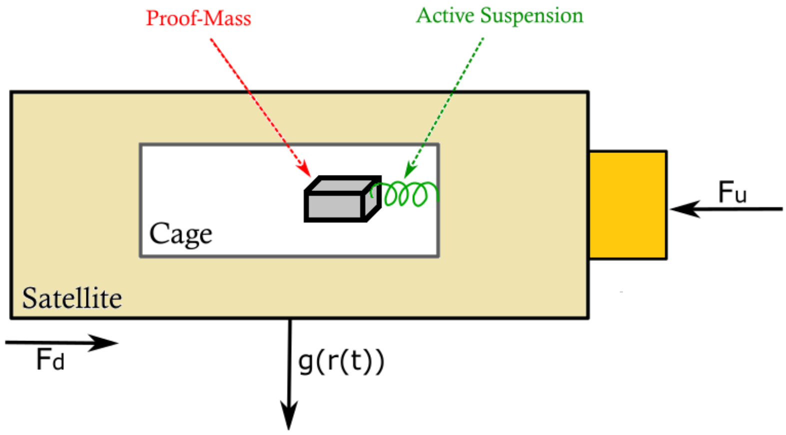

Figure 3.1: Drag-free Accelerometer Strategy

3.2 Control Architecture

As already mentioned, the drag-free control was realized following the EMC methodology. Indeed, thanks to this technique, it is possible to estimate the non-gravitational forces using the EMC disturbance dynamics. This possibility makes the EMC one of the most suitable methods to address the drag-free control problem.
The main issue for the estimation of these forces consists in their high-variability due to the altitude and the solar and geomagnetic activity [10]. Therefore, the estimation of the non-gravitational disturbances is performed adopting a third order stochastic and parameter-free disturbance dynamics and the rejection of the estimated disturbing forces is obtained (up to a certain frequency and accuracy) by means of a control law [10].
In this section a brief overview about the main parts composing the control architecture is provided. We consider in the following a single degree of freedom, to be replicated for the three spacecraft axis.
Let's recall that the linear and the angular drag-free control are based on the same control schemes, thus here for simplicity we will focus only on the first.
According to the EMC methodology, the control scheme is based on a state predictor, that comes from the embedded model of the sensors-to-actuators drag-free chain, plus a control law.
The simplified block-diagram of the drag-free models of a single satellite is shown Figure 3.2.
As we can notice, the same command signal feeds both the fine model/plant and the control unit. Specifically, the system to be controlled, i.e. the plant, is driven by a digital command $\tilde{\boldsymbol{u}}_t$ which feeds the thruster assembly, and gives as output the digital measurements $\tilde{\boldsymbol{y}}_a$ exiting from the accelerometer package [10]. The plant includes three main parts: the environment forces and torques to accurately describe the non-gravitational effects due to the external world, the accelerometer errors, trated as disturbances coming from formation and attitude control models, and the dynamics of thrusters and accelerometers [10]. Within the Embedded Model, instead, we can distinguish two parts: the controllable dynamics $\boldsymbol{M}$, that contains the nominal value of the relevant model parameters, and the disturbance

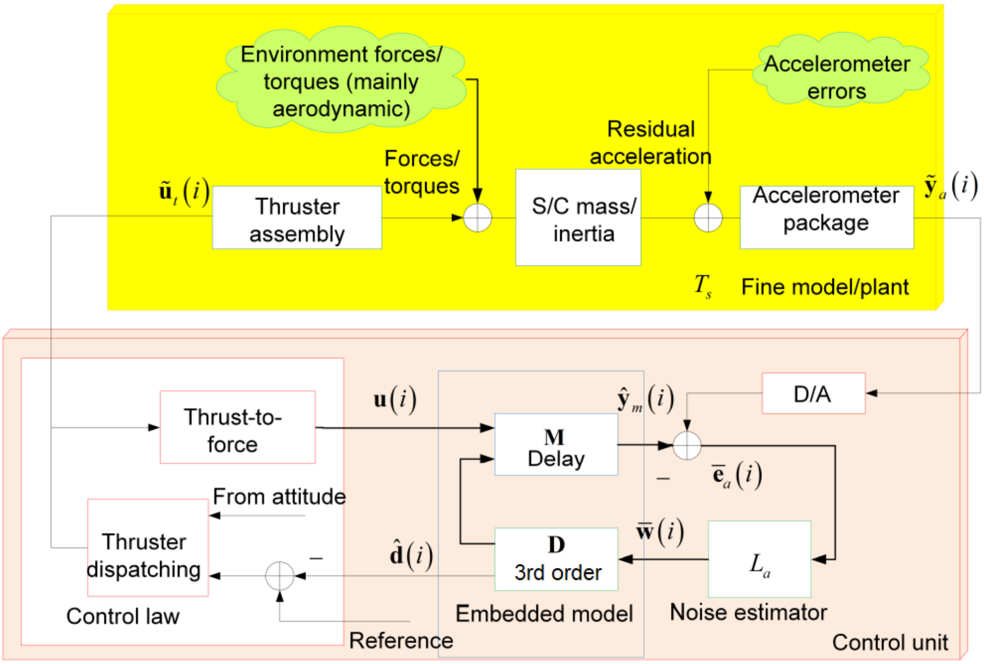

Figure 3.2: Block Diagram of the Drag-Free Model of a Single Satellite [10]

dynamics $\boldsymbol{D}$, that is usually parameter free [10]. Besides the Embedded Model, in the Control Unit there is also the Noise Estimator, whose gains L_a are tuned by means of simulations or tests and then maintained constant, and the Control Law that provides the digital command $\tilde{\boldsymbol{u}}_t$ necessary to reject the estimated disturbances [10].
Going more into detail, the overall block scheme of the single-axis drag-free control unit is depicted in Figure 3.3. As illustrated, the complete control law is obtained by summing the command forces given by the drag-free control and the formation control.
Summarizing what has been said so far, in the overall drag-free controller block scheme we can highlight the presence of three main components:

- The Controllable Dynamics, which is obtained with a delay block that shapes the input-output relation between thruster command and accelerometer measurements.

- The Disturbance Dynamics, which, in order to satisfy the NGGM demanding requirements, needs a third order stochastic dynamics to fit in a reliable way the high frequency spectral density of the non-gravitational acceleration.

- The Noise Estimator, whose gains constitute a simple static estimator (such as a Kalman Filter) with the aim of realizing the noise vector components as a linear function of the measured model error.

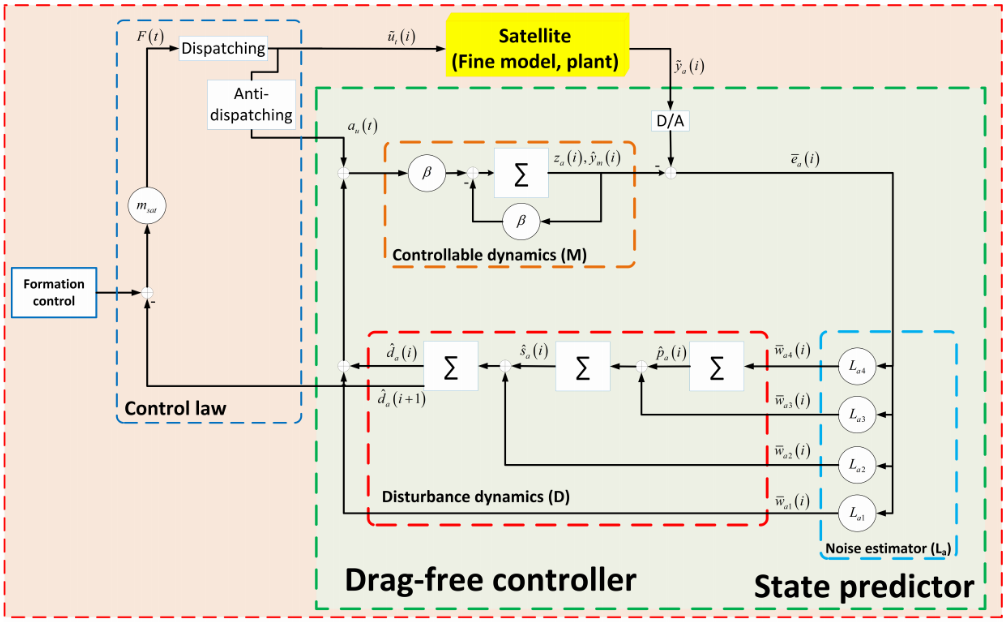

Figure 3.3: Overall Block Scheme of a Single-Axis EMC Drag-Free Controller [10]

3.3 Simulations with Drag-Free Control

After having explained the concept around the drag-free control, in the following we will illustrate some simulated results obtained introducing the drag-free control block inside the Simulink scheme presented in Figure 2.3. With this last modification, the simulator adopted is composed by the nonlinear model previously described, plus a new block containing the drag-free control system; this block receives as input the accelerometers measurement of the non-gravitational body forces and gives as output the drag-free command. Then, the command exiting from the drag-free control block is summed to the disturbance forces coming from the atmospheric disturbance model in order to obtain the total non-gravitational body forces, as depicted in Figure 3.4. Indeed, the overall force and torque acting on the spacecraft are given by the resultant of the environment disturbances and the control forces. At this purpose, later also the formation control command force will be added to this sum. The Simulink scheme presented in Figure 3.4 is the one that includes the nominal attitude function in place of the kinematic and dynamic blocks.
The simulation was performed over a period of 150 orbits as the one described in Section 2.7. In this way it is possible to make a further comparison on the formation distance behaviour with respect to the cases previously illustrated. However, before checking the distance behaviour, it is worth to take a look at the drag-free command force, in order to have an idea about its order of magnitude and its shape. Figure 3.5 shows the three body coordinates of the drag-free command force acting on both satellites. The control actions applied at the two satellites are similar in magnitude, but have two components, namely the first and the second body components, with the opposite sign. This can be due to the way in which we defined the satellites' nominal attitude. Indeed, let's recall that the nominal body reference frames were chosen with the first and the second coordinates in

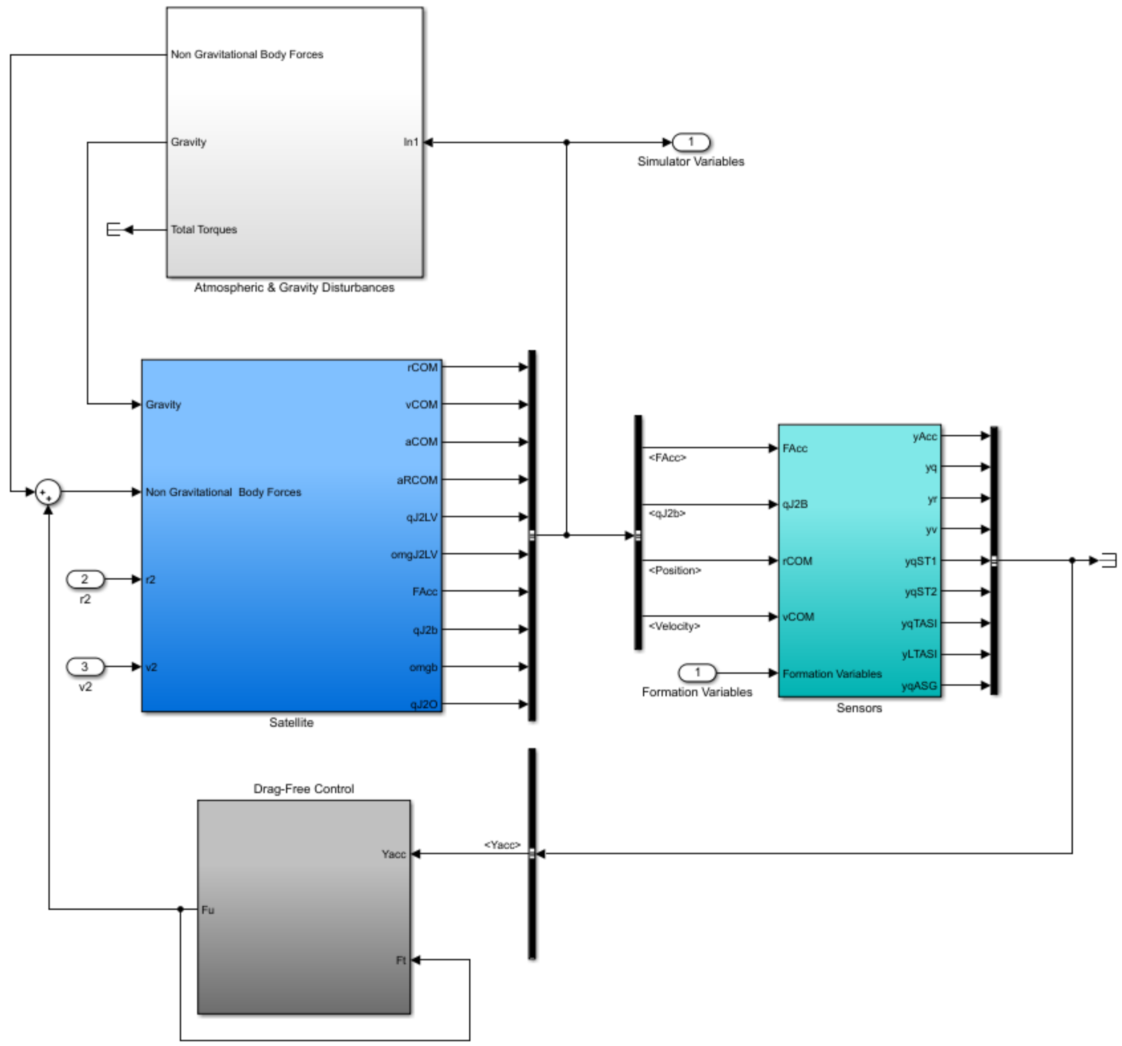

Figure 3.4: Satellite Block Scheme after Introducing the Drag-Free Control

the opposite direction to each other. Further, it is possible to compare the command force with the total disturbance force coming from the atmospheric disturbance block. Basing on what has been said so far, we expect that these two forces have more or less the same magnitude but opposite sign since, by definition, the aim of the drag-free control is to cancel the non-gravitational disturbances due to the environment effects. At this purpose, in Figure 3.6 is reported the plot of the sum of these two quantities, for both satellites. As we can notice, in both cases this sum results approximately equal to zero, pointing out that the drag-free control works as expected, rejecting with a good accuracy the disturbance forces.
Now let's focus on the formation distance, that is the variable on which this study is centered. In Figure 3.7 the time profile of the satellite-to-satellite distance obtained with the addition of the drag-free control is added to the plots reported in Section 2.7, stressing a further improvement with respect to the previous cases since in this last simulation the

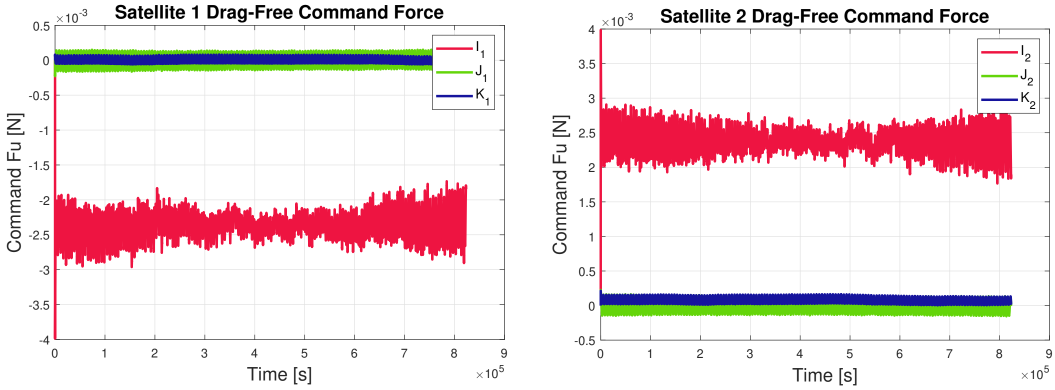

Figure 3.5: Drag-Free Command Force

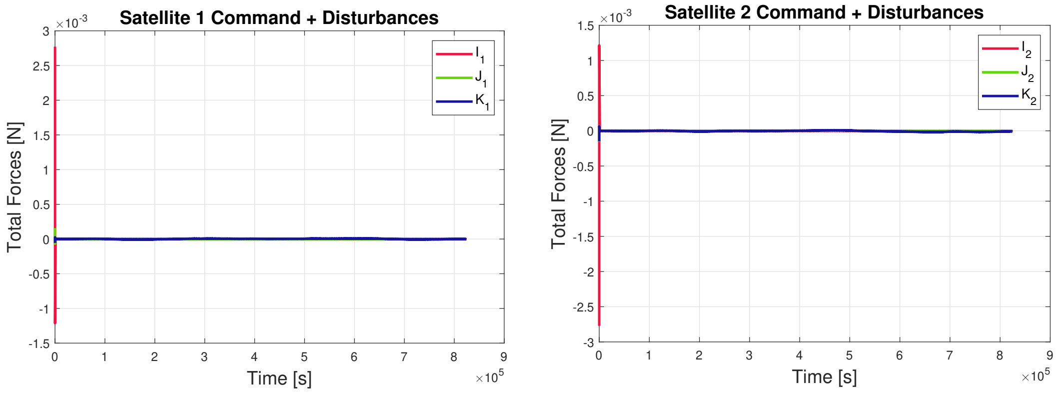

Figure 3.6: Satellites Total Non-Gravitational Forces: Command + Disturbances

formation distance remains inside the limit of the 10% from the nominal value $d_{nom} = 100$ km for more than 150 orbits.

3.3.1 No Nominal Attitude vs Nominal Attitude

Another interesting comparison that we can do is the one depicted in Figure 3.8, whose aim is to collate the time profile of the formation distance presented so far with the one obtained introducing the drag-free control inside the nonlinear model reported in Chapter 3 before developing the function to force the satellites' nominal attitude. The two plots in the figure show an almost identical behaviour at the beginning, with a very slow divergence in both cases. However, even if the formation distance remains in any case close to the nominal value of $d_{nom} = 100$ km, the nominal attitude introduces an even greater improvement, furtherly slowing the divergence. Since the difference between the two simulations seems to be small and insignificant, in order to highlight the importance of using the nominal attitude, let's plot the drag-free commands acting on the satellites in the two cases. These plots, shown in Figure 3.9, point out that, even if the satellite-to-satellite distance seems similar, the command is very different and specifically in case of nominal attitude it is remarkably smaller. For the plots in Figure 3.9, a simulation time of 20 orbits has been used since

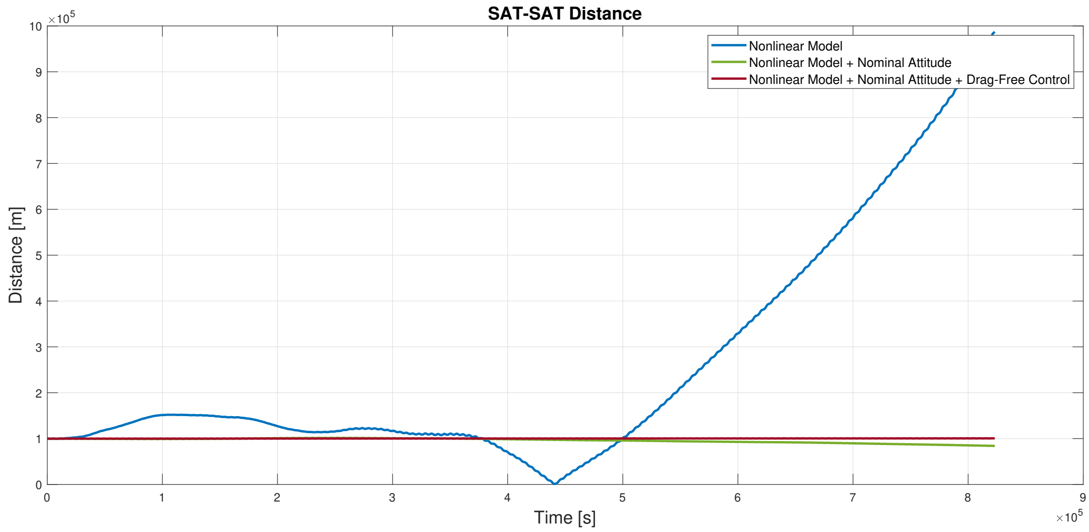

Figure 3.7: No-Control vs Nominal Attitude vs Drag-Free control

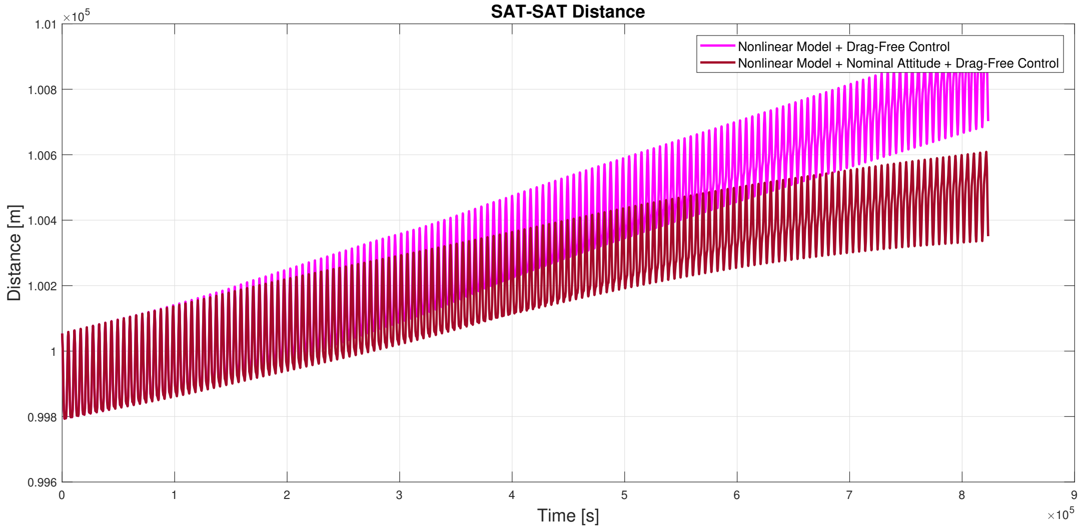

Figure 3.8: Drag-Free Control: No Nominal Attitude vs Nominal Attitude

what matters to compare is only the order of magnitude of the variables. The difference between the two cases is particularly due to the fact that using the nominal attitude, the drag disturbance is smaller. Hence, we can say that using the nominal attitude allows us to do a more meaningful analysis on disturbances, to avoid too large drag-free commands and to easily control the formation distance.

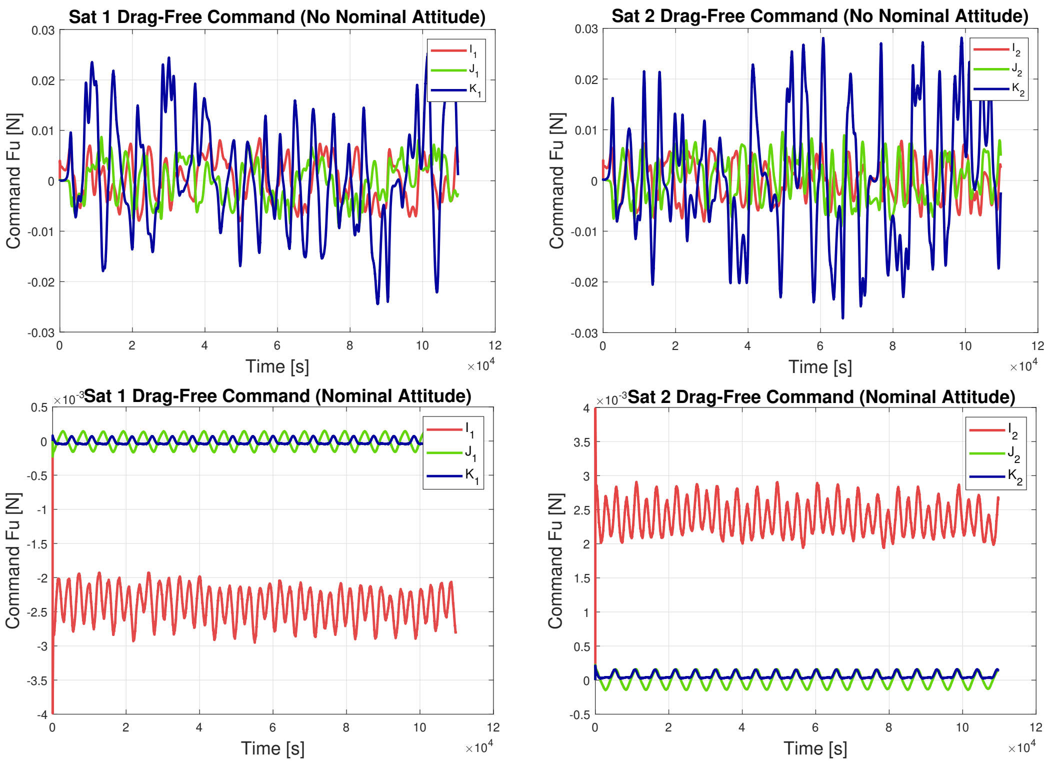

Figure 3.9: Drag-Free Command Force: No Nominal Attitude vs Nominal Attitude

Chapter 4

Formation Control

This chapter is devoted to introduce the main features of the NGGM orbit and formation control problem and to explain the rationale behind the strategy proposed for its solution. The ambitious objective of Formation Control consists in guaranteeing the system long-term stability by simultaneously counteracting bias and drift of residual drag-free accelerations. Let's recall that the expression "formation" is related to a group of cooperating satellites which perform the mission objective working together and realizing their tasks in place of a unique, bigger, spacecraft. Thus, Formation Control should allow the concurrent monitoring of both satellites' altitude and relative distance in order to maintain them inside the required intervals. Let's recall that the nominal values of spacecraft orbital altitude and satellite-to-satellite distance have been chosen with the aim of maximizing the capability to measure the gravity signal.
The Table 4.1 collects all the scientific requirements concerning the orbit and formation control. These requirements are split into distance, radial and lateral variations. In partic-

Variable	Bound	Unit
Formation distance variation	$\eta_d = 10\%$	%(distance)
Formation radial variation	$\eta_r = 2\%$	%(altitude)
Formation lateral variation	$\eta_y = 1\%$	%(distance)

Table 4.1: NGGM Orbit and Formation Requirements

ular, the latter refers only to the in-line formation type, that envisages the two satellites flying on same nominal orbit but with different true anomalies. As it is evident from Table 4.1, the objective of Formation Control results in ensuring that the perturbations affecting the formation altitude and inter-satellite distance remain bounded during the mission lifetime, namely during a period of about 11 years in order to cover an entire solar cycle. This objective can be achieved by limiting the free response inside some bounds as well as cancelling as much as possible the secular components of residual drag-free accelerations.
The control unit previously designed for the NGGM Formation Control was realized using the Embedded Model Control methodology, explained in Section 1.4. As a matter of fact, this technique well fits the control problem under study, being able to guarantee the closed-loop stability of a model-based control law in presence of big parametric and structural

uncertainties.
This thesis work aims at studying the same problem by adopting a different control strategy. In particular, a NMPC-based framework has been implemented. Thus, this chapter is focused on the Formation Control design, implementation and simulations, by proposing a valid alternative solution with respect to the EMC. As a matter of fact, thanks to its advantages, the Model Predictive Control (MPC) has the ability to find an optimal control law managing at the same time state and input constraints and providing an online adaptation of the control strategy to possible variations of the process conditions.
Being the Model Predictive Control a particular branch of model-based design, for the NMPC internal prediction two LTI models have been explored in this study. The first model is based on the standard Hill-Clohessy-Wiltshire equations while the second one consists of an innovative integrated formation control (IFC) model that allows a common description of the formation altitude and satellite-to-satellite distance, by defining a specific orbital reference frame called Formation Local Orbital Frame (FLOF). Specifically, in the following, the theory behind the MPC technique and the two proposed models has been described in detail. Then, for each one of them, a comparison of the free evolution of its state variables with respect to the corresponding ones of the accurate nonlinear model described in Chapter 3 is presented. After having highlighted the greater effectiveness of the IFC model in approximating the real plant dynamics, an NMPC framework has been developed for the specific control problem under study, and numerous configurations of parameters have been tested and simulated.

4.1 Model Predictive Control

Model Predictive Control (MPC), also called Receding Horizon Control (RHC) is a modern feedback strategy widely adopted for industry applications, especially for linear processes. As the EMC, this advanced method, is a model-based design technique, but its advantage consists in the possibility to control a process by explicitly taking into account constraints on controls and states.
Linear MPC refers to a family of MPC schemes in which linear models are used to predict the system dynamics, considering only linear state and input constraints. Nevertheless, many systems are, in general, inherently nonlinear. In this cases, linear models are often inadequate to represent the behaviour of the system and nonlinear models have to be used [2], [13]. This is the rationale behind the NMPC, which is a variant of the standard MPC based on nonlinear models and/or nonlinear constraints.
Both MPC and NMPC requires an iterative solution of optimal control problems on a finite prediction horizon. This control technique is based on the idea to employ a dynamical MODEL of the plant to PREDICT the future behaviour of the variables of interest and compute an "optimal" CONTROL action. The need to use a model of the plant derives from the fact that in real applications the exact plant dynamics is seldom known.
Since the problem we are addressing is nonlinear, let's focus on the NMPC, considering a MIMO nonlinear system

$$\begin{aligned}\dot{x} &= f(x,u)\\ y &= h(x,u)\end{aligned} \tag{4.1}$$

where $x \in R^n$ is the state, $u \in R^{n_u}$ is the command input and $y \in R^{n_y}$ is the output.
It is assumed that the state is measured, otherwise an observer or a model in input-output form has to be used. The model contained in the NMPC algorithm is of the form

$$\begin{aligned} \dot{\hat{x}} &= \hat{f}(x, u) \\ \hat{y} &= \hat{h}(x, u) \end{aligned} \tag{4.2}$$

It is worth noticing that in the nominal case the prediction model is exactly equal to the real plant, that means $f = \hat{f}$ and $h = \hat{h}$.
The MPC strategy, illustrated in Figure 4.1, consists in solving on-line a finite horizon open loop optimal control problem based on measurements obtained online, with sampling time T_s. Let's denote these measurements with $x(t_k)$ with $t_k = T_s k$, $k = 0,1,\ldots$
At each time $t = t_k$, the controller exploits the model of the plant to predict the future dynamic behaviour of the system over the time interval $[t, t + T_p]$, where $T_p > T_s$ is called prediction horizon. This operation is obtained by the integration of Eq. 4.2 and gives as output the predicted system state and output at any time $\tau \in [t, t+T_p]$, in function of the initial state $x(t)$ and the input signal $u(t : \tau)$, that is the input signal in the interval $[t, \tau]$.

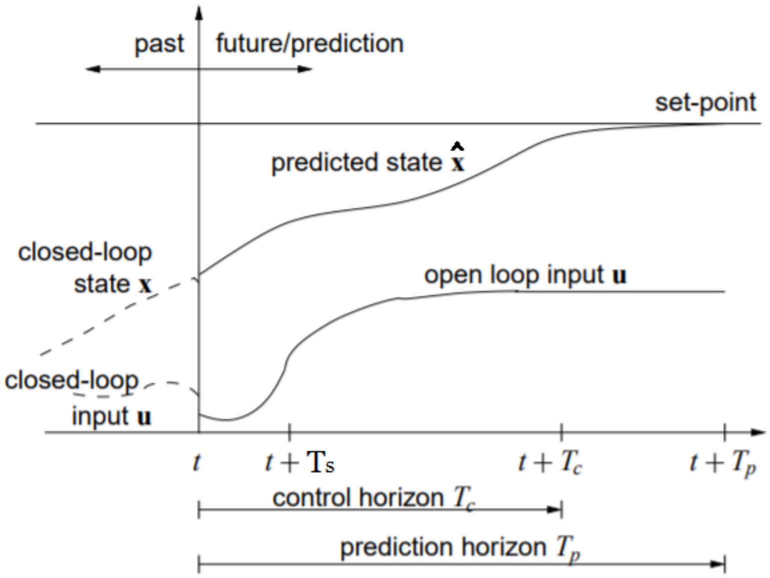

Figure 4.1: MPC Strategy [13]

Beside the prediction, at each time $t = t_k$, the controller determines an optimal input signal over a control horizon $T_c < T_p$, such that a predetermined open-loop performance objective functional is optimized. Broadly speaking, the objective is to look for an input signal able to generate the desired behaviour in the predicted output for $\tau \in [t, t + T_p]$.
The concept of desired behaviour is formalized by defining the objective functional

$$J(u(t : t + T_p)) = \int_t^{t+T_p} \|\tilde{y_p}(\tau)\|_Q^2 + \|u(\tau)\|_R^2 d\tau + \|\tilde{y_p}(t + T_p)\|_P^2 \tag{4.3}$$

where $\tilde{y}_p(\tau) = r(\tau) - \tilde{y}(\tau)$ is the predicted tracking error, $r(\tau) \in R^{n_y}$ is a reference to track and $\|.\|_Q^2$ represents a square weighted norm. In general, the square weighted norm of a vector $v \in R^n$ is defined as $\|v\|_Q^2 = v^T Q v = \sum_{i=1}^n q_i v_i^2$.
To set the controller we need to properly choose the weight matrices Q, R and P, which are diagonal matrices composed of non-negative elements. The optimal input signal $u^*(t : t+T_p)$ is chosen as the one minimizing the objective function $J(u(t : t+T_p))$. In particular, the goal is to minimize, at each time t_k, the tracking error square norm over a finite time interval, choosing in the correct way the weight matrix Q. The matrices P and R, instead, are used to give more importance to the final tracking error and to manage the trade-off between performance and command activity respectively. Further, the minimization of $J(u(t : t + T_p))$ is subject to the following constraints

$$\begin{aligned} &\hat{x}(\tau) = \hat{f}(x(\tau), u(\tau)), \hat{x}(t) = x(t), \tau \in [t, t + T_p] \\ &\hat{y}(\tau) = \hat{h}(x(\tau), u(\tau)) \end{aligned} \tag{4.4}$$

while additional constraints may be present on the predicted state/output and on the command input.
The optimization problem described above is generally convex in linear MPC, whereas in NMPC it is not necessarily convex anymore; for this reason, an efficient numerical algorithm is needed for its solution, providing in any case only a local minimum.
As depicted in Figure 4.1, the input is an arbitrary function of time, thus $u(t : t + T_p)$ can be seen as a vector with an infinite number of elements leading to an optimization problem that involves an infinite number of decision variables. To overcome the problem, it is often necessary to parametrize the input signal, choosing, for example, a piece-wise constant input over the sampling time T_s:

$$u(\tau) = u_p(\tau) = c_i \qquad for \begin{cases} \tau \in [t + (i-1)T_s, t + iT_s] \\ i = 1, \ldots, \frac{T_p}{T_s} \end{cases} \tag{4.5}$$

In the time interval $[t, t + T_p]$, the input signal $u^*(t : t + T_p)$ is an open-loop input since it depends on $x(t)$ but not on $x(\tau), \tau > t$. Thus, $u^*(t : t + T_p)$, if applied for the entire time interval $[t, t + T_p]$, does not perform a feedback action and it cannot increase the precision or reduce the errors. Consequently, in order to include some feedback mechanism, only the first input value $u^*(\tau) = u^*(t = t_k)$ is applied, keeping it constant until the next measurements becomes available, i.e. $\forall \tau \in [t_k, t_(k + 1)]$. This strategy is referred to as Receding Horizon. Then, using the measurements obtained at the successive sampling instant, the whole procedure of prediction and optimization is repeated to find a new input function, with the control and prediction horizons moving forwards.
Summing up, the mathematical formulation for NMPC algorithm is described below:

At time $t = t_k$, for $\tau \in [t, t + T_p]$,

1. The plant or its model is sampled in order to get the initial state $x(t_k)$ and to predict the system future behaviour over the prediction horizon T_p.

2. The optimization problem is solved in order to compute the minimizer

   $u^*(t:t+T_p) = argminJ(u(t:t+T_p))$

   subject to:

$$
\begin{aligned}
&\hat{x}(\tau) = \hat{f}(x(\tau), u(\tau)), \qquad \hat{x}(t) = x(t)\\
&\hat{y}(\tau) = \hat{h}(x(\tau), u(\tau))\\
&u(\tau) = u_p(\tau)\\
&\hat{x}(\tau) \in X_c, \qquad \hat{y}(\tau) \in Y_c, \qquad u(\tau) \in U_c\\
&u(\tau) = u(t+T_c), \qquad \tau \in [t+T_c, t+T_p]
\end{aligned}
$$

   The last constraint means that the command input is optimized from t to $t+T_c$, and then kept constant from $t+T_c$ to $t+T_p$. Note that, since the input is parametrized, the open loop optimal input is $u^*(\tau) = u_p^*(\tau)$.

3. According to the receding horizon strategy, only the first element of the minimizer is applied as present closed loop control action, i.e. $u(\tau) = u^*(t_k), \forall \tau \in [t_k, t_(k+1)]$.

4. The algorithm sets $k \leftarrow k+1$ and the procedure is repeated from step 1.

4.2 Hill-Clohessy-Wiltshire Equations

The model-based design control techniques, like EMC and MPC, foresee the presence of internal models used to compute the control action. At this purpose, let's introduce the Hill-Clohessy-Wiltshire (HCW) equations, which constitutes a model often used to analyse the relative motion of two spacecrafts in Earth-bound orbits. This analysis is usually carried out on the basis of simplifying assumptions, such as assuming that the reference spacecraft, called Target, follows a circular orbit about a central body, considered a point mass. This model could be a good choice for the study of several orbital manoeuvres, such as the "space rendezvous", which involves two spacecrafts approaching at a very close distance.
Since the in-line configuration of NGGM formation envisages a circular nominal orbit, one of the ideas developed in this thesis work was to use the Hill-Clohessy-Wiltshire equations to describe the relative motion of each spacecraft with respect to its nominal position on the orbit.
The spacecraft dynamics in a neighborhood of the target is described by the following equations:

$$
\begin{aligned}
\ddot{z}_1 &= 3\omega_{nom}^2 z_1 + 2\omega_{nom}\dot{z}_2 + u_1\\
\ddot{z}_2 &= -2\omega_{nom}\dot{z}_1 + u_2\\
\ddot{z}_3 &= -\omega_{nom}^2 z_3 + u_3
\end{aligned}
\tag{4.6}
$$

where ω_{nom} is the nominal angular velocity of the target point on the nominal orbit and u_1, u_2, u_3 are the accelerations produced by the command input along the three directions of motion.

The Hill-Clohessy-Wiltshire frame, illustrated in Figure 4.2 is centered in the target point and have the z_1-axis along the radius vector of the target point, the z_3-axis along its angular momentum vector, and the z_2-axis which completes the right handed system.

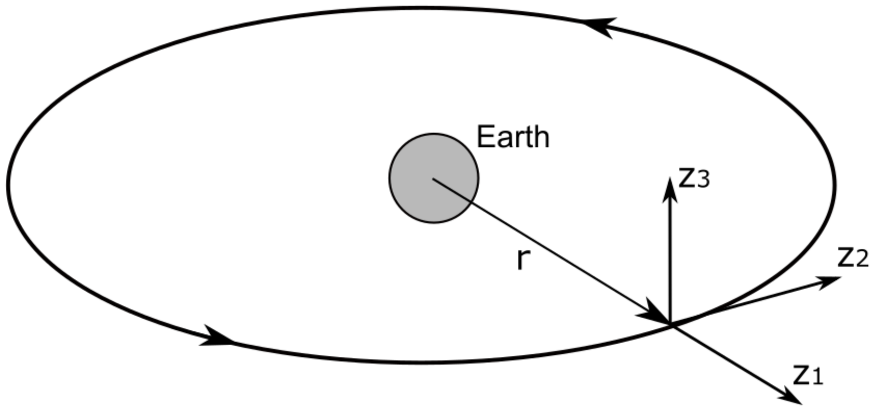

Figure 4.2: Hill-Clohessy-Wiltshire Frame of Reference

Therefore, we define with z_i the spacecraft coordinates in the target-centered frame of reference.
The model equations previously defined can be rewritten in matricial form by means of the following LTI system:

$$\begin{aligned} \dot{\boldsymbol{x}} &= A\boldsymbol{x} + B\boldsymbol{u} \\ \boldsymbol{y} &= C\boldsymbol{x} + D\boldsymbol{u} \end{aligned} \tag{4.7}$$

where:

$$\boldsymbol{x} = \begin{bmatrix} z_1 \\ z_2 \\ z_3 \\ \dot{z_1} \\ \dot{z_2} \\ \dot{z_3} \end{bmatrix}, A = \begin{bmatrix} 0 & 0 & 0 & 1 & 0 & 0 \\ 0 & 0 & 0 & 0 & 1 & 0 \\ 0 & 0 & 0 & 0 & 0 & 1 \\ 3\omega_{nom}^2 & 0 & 0 & 0 & 2\omega_{nom} & 0 \\ 0 & 0 & 0 & -2\omega_{nom} & 0 & 0 \\ 0 & 0 & -\omega_{nom}^2 & 0 & 0 & 0 \end{bmatrix}, B = \begin{bmatrix} 0 \\ I \end{bmatrix}, C = I, D = 0,$$

4.3 Integrated Orbit and Formation Model

Besides the HCW equations, the other model taken in consideration, for the internal dynamics of the above-mentioned model-based techniques, makes use of a novel set of Hill-type equations, initially developed for the EMC strategy currently adopted. This model, called Integrated Formation Control (IFC), allows a common description of the formation altitude and inter-satellite distance, basing its dynamics on the definition of the FLOF.
The model formulation assumes that the high-frequency acceleration components are only due to the gravity term δg_k, where $k = 1{,}2$ is a pedix used to denote which satellite is considered. This assumption is realistic if the short-term non gravitational accelerations

are cancelled, or in other words if a drag-free control is available [10].
The formation dynamics is derived with respect to the FLOF frame and requires the definition of the orbit and formation perturbations. In this context, let us consider the GNSS measurements $\mathbf{y}_{rk}$ and $\mathbf{y}_{vk}$ of the spacecrafts' CoMs position and velocity vectors, and the measurements $\mathbf{y}_{ak}$ coming from accelerometers. Thus, for each satellite, the following relations hold:

$$\begin{aligned}
&\ddot{\mathbf{r}}_k(t) = -\mathbf{g}(\mathbf{r_k}) + \mathbf{a}_k(t) \qquad \mathbf{r}_k(0) = \mathbf{r}_{k0} \qquad \dot{\mathbf{r}}_k(0) = \mathbf{v}_{k0}\\
&\mathbf{y}_{rk}(t) = \mathbf{r}_k(t) + \mathbf{e}_{rk}(t)\\
&\mathbf{y}_{vk}(t) = \dot{\mathbf{r}}_k(t) + \mathbf{e}_{vk}(t)\\
&\mathbf{y}_{ak}(t) = \mathbf{P}_a(\mathbf{a}_k + \mathbf{n}_{ak}) + \mathbf{w}_{ak}
\end{aligned} \tag{4.8}$$

where $\mathbf{e}_{rk}$ and $\mathbf{e}_{vk}$ are the model errors which include both measurement errors and neglected dynamics, $\mathbf{P}_a$ is the accelerometer dynamics, while $\mathbf{n}_{ak}$ and $\mathbf{w}_{ak}$ are the low-frequency and the high-frequency accelerometer errors. Further, by denoting with m the spacecraft mass and respectively with $\mathbf{d}_k$ and $\mathbf{u}_k$ the disturbance forces and the thruster command forces, the term $\mathbf{a}_k = (\mathbf{u}_k + \mathbf{d}_k)/m$ accounts for the non-gravitational accelerations acting upon the k-th spacecraft.
Moving our attention from the single satellites to the overall formation, let's denote the mean and differential formation non-gravitational accelerations as:

$$\mathbf{a} = \frac{\mathbf{a}_1 + \mathbf{a}_2}{2}, \qquad \Delta\mathbf{a} = \mathbf{a}_1 - \mathbf{a}_2. \tag{4.9}$$

Now, with the same logic used before, it is possible the write the following relations for the formation mean and differential dynamics:

$$\begin{aligned}
\ddot{\mathbf{r}}_k(t) &= -\frac{\mathbf{g}(\mathbf{r_1}) + \mathbf{g}(\mathbf{r_2})}{2} + \mathbf{a}(t) = -\mathbf{g}(\mathbf{r}) + \mathbf{a}(t), \quad \mathbf{r}(0) = \mathbf{r}_0, \quad \dot{\mathbf{r}}(0) = \mathbf{v}_0\\
\Delta\ddot{\mathbf{r}}(t) &= -(\mathbf{g}(\mathbf{r}_1) - \mathbf{g}(\mathbf{r}_2)) + \Delta\mathbf{a}(t)\\
&= -U(\mathbf{r})\Delta\mathbf{r}(t) + \Delta\mathbf{a}(t) \quad \Delta\mathbf{r}(0) = \Delta\mathbf{r}_0, \quad \Delta\dot{\mathbf{r}}(0) = \Delta\mathbf{v}_0
\end{aligned} \tag{4.10}$$

where $U(\mathbf{r})$ is the gravity tensor to be measured for obtaining the value of the local gravity field.
Let's recall that the objective of the drag-free control is to reach the condition:

$$\mathbf{a}_k = 0 \quad \Longrightarrow \quad \mathbf{a} = 0, \quad \Delta\mathbf{a} = 0 \tag{4.11}$$

This condition is obtained with a drag-free command $\mathbf{u}_k$ able to cancel the real-time prediction $\hat{\mathbf{d}}_k$ of the disturbance forces coming from accelerometer wide-band measurements. Nevertheless, because of the limited BW of the drag-free control law, measurement errors and causality, this cancellation cannot be perfect and produces always a residual drag-free acceleration $\mathbf{w}_{ak}$

$$\mathbf{u}_k = -\hat{\mathbf{d}}_k \quad \Longrightarrow \quad \mathbf{a}_k = (-\mathbf{d}_k + \hat{\mathbf{d}}_k)/m \simeq \mathbf{w}_{ak} \neq 0. \tag{4.12}$$

As previously said, to build the integrated formation model, the preliminary definition of formation and orbit perturbations is needed.
At this purpose, let's consider a nominal reference sphere of radius $\mathbf{r}_{nom}$, that stands for the nominal formation altitude, and the nominal inter-satellite distance d_{nom}, whose direction is set as tangent to the reference sphere. These quantities are associated respectively to the formation CoM position $\mathbf{r}$ on the orbit and the satellites' relative positions $\Delta\mathbf{r}$. Denoting with $\mathbf{r}_1$ and $\mathbf{r}_2$ the satellites' radii, the following relations hold:

$$\begin{aligned} &\mathbf{r} = r_x\vec{o}_1 + r_z\vec{o}_3, \quad \mathbf{r}_1 - \mathbf{r}_2 = d_{nom}\vec{o}_1 \\ &\mathbf{r}_1 = (r_x + \frac{d}{2})\vec{o}_1 + r_z\vec{o}_3, \quad \mathbf{r}_2 = (r_x - \frac{d}{2})\vec{o}_1 + r_z\vec{o}_3 \end{aligned} \tag{4.13}$$

where, d is the inter-distance, r_z is the height of the triangular virtual structure and r_x is the radius component along the satellite-to-satellite direction $\vec{o}_1$.
One of the objectives of Orbit and Formation Control is to align the formation radius $\mathbf{r}$ to $\vec{o}_3$, bringing r_x to its nominal condition, i.e. $r_x = 0$. Consequently, the three Cartesian perturbations in FLOF coordinates are $\delta d, \delta r_x, \delta r_z$, which can be introduced in the formulation of formation mean and differential radius as follows:

$$\begin{aligned} &\Delta\mathbf{r} = (d_{nom} + \delta d)\vec{o}_1, \\ &\mathbf{r} = r_x\vec{o}_1 + r_z\vec{o}_3 = (0 + \delta r_x)\vec{o}_1 + (r_{nom} + \delta r_z)\vec{o}_3 \end{aligned} \tag{4.14}$$

Furthermore, three additional perturbations are provided by the 3D non-zero components of the FLOF angular rate vector $\boldsymbol{\omega} = \omega_x\vec{o}_1 + \omega_y\vec{o}_2 + \omega_z\vec{o}_3$, whose norm is defined by $\omega = \omega_{nom} + \delta\omega$. According to what has been said so far, the overall formation dynamics can be described by 6 DoFs.
It is worth to notice that since the three Cartesian coordinates are defined considering a reference sphere of radius r_{nom}, they perfectly fit the in-line formation type, characterized by a circular orbit. Conversely, the reference orbit described by the pendulum formation has an elliptical shape. Nonetheless, it can be proved that this elliptical orbit can be approximated by the same circular polar orbit of the in-line case and so the discrepancy can be neglected, thus making the three Cartesian perturbations valid in both cases [10].
The formation dynamics above defined is a necessary starting point for the derivation of the continuous-time equations of the IFC model. Since, as previously specified, the orbit and formation dynamics is based on 6 DoFs, the IFC model will involve six differential equations. The first set of differential equations is obtained starting from the relative position vector $\Delta\mathbf{r}$, while the second set of differential equations comes from the kinematic equation of the mean formation radius $\mathbf{r}$. Thus, the final perturbation equations are obtained by combining the kinematics equations involving the six selected perturbations with the formation triangle dynamic equations.

As a result of this combination, the six scalar second order differential equations are:

$$
\begin{aligned}
&\ddot{d} = -\omega_s^2(r)d(1-3\frac{r_x^2}{r^2}) + d(\omega_y^2+\omega_z^2) + \Delta a_x \\
&\dot{\omega}_z = -2\dot{d}\frac{\omega_z}{d} - \omega_y\omega_x + \frac{\Delta a_y}{d} \\
&\dot{\omega}_y = -3\omega_0^2(r)\frac{r_x r_z}{r^2} - \frac{2}{d}\dot{d}\omega_y + \omega_z\omega_x - \frac{\Delta a_z}{d} \\
&\ddot{r}_x = -\omega_s^2(r)r_x(1-3\frac{r_z^2}{r^2}) - 2\omega_y\dot{r}_z + (\omega_y^2+\omega_z^2)r_x - 2\omega_z\omega_x r_z + 2\frac{r_z}{d}\omega_y\dot{d} + \frac{r_z}{d}\Delta a_z + a_x \\
&\ddot{r}_z = -\omega_s^2(r)r_z(1-3\frac{r_x^2}{r^2}) + 2\omega_y\dot{r}_x + (\omega_x^2+\omega_y^2)r_z - 2\frac{r_x}{d}\omega_y\dot{d} - \frac{r_x}{d}\Delta a_z + a_z \\
&\dot{\omega}_x = \frac{2}{r_z}(-\omega_x\dot{r}_z + \omega_z\dot{r}_x) + \omega_z\omega_y - 2\frac{r_x}{dr_z}\omega_z\dot{d} + \frac{r_x}{dr_z}\Delta a_y - \frac{a_y}{r_z}
\end{aligned}
\tag{4.15}
$$

where $\omega_s^2 = \frac{\mu}{r^3}$ is the mean orbital rate.
As we can notice from Eq. 4.15, the FLOF components of the external mean and differential accelerations (respectively $\mathbf{a}$ and $\Delta\mathbf{a}$) have been highlighted. Moreover, it is worth to underline that, for the derivation of this model, the gravity gradient $\Delta\mathbf{g}$ and the gravity term $\mathbf{g}$ have been expressed in FLOF coordinates considering only the spherical gravity term and ideally arranging the higher order terms, from J2 on, as part of the external acceleration contribution.
Finally, the obtained perturbation equations need to be linearised around the equilibrium point. As a matter of fact, since the aim of formation control is to keep the formation variables above defined close to their nominal value, an equilibrium point must be identified. To do this, under zero input signals, let's set each formation variable derivative to zero, obtaining in this way the following equilibrium components:

$$
\begin{aligned}
&d_{eq} = d_{nom} \\
&r_{z,eq} = r_{nom} \\
&r_{x,eq} = 0 \\
&\omega_{y,eq} = \omega_s(r_{nom}) = \omega_{nom} \\
&\omega_{x,eq} = \omega_{z,eq} = 0
\end{aligned}
\tag{4.16}
$$

Now, let's define the formation triangle perturbed states as the difference between the actual and the nominal value and let's explicit the non-gravitational acceleration input vector as follows:

$$\delta \boldsymbol{x}_f = \begin{bmatrix} \delta d = d - d_{nom} \\ \rho_x = \alpha r_x \\ \rho_z = \alpha(r_z - r_{nom}) \end{bmatrix}, \quad \delta \boldsymbol{v}_f = \begin{bmatrix} \delta \dot{d}/\omega_{nom} \\ \dot{\rho}_x/\omega_{nom} \\ \delta \dot{\rho}_z/\omega_{nom} \\ w_x = \alpha \dot{r}_x/\omega_{nom} \\ w_y = d_{nom}(\omega_y - \omega_{nom})/\omega_{nom} \\ w_z = \alpha \dot{r}_z/\omega_{nom} \end{bmatrix},$$
$$\boldsymbol{a}_f = \begin{bmatrix} \Delta a_x \\ \Delta a_y \\ \Delta a_z \\ \alpha a_x \\ \alpha a_y \\ \alpha a_z \end{bmatrix} \tag{4.17}$$

From Eq. 4.17, we can notice that the perturbed state vector $\delta \boldsymbol{x}$ is composed by two sub-vectors $\delta \boldsymbol{x}_f$ and $\delta \boldsymbol{v}_f$, that respectively represent the length and the rate state variables. The adimensional factor $\alpha = d_{nom}/r_{nom}$ has been used in order to express all the quantities in length unit. It is worth to underline that the model simplification introduced by considering only the spherical gravity term could influence the model capability to describe the formation dynamic behaviour when the adimensional coefficient $\alpha = d_{nom}/r_{nom}$ is greater than 0.01. In this case, J2 gravity term contribution to the gravity gradient should be taken in consideration.
The model equations above defined can be rewritten in equilibrium conditions through the perturbed state variables and inputs, leading to the following linear time-invariant (LTI) continuous-time system:

$$\begin{aligned} \begin{bmatrix} \delta \dot{\boldsymbol{x}}_f \\ \delta \dot{\boldsymbol{v}}_f \end{bmatrix}(t) &= \omega_{nom} \begin{bmatrix} 0 & A_{12} \\ A_{21} & A_{22} \end{bmatrix} \begin{bmatrix} \delta \boldsymbol{x}_f \\ \delta \boldsymbol{v}_f \end{bmatrix}(t) = \frac{1}{\omega_{nom}} \begin{bmatrix} 0 \\ B_2 \end{bmatrix} \boldsymbol{a}_f(t) \\ \boldsymbol{y}_f(t) &= \begin{bmatrix} C_1 & C_2 \end{bmatrix} \begin{bmatrix} \delta \boldsymbol{x}_f \\ \delta \boldsymbol{v}_f \end{bmatrix}(t) \end{aligned} \tag{4.18}$$

where the matrices A_{12}, A_{21}, A_{22} and B_2 are parameter free.
Note that, the matrix A is ninth order and its eigenvalues are

$$\lambda_{1,2,3} = 0, \qquad \lambda_{4,5,6} = j\omega_{nom}, \qquad \lambda_{7,8,9} = -j\omega_{nom}$$

Hence, the three eigenvalues $\lambda_{1,2,3} = 0$ need to be stabilized, while the others are imposed by nature.
From the complete model defined in Eq. 4.18, it is possible to consider a restricted seventh order one, which is proven to be observable and controllable when assuming $\boldsymbol{y}_f(t) = \delta \boldsymbol{x}_f(t)$. Such model considers only the three Cartesian perturbations ρ_x, ρ_z, δd and their normalized rates w_x, w_z, w_d, plus the normalized perturbation of the orbital rate w_y. In addition, also the input is restricted to the in-plane input variables in $\boldsymbol{a}_f$. These last modifications lead to the following 7-th order LTI system:

$$\begin{aligned}\begin{bmatrix}\dot{\boldsymbol{r}}\\ \dot{\boldsymbol{w}}\end{bmatrix}(t) &= \begin{bmatrix}0 & I\omega_{nom}\\ A_{21} & A_{22}\end{bmatrix}\begin{bmatrix}\boldsymbol{r}\\ \boldsymbol{w}\end{bmatrix}(t) = \begin{bmatrix}0\\ B_2\end{bmatrix}\boldsymbol{u}(t)\\ \boldsymbol{y}(t) &= \begin{bmatrix}I & 0\end{bmatrix}\begin{bmatrix}\boldsymbol{r}\\ \boldsymbol{w}\end{bmatrix}(t), \qquad \begin{bmatrix}\boldsymbol{r}\\ \boldsymbol{w}\end{bmatrix}(0) = \begin{bmatrix}\boldsymbol{r}_0\\ \boldsymbol{w}_0\end{bmatrix}\end{aligned} \tag{4.19}$$

where:

$$\begin{aligned}&\boldsymbol{r} = \begin{bmatrix}\rho_x = \alpha\delta r_x\\ \rho_z = \alpha\delta r_z\\ \delta d\end{bmatrix}, \boldsymbol{w} = \begin{bmatrix}w_x = \alpha\dot{r}_x/\omega_{nom}\\ w_z = \alpha\dot{r}_z/\omega_{nom}\\ w_d = \dot{d}/\omega_{nom}\\ w_y = d_{nom}(\omega_y - \omega_{nom})/\omega_{nom}\end{bmatrix},\\ &\boldsymbol{u} = \begin{bmatrix}u_{fx}\\ u_{fz}\\ \Delta u_{fx}\\ \Delta u_{fz}\end{bmatrix} = \begin{bmatrix}\alpha a_x\\ \alpha a_z\\ \Delta a_x\\ \Delta a_z\end{bmatrix}\\ &A_{21} = 3\omega_{nom}\begin{bmatrix}1 & 0 & 0\\ 0 & 1 & 0\\ 0 & 1 & 0\\ -1 & 0 & 0\end{bmatrix}, \; A_{22} = 2\omega_{nom}\begin{bmatrix}0 & -1 & 1 & 0\\ 1 & 0 & 0 & 1\\ 0 & 0 & 0 & 1\\ 0 & 0 & -1 & 0\end{bmatrix},\\ &B_2 = \begin{bmatrix}\alpha & 0 & 0 & 1\\ 0 & \alpha & 0 & 0\\ 0 & 0 & 1 & 0\\ 0 & 0 & 0 & -1\end{bmatrix}/\omega_{nom}\end{aligned} \tag{4.20}$$

4.4 Nonlinear Model vs Hill-Clohessy-Wiltshire Equations

The first necessary step to be sure that the Hill-Clohessy-Wiltshire equations can represent in a good way the dynamics of our system is to compare the free-evolution of its state variables with the evolution of the corresponding ones obtained from the nonlinear model. In order to put the two models in the same conditions, the simulation with the nonlinear model must be performed after having zeroed the external disturbance forces caused by atmospheric drag and solar pressure, and after having modified the gravity model in order to consider only the spherical term. In addition, since it is necessary to start from the same initial conditions in both cases, a frame transformation of the initial satellites' position and velocity vectors from the inertial frame to the HCW frame is needed.
Recalling that HCW equations are based on the assumption of using a circular target orbit, let's consider as target an Earth-centered orbit of radius $r_{nom} = (RE + h)(1 - e)$, where $RE = 6.3781 \times 10^6\ m$ is the Earth equatorial radius, $h = 3.453 \times 10^5\ m$ is the nominal formation altitude and $e = 10^{-3}$ is the eccentricity value used in the nonlinear simulator. Moreover, since we are assuming a circular orbit, the nominal angular velocity can be computed as $\omega_{nom} = \sqrt{\mu/r_{nom}^3} = 0.0011\ rad/s$.

To identify the satellites' nominal initial position and velocity vectors in the inertial frame, we need firstly to transform the position and velocity vectors on the equatorial plane written in the Eq. 4.21, by means of the matrix T defined in the Eq. 4.22.

$$\boldsymbol{r} = \begin{bmatrix} r_{nom} \\ 0 \\ 0 \end{bmatrix}, \boldsymbol{v} = \begin{bmatrix} 0 \\ v_{nom} = \sqrt{\frac{\mu}{r_{nom}}} \\ 0 \end{bmatrix} \tag{4.21}$$

$$T = R_3(\Omega)R_1(i)R_3(\omega) \tag{4.22}$$

where:

$$R_3(\Omega) = \begin{bmatrix} \cos\Omega & -\sin\Omega & 0 \\ \sin\Omega & \cos\Omega & 0 \\ 0 & 0 & 1 \end{bmatrix}, R_1(i) = \begin{bmatrix} 1 & 0 & 0 \\ 0 & \cos i & -\sin i \\ 0 & \sin i & \cos i \end{bmatrix}, R_3(\omega) = \begin{bmatrix} \cos\omega & -\sin\omega & 0 \\ \sin\omega & \cos\omega & 0 \\ 0 & 0 & 1 \end{bmatrix}$$

The transformation matrix T is composed by three rotations: the first is about the z axis of an angle $\Omega = 0\ rad$, the second is about the x axis of an angle $i = 1.1519\ rad$ and the third is about the z axis of an angle $\omega = 0.0074\ rad$ for the nominal position of Satellite 1 and of an angle $\omega = -0.0074\ rad$ for the nominal position of Satellite 2. Let's recall that Ω, i and ω represent respectively the Right Ascension of the Ascending Node (RAAN), the orbit inclination and the argument of perigee. The above mentioned values of RAAN and inclination are the same used for the nonlinear simulator, while the values of the two arguments have been computed in order to guarantee a distance between the satellites equal to the nominal value $d_{nom} = 100\ km$.
Finally, the initial conditions of the two satellites in the HCW frame are computed by the difference between the satellites' initial position and velocity vectors in the inertial frame given by the nonlinear simulator, and their nominal values obtained by means of the previous transformation, as illustrated in Figure 4.3.

$$\begin{aligned} \boldsymbol{r_{hcw0}} &= \boldsymbol{r_0} - \boldsymbol{r_{nom0}} \\ \boldsymbol{v_{hcw0}} &= \boldsymbol{v_0} - \boldsymbol{v_{nom0}} \end{aligned} \tag{4.23}$$

Thus, the initial conditions of the two satellites in the HCW frame, obtained from Eq. 4.23, are respectively:

$$\boldsymbol{x}_{01} = \begin{bmatrix} -5.388 \times 10^{-5} \\ 26.904 \\ 1.4850\times^{-12} \\ -0.0309 \\ 3.8508 \\ -2.5557 \times 10^{-13} \end{bmatrix}, \qquad \boldsymbol{x}_{02} = \begin{bmatrix} -5.388 \times 10^{-5} \\ -26.904 \\ -1.4850\times^{-12} \\ 0.0309 \\ 3.8508 \\ -2.5557 \times 10^{-13} \end{bmatrix} \tag{4.24}$$

The six elements of each vector represent the state variables of the HCW system, namely the components of position and velocity vectors expressed in the HCW frame.
In Figures 4.4 and 4.5 are compared the position and velocity inertial components obtained

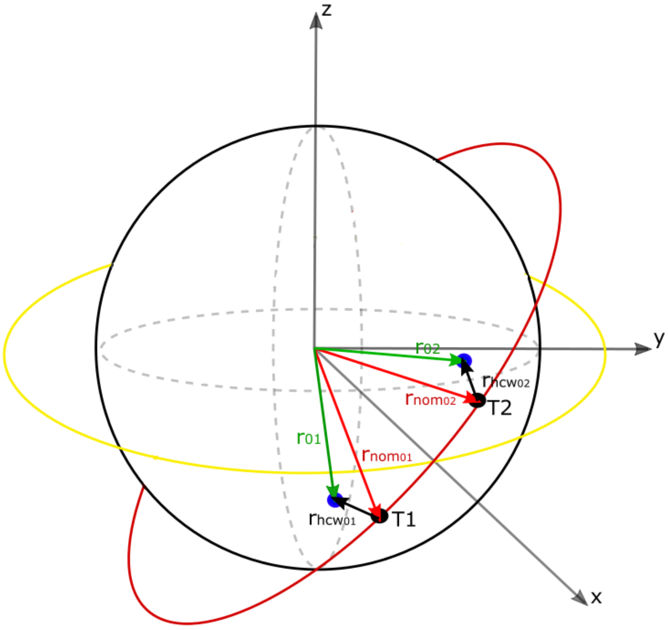

Figure 4.3: Tranformation from Inertial to HCW Frame

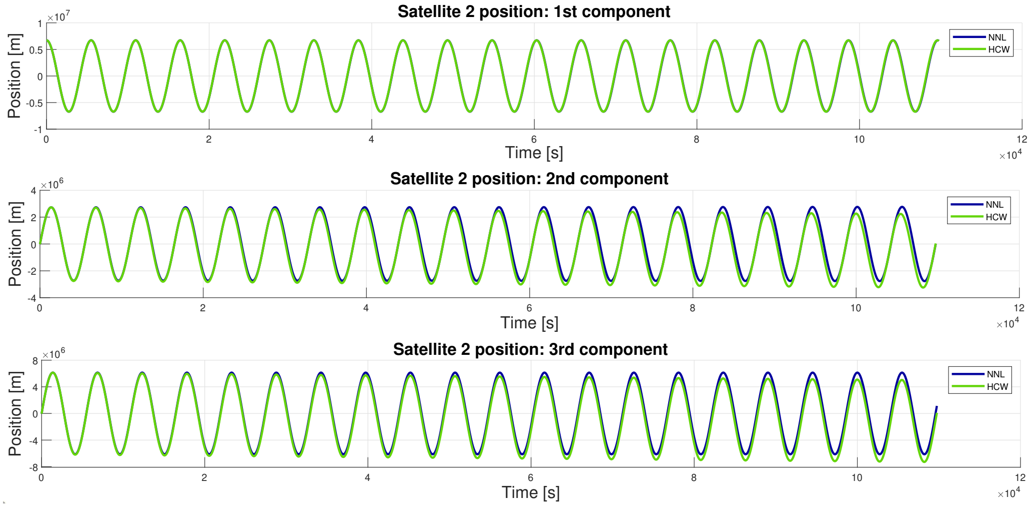

Figure 4.4: Comparison between HCW Model and Nonlinear Model (Position Components)

from the HCW system with the corresponding variables obtained from the nonlinear model. For simplicity only the Satellite 2 variables have been reported in this pictures, but the same considerations hold also for Satellite 1. As we can notice, this comparison shows a faster divergence of the HCW position components with respect to the corresponding nonlinear ones. This may imply an inadequacy of the Hill-Clhoessy-Wiltshire equations in describing the NGGM system due to the fact that these equations lead to a very approximated model where a lot of effects are completely disregarded.

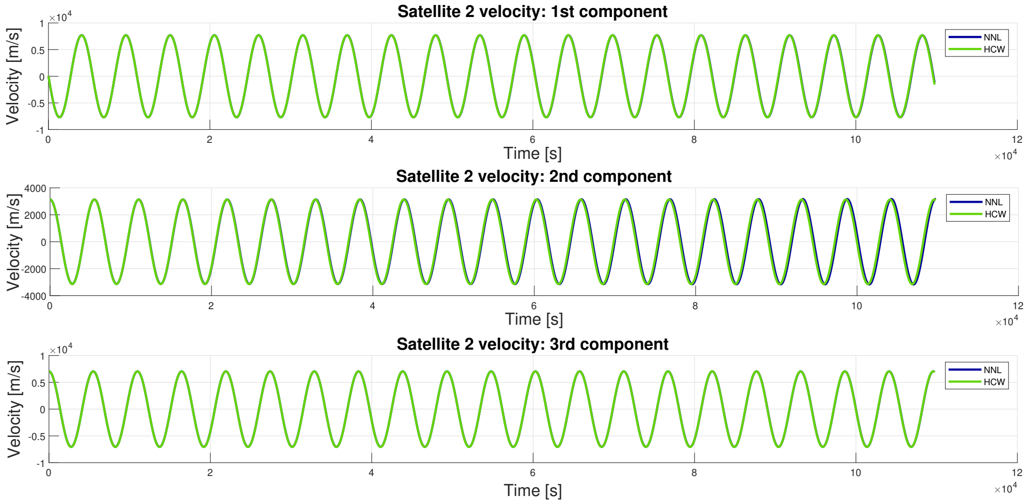

Figure 4.5: Comparison between HCW Model and Nonlinear Model (Velocity Components)

4.5 Nonlinear Model vs IFC Model

Since the comparison between Nonlinear model and HCW equations has made it clear that the Hill-Clohessy-Wiltshire model does not fit particularly well this kind of control problem, let's now focus on the Integrated Orbit and Formation model, explained in detail from a theoretical point of view in Section 4.3. Even in this case, the first necessary step is the comparison between the free-evolution of the formation state variables with the evolution of the corresponding variables obtained from the nonlinear model. In this case, in order to put the two models in the same conditions, besides zeroing the external disturbance forces, we need also to modify the gravity model of the nonlinear simulator in order to consider only the spherical term. This modification is needed because in the formulation of the IFC model only the spherical gravity term has been taken into account, ideally treating all the higher order terms as part of the external acceleration components. In addition, since it is necessary to start from the same initial conditions, using the initial FLOF position and velocity vectors given by the nonlinear simulator, it is possible to derive the following initial conditions for the IFC model:

$$\boldsymbol{x}_0 = \begin{bmatrix} 0 \\ -102.77 \\ 53.81 \\ -1.18 \times 10^{-11} \\ 0 \\ 0 \\ 200.25 \end{bmatrix} \tag{4.25}$$

Notice that the values of r_{nom}, d_{nom} and ω_{nom} that have been used to find these initial conditions, are those corresponding to the values specified in the nonlinear simulator, i.e. $r_{nom} = (RE + h)$, $d_{nom} = 100\ km$ and $\omega_{nom} = 0.001145201778066$ rad/s.
In Figure 4.6 the output variables obtained from the IFC model are compared with the

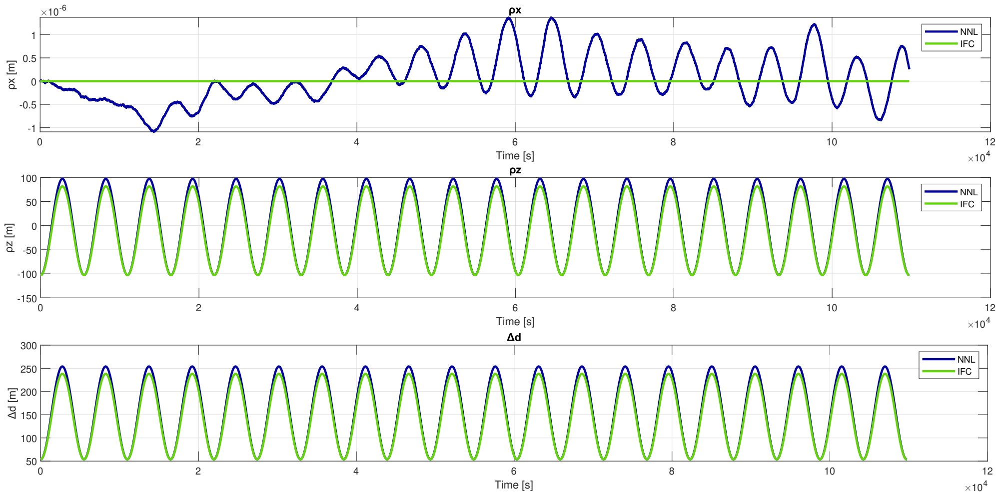

Figure 4.6: Comparison between IFC Model and Nonlinear Model

corresponding variables given by the Nonlinear model. Specifically, only the first three state ρ_x, ρ_z, Δd have been considered since they are the perturbed states needed for the verification of the triangular virtual structure stability. As we can notice, the behaviour of the 2nd and 3rd state variables, namely ρ_z and Δd, is very similar in both cases, with a discrepancy of only few tens of meters. The 1st state ρ_x, instead, shows a more significant divergence since the values have different order of magnitude. However, as shown in more detail in Figure 4.7, the values of ρ_x are in both cases very close to zero (10^{-6} for the Nonlinear model and 10^{-11} for the IFC model), thus this difference is not particularly worrying.

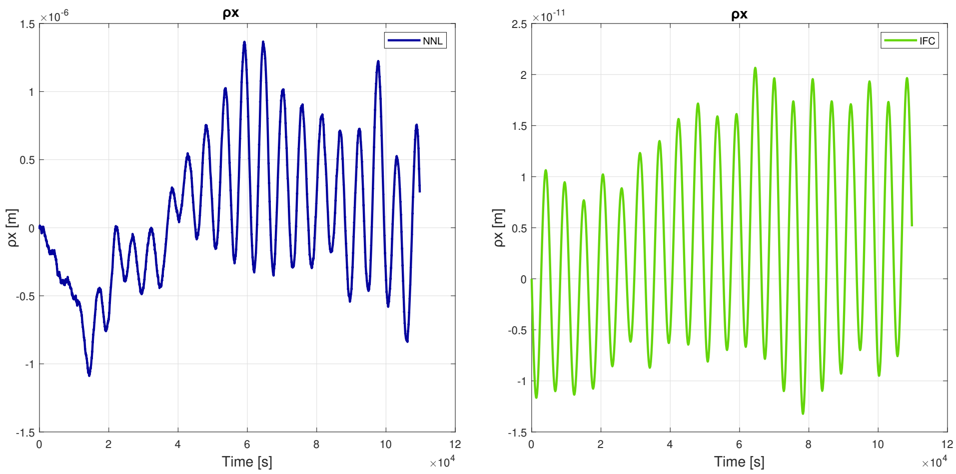

Figure 4.7: Comparison between IFC Model and Nonlinear Model: ρ_x

4.6 HCW Model vs IFC Model

In the previous sections, the theoretical description of both the HCW equations and the IFC model has been presented. For both cases we stressed the attention on the comparison between the free evolution of each model's state variables and the corresponding variables of the real plant, represented here by the high-fidelity nonlinear model, described in Chapter 3. From the comparisons performed by placing the two models in the same initial conditions and using the same order of gravity, the Figures 4.4, 4.5 and 4.6 have been obtained. Looking at the first two pictures, namely those referred to the comparison between HCW model and Nonlinear model, it has been emphasized how the plot referred to the position components showed a faster divergence with respect to the one referred to the velocity components. Indeed, as it is evident reading on the y-axis, the order of magnitude of these components is quite big, so even if on a cursory glance, the difference seems minimal, in reality there is a considerable disparity between the compared quantities.
Looking, instead, at the last figure, that is the one concerning the comparison between IFC model and Nonlinear model, it is possible to observe a difference of only few tens of meters between the two models. However, to be able to make sure to the greater capability of the IFC model in describing our system dynamics, it is convenient to compare the same quantities. Thus, since the Formation Control focuses on the satellite-to-satellite distance, let's plot in Figure 4.8 the comparison between HCW model and Nonlinear Model stressing the attention on the quantity $\Delta d = d - d_{nom}$.

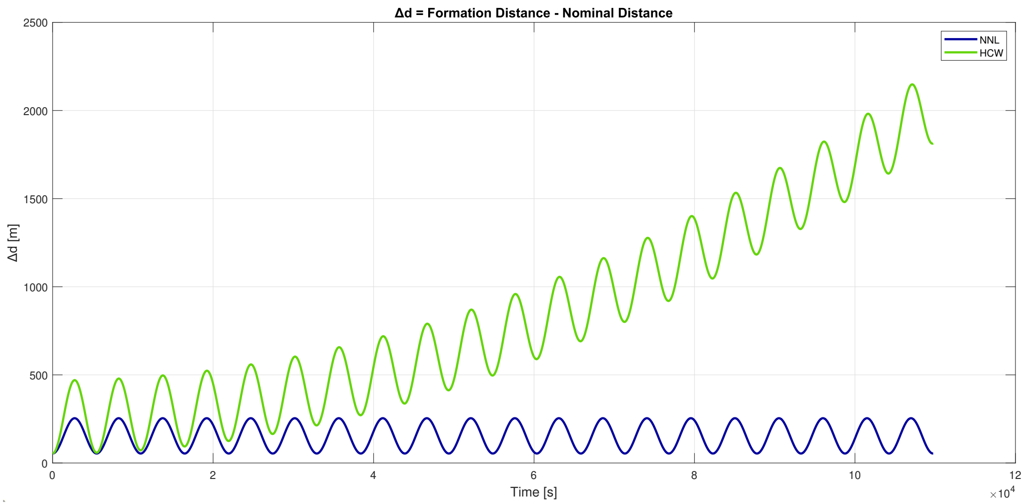

Figure 4.8: Comparison between HCW Model and Nonlinear Model: Δd

From this figure, it is evident that this quantity diverges much faster in HCW model than in the Nonlinear one, where, on the contrary, it remains almost flat.
Finally, for the sake of completeness, it is worth to compare this plot with the one reported in the third row of Figure 4.6, in which the same quantity Δd is shown in the comparison between IFC model and Nonlinear model. Analyzing the two plots, it becomes clear how the IFC model is certainly more effective in approximating the real plant dynamics as it shows a behavior much more similar to the nonlinear one.

4.7 NMPC framework for Formation Control

From the previous section, it has been clarified that the most suitable model to be used for the internal control dynamics is the Integrated Formation Control (IFC) model. Consequently, from now on, in the development of the NMPC framework for this specific control problem, the internal prediction will always rely on this linearized model, which is the one that, despite its simplifications, best approximates the real plant dynamics.
Before introducing the implementation of the Formation Control block diagram via NMPC strategy, it is worth to recap some general features to be taken into account. First of all, let's recall from Section 1.4 that the overall NGGM control unit is organized in a hierarchical way, with two nested loops constituted by a wide-band Drag-Free Control and a narrow-band Orbit and Formation Control. As consequence, to be sure that drag-free control does not influence the formation authority, the orbit and formation control should be designed as ideally low-frequency with respect to the the other one. Therefore, its sampling time T_s should be bigger than the one used for drag-free control, i.e. bigger than 1 s. Then, the prediction horizon needs to be chosen with a trial and error procedure considering that generally a large T_p increases the closed-loop stability properties but a "too large" T_p may reduce the short time tracking accuracy.
Further, it is worth to underline that the problem under study is also constrained by strong requirements on the command input, which should remain very limited in order to guarantee a very low thruster authority. Moreover, another constraint to be included in the optimization problem concerns the requirement on the formation distance, whose variation should stay within a limit of the 10% from the nominal value, that means it should stay between 90 km and 110 km, as specified in Table 4.1. Thanks to the NMPC framework, it is possible to manage all these constraints on state and input directly by setting upper and lower bounds on the control command and by using a constraint on the 3rd state of the IFC model, namely $\Delta d = d - d_{nom}$, so as to limit its variation to a maximum of 10 km.

4.7.1 NMPC with Ideal Plant

To develop an NMPC framework for the specific control problem under study we proceeded step by step considering first of all an ideal situation where the plant is identical to the internal prediction model, namely the IFC model, whose LTI system formulation is reported in Eq. 4.19. As already explained, this system is proven to be observable and controllable when $C = \begin{bmatrix} I & 0 \end{bmatrix}$, that means when the output coincides with the first three perturbed states ρ_x, ρ_z, and Δd. The ideal plant, in this case, has been formulated using the same IFC system equations, with the only difference in the matrix C, that has been chosen equal to the identity matrix ($C = I_{7\times 7}$) in order to give as output all the seven states needed for the control algorithm.
The state constraint introduced at this step regards the third state Δd, that is the one that we want to maintain inside the limit specified by the scientific requirements. At this purpose a state constraint $X_c = \{x : \|\Delta_d\| \leq 10000\}$ has been introduced. For what concerns the input constraints, instead, we proceeded firstly choosing them as large as possible, and then progressively reducing their order of magnitude until reaching the limit after which the system stability was no longer guaranteed. Figure 4.9 depicts the Simulink

scheme adopted in the development of an NMPC framework in ideal conditions, that is with the plant ideally equal to the prediction model. Inside the block "NMPC law" is

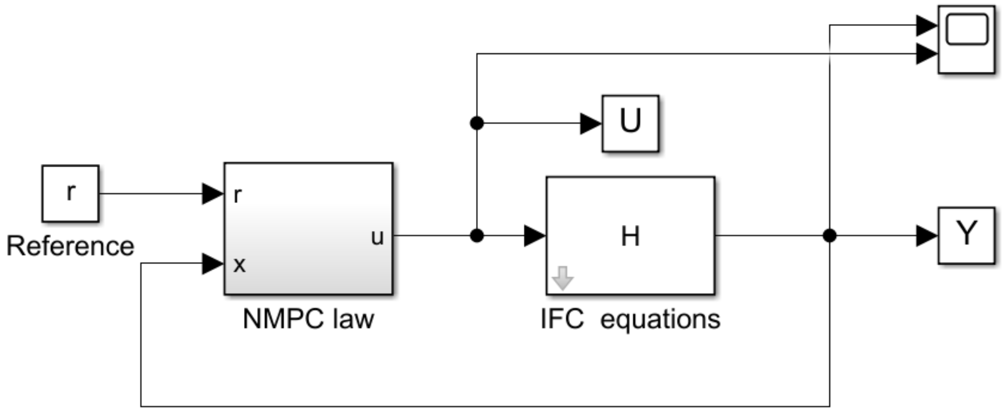

Figure 4.9: NMPC Framework with Ideal Plant

present a structure which defines the IFC internal prediction model, the state and input constraints and all the other parameters which characterize the NMPC framework, such as the sampling time, the prediction horizon, the weight matrices and so forth. The block "IFC equations", instead, represent the plant, that in this case exploits the same system equations of the IFC model. The seven states exiting from the plant are feedbacked inside the NMPC law, which takes as input also the reference to be tracked, and return as output the optimal command obtained from the solution of the the specified optimization problem. The reference to be tracked in this case is a vector $r = [0; 0; 0]$, since we ideally want the perturbed states goes to zero.

4.7.2 NMPC with Nonlinear Plant

The NMPC configurations, which show a good behaviour with the ideal plant, need to be later inserted inside the nonlinear simulator composed by the system nonlinear model described in Chapter 2, to which the drag-free control block had been added, as explained in detail in Chapter 3. Indeed, the total non-gravitational forces acting on each spacecraft must be given by the resultants of the atmospheric disturbances and the control actions given by the actuators, namely the drag-free and the formation control command forces. However, before summing these two contributions, some transformations are needed. Indeed, looking at Eq. 4.20 we can notice that the input of the IFC model is given the in-plane mean accelerations pre-multiplied by the adimensional factor α and the in-plane differential accelerations, as reported in the following equation:

$$\boldsymbol{u} = \begin{bmatrix} u_{fx} \\ u_{fz} \\ \Delta u_{fx} \\ \Delta u_{fz} \end{bmatrix} = \begin{bmatrix} \alpha a_x \\ \alpha a_z \\ \Delta a_x \\ \Delta a_z \end{bmatrix}. \tag{4.26}$$

In order to sum the same quantities we need to derive from the NMPC command input $\boldsymbol{u}$ the single satellites accelerations $\boldsymbol{a}_1$ and $\boldsymbol{a}_2$. At this purpose, let's recall that

$$\boldsymbol{a} = \frac{\boldsymbol{a}_1 + \boldsymbol{a}_2}{2}, \qquad \Delta\boldsymbol{a} = \boldsymbol{a}_1 - \boldsymbol{a}_2. \tag{4.27}$$

Therefore, merging Eqs. 4.26 and 4.27 it is possible to derive the following system:

$$\begin{cases} u_{fx} = \alpha\frac{a_{1x}+a_{2x}}{2} \\ u_{fz} = \alpha\frac{a_{1z}+a_{2z}}{2} \\ \Delta u_{fx} = a_{1x} - a_{2x} \\ \Delta u_{fz} = a_{1z} - a_{2z}. \end{cases} \tag{4.28}$$

From the solution of the system in Eq. 4.28, the in-plane FLOF coordinates of the satellites' accelerations $\boldsymbol{a_1}$ and $\boldsymbol{a_2}$, can be derived:

$$\begin{cases} a_{1x} = \frac{2u_{fx}+\alpha\Delta u_{fx}}{2\alpha} \\ a_{2x} = \frac{2u_{fx}-\alpha\Delta u_{fx}}{2\alpha} \\ a_{1z} = \frac{2u_{fz}+\alpha\Delta u_{fz}}{2\alpha} \\ a_{2z} = \frac{2u_{fz}-\alpha\Delta u_{fz}}{2\alpha}. \end{cases} \tag{4.29}$$

Consequently, knowing that the out-of-plane coordinates a_{1y} and a_{2y} are equal to zero, we can write the satellites' FLOF acceleration vectors given by thrusters as

$$\begin{aligned} \boldsymbol{a}_1 &= \begin{bmatrix} a_{1x} \\ a_{1y} \\ a_{1z} \end{bmatrix} = \begin{bmatrix} \frac{2u_{fx}+\alpha\Delta u_{fx}}{2\alpha} \\ 0 \\ \frac{2u_{fz}+\alpha\Delta u_{fz}}{2\alpha} \end{bmatrix} \\ \boldsymbol{a}_2 &= \begin{bmatrix} a_{2x} \\ a_{2y} \\ a_{2z} \end{bmatrix} = \begin{bmatrix} \frac{2u_{fx}-\alpha\Delta u_{fx}}{2\alpha} \\ 0 \\ \frac{2u_{fz}-\alpha\Delta u_{fz}}{2\alpha} \end{bmatrix}. \end{aligned} \tag{4.30}$$

Further, since the drag-free command forces are expressed in the spacecraft body reference frame, the single satellites accelerations $\boldsymbol{a}_1$ and $\boldsymbol{a}_2$, need to be multiplied by the spacecraft mass and than two frame transformations have to be performed: the first one from FLOF to Inertial frame and the second one from Inertial to Body frame.

Figure 4.10 depicts the first level of the nonlinear simulator, to which the formation control block has been added. As we can notice, this block takes as input the IFC state variables and the FLOF quaternion to perform the frame transformation mentioned before. The inertial satellites' accelerations $\boldsymbol{a}_1$ and $\boldsymbol{a}_2$ exiting from the formation control block feed the respectively the Satellite 1 and Satellite 2 blocks. Going more into detail, inside the formation control block we can find the NMPC control law and all the transformations needed to derive the satellites' accelerations starting from the NMPC command input, as previously described in Eqs. 4.29 and 4.30. In addition, inside this block is also performed the transformation from FLOF to Inertial frame, as shown in Figure 4.11.

Finally, inside Satellite 1 and Satellite 2 blocks the last transformation from Inertial to Body frame is performed and the acceleration vectors are multiplied by the spacecraft

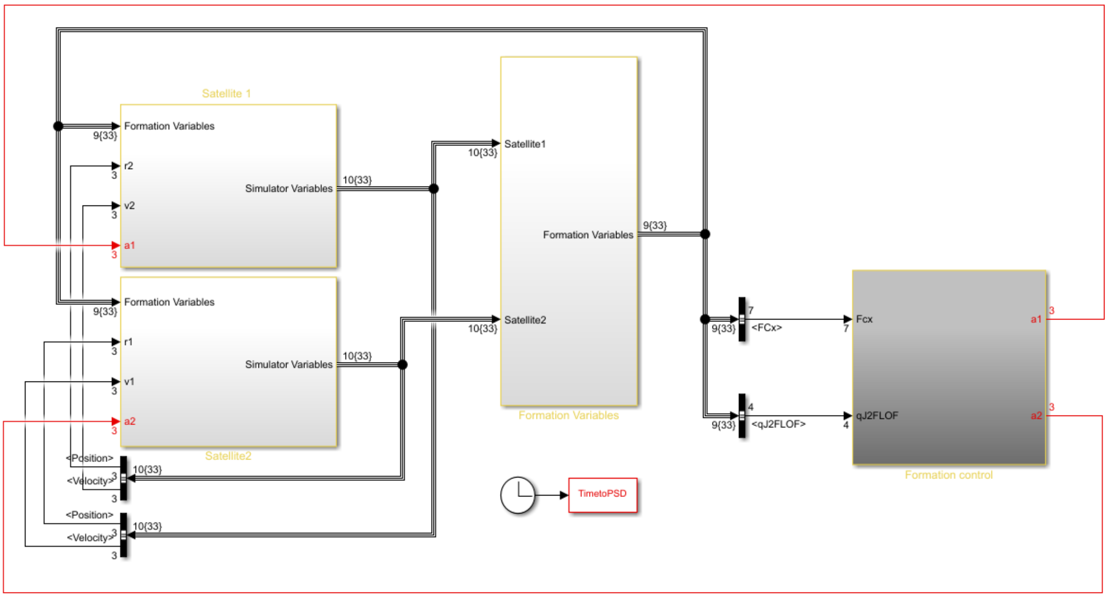

Figure 4.10: Nonlinear Simulator with Formation Control Block

mass in order to obtain the formation control command force that enters in a summing node with the drag-free command force, as represented in Figure 4.12. The quantity exiting from this summing node contributes with the atmospheric disturbances to form the Non-gravitational Body Forces needed for the orbital dynamics.

4.8 Simulated Results

In this section, some results concerning the simulations performed after the introduction of the NMPC-based formation control are presented. Since the true spacecraft variables cannot be obtained directly from the actual plant, a wide long-run simulation campaign was performed using the high-fidelity simulator described in the previous chapters. In the following, we select the most relevant configurations among all the simulations carried out during this campaign, and we summarize the obtained results. In all the simulated conditions, the NGGM mission requirements, detailed in Table 4.1, were checked. All the tests were performed with a simulation time lasting for 2000 orbits.
As previously specified, for the development of an NMPC framework for the NGGM formation control, a sampling time T_s as large as possible had to be considered in order to avoid interference with the wide-band drag-free control. For what concerns the prediction horizon, instead, it was chosen with a trial and error procedure remaining as close as possible to the duration of the orbital period, that is $P = 5487\ s$. For each NMPC configuration reported in the following, the main design parameters have been grouped in some tables. Specifically, these relevant parameters are: the sampling time T_s, the prediction horizon T_p, the weight matrices Q, P and R, and the command lower and upper bounds L_b and U_b which represent the input constraints. Further, another quantity to be taken into account

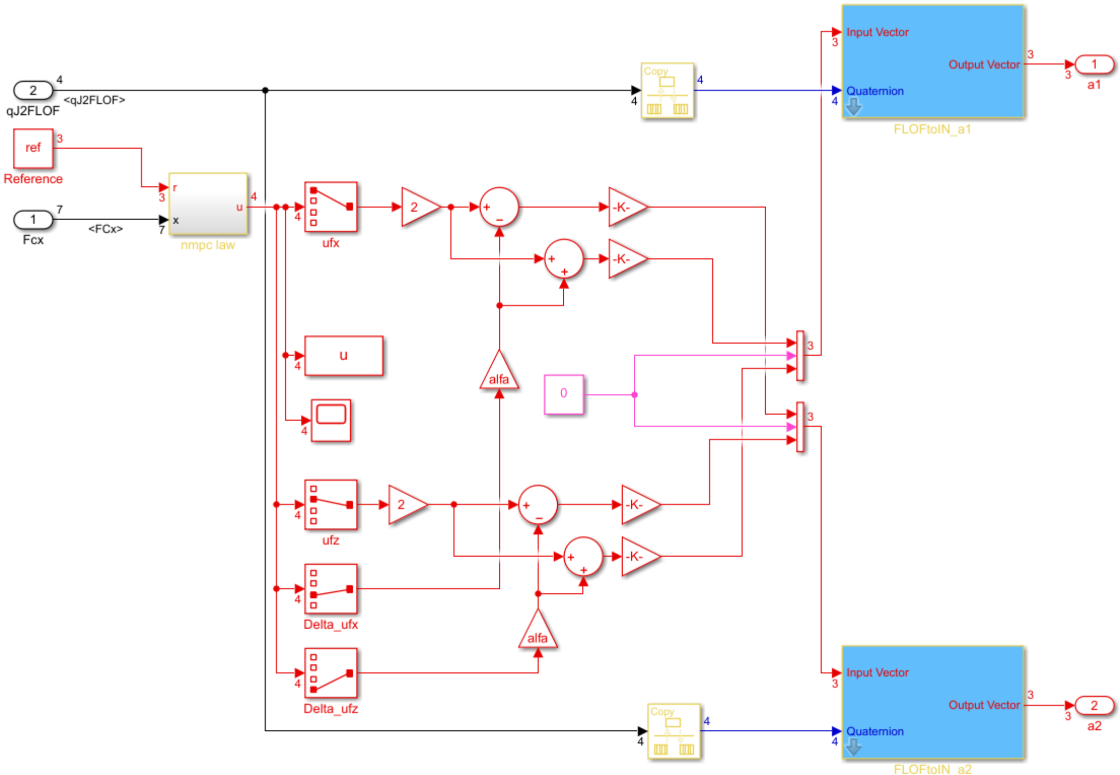

Figure 4.11: Formation Control Block Scheme

is the order of spherical harmonics used in the nonlinear simulator for the gravity model. As a matter of fact, the first three simulations were performed using a 2nd order gravity model $J2$ in order to reduce the gap between the nonlinear model, namely the plant, and the internal prediction model of the NMPC algorithm which, as explained in Section 4.3, considers only the spherical gravity term while treating the higher order terms as external disturbances.
The first configuration presented in this section is reported in Table 4.2. According to what has been said so far, the prediction horizon was chosen with a trial and error procedure as $T_p = 4000\ s$; indeed, this value turned out to be the best trade off between closed-loop stability properties and tracking accuracy. Then, the sampling time was chosen as large as possible noticing that values greater than $T_s = 400\ s$ failed in guaranteeing the system stability. Further, the lower and upper bounds on command input were selected low enough to ensure a very small command effort, and the diagonal elements of the weight matrices were obtained with a trial and error procedure. Finally, as already explained, the $J2$ (2nd order) gravity term was initially adopted for the gravity model of the nonlinear simulator so as to proceed step by step in reducing the gap with the IFC internal prediction model, however leading in this way to a less realistic situation. The NMPC configuration in Table 4.2 was firstly simulated considering the ideal case where the plant is exactly equal to the model used for the prediction, as detailed in Section 4.7.1. Figure 4.13 depicts the behaviour of the first three state variables, namely the output variables ρ_x, ρ_z and Δd of

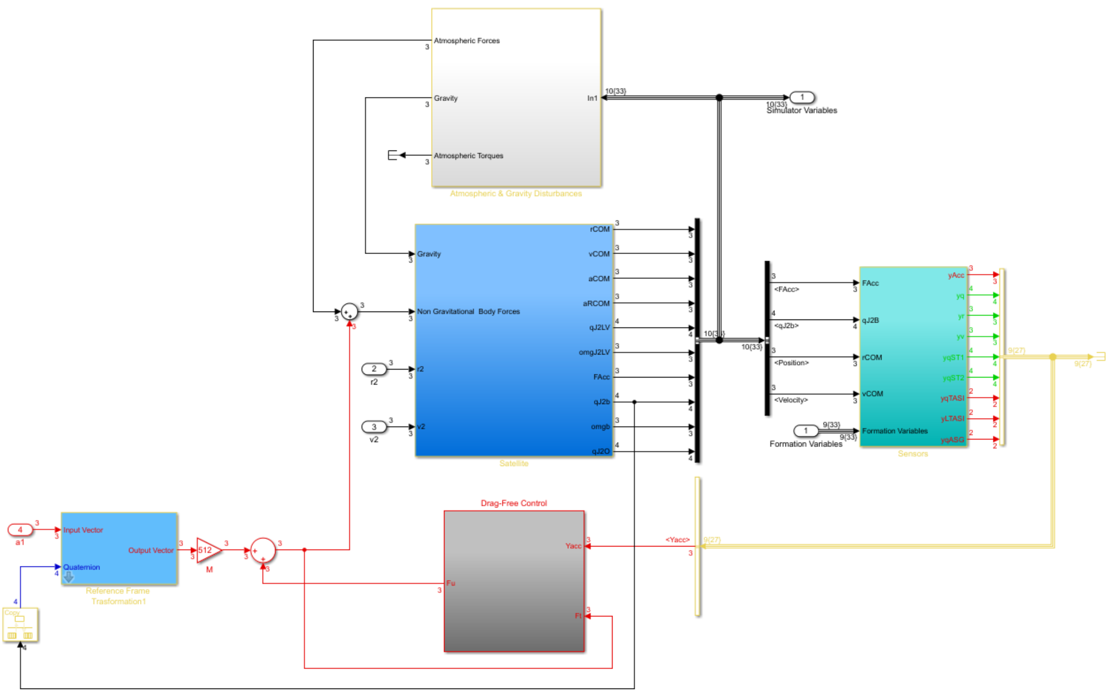

Figure 4.12: Satellite Block Scheme after Introducing the Formation Control

Parameter	NMPC Configuration 1
T_s	400 s
T_p	4000 s
Q	$diag$([1,1,1])
P	$diag$([1,1,1])
R	$diag$([0.5,0.5,0.5,0.5])
L_b	[-7e-7, -7e-7, -5e-7, -5e-7]
U_b	[7e-7, 7e-7, 5e-7, 5e-7]
Gravity	Order 2

Table 4.2: NMPC Configuration 1

the IFC model, in this ideal situation. As we can notice from the picture, the developed NMPC framework is able to stabilize the system not only maintaining limited the value of the states but also making their amplitude converge towards the zero value.
After having make sure that the identified configuration worked in the ideal case, we implemented it on the high-fidelity simulator composed by the nonlinear plant affected by both atmospheric and gravity disturbances as detailed in Section 4.7.2. Figures 4.14, 4.15 and 4.16 represent respectively the behaviour of the three system output states after a long-run simulation lasting 2000 orbits. In each figure, the bounds imposed on each variable by the formation requirements in Table 4.1 have been highlighted with a green line. In particular,

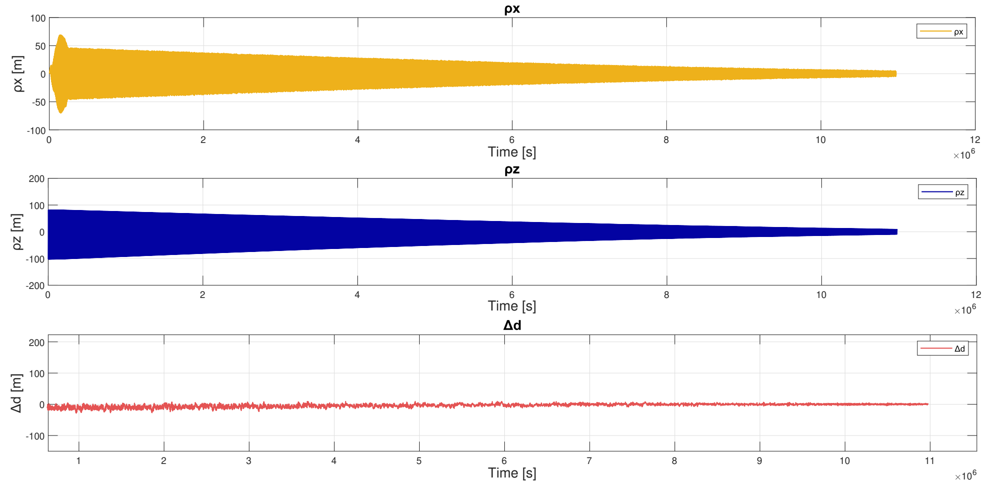

Figure 4.13: NMPC Configuration 1: Behaviour of the State Variables (Ideal Plant)

the formation requirements are split into lateral, radial and distance variations to be calculated with respect to a nominal circular orbit. Specifically, the requirements on distance and lateral variations, namely Δd and ρ_x, are expressed in terms of percentage with respect to the nominal distance $d_{nom} = 100\ km$, while the requirement on the radial variation ρ_z is expressed as a percentage with respect to the nominal altitude $h = 3.453 \times 10^5\ m$.

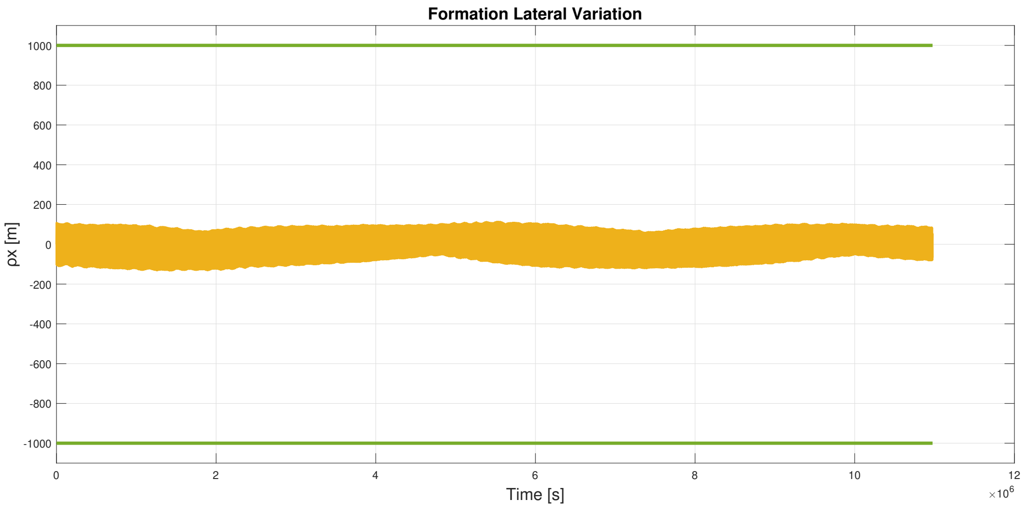

Figure 4.14: NMPC Configuration 1: Formation Lateral Variation

As shown in the figures here reported, because of the presence of model uncertainties and plant nonlinearities, in the realistic situation the behaviour of these state variables get worse if compared to the ideal one in Figure 4.13, in as much as the developed NMPC

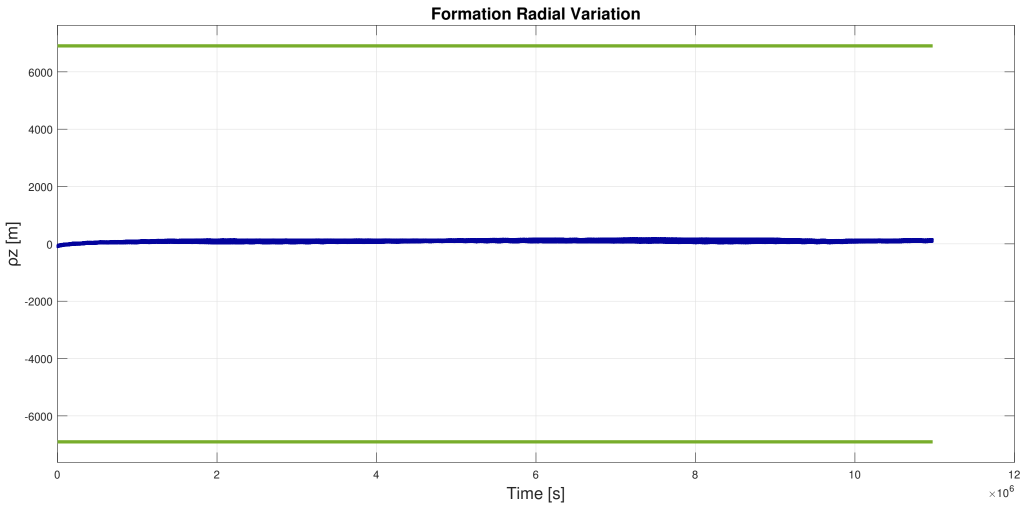

Figure 4.15: NMPC Configuration 1: Formation Radial Variation

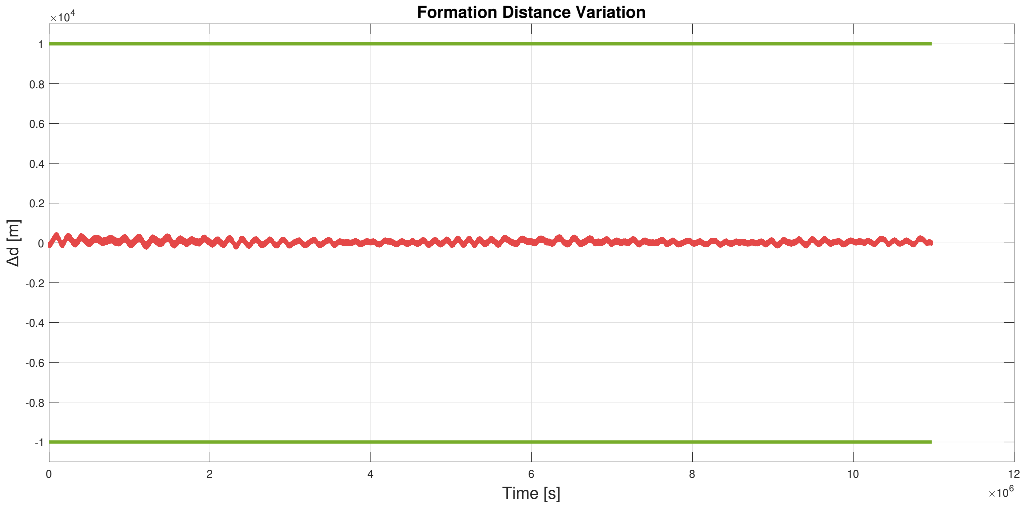

Figure 4.16: NMPC Configuration 1: Formation Distance Variation

framework is not able anymore to ensure the convergence towards the zero value. Nevertheless, looking at the requirements in Table 4.1, we can notice that they only require the NMPC capability to ensure the orbit and formation long-term stability, though admitting large 'natural' fluctuations around the altitude and distance nominal values. Consequently, since the variables do not diverge and their value widely remain inside the specified limits, it is possible to state that this first NMPC configuration is anyway able to stabilize the system as the only task of orbit and formation control is to maintain the state variables bounded in order to meet the scientific requirements, even without necessarily guaranteeing the tracking accuracy.
In the following (Figure 4.17), the plot of the Satellite-to-Satellite Distance is reported in order to show that this variable remains around its nominal value throughout the entire

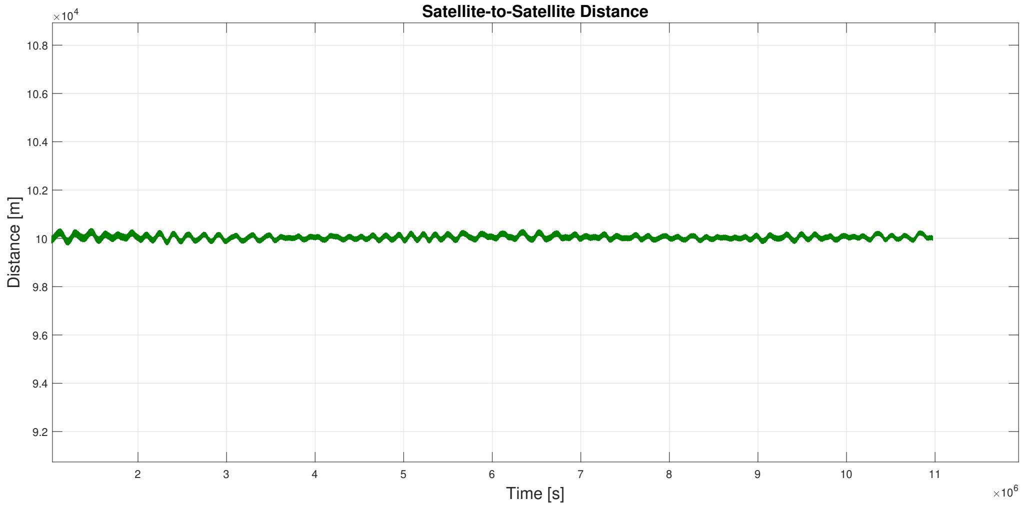

Figure 4.17: NMPC Configuration 1: Satellite-to-Satellite Distance

simulation time thanks to the action of the control system.
However, it is worth to recall that the aim of orbit and formation control consists not only in guaranteeing the formation stability but also in cancelling as much as possible the drag-free residual acceleration acting on the two satellites. In this context, in order to have an idea about how much the developed control framework is able to fulfill this last task, let's report in Figure 4.18 the three components of the body drag-free residual acceleration. For the sake of brevity, only the Satellite 1 drag-free residual acceleration has been reported since the behaviour of this quantity is more or less the same for both satellites.
The performed simulations made it clear that the drag-free residual acceleration was directly proportional to the command input. As a matter of fact, the behaviour depicted

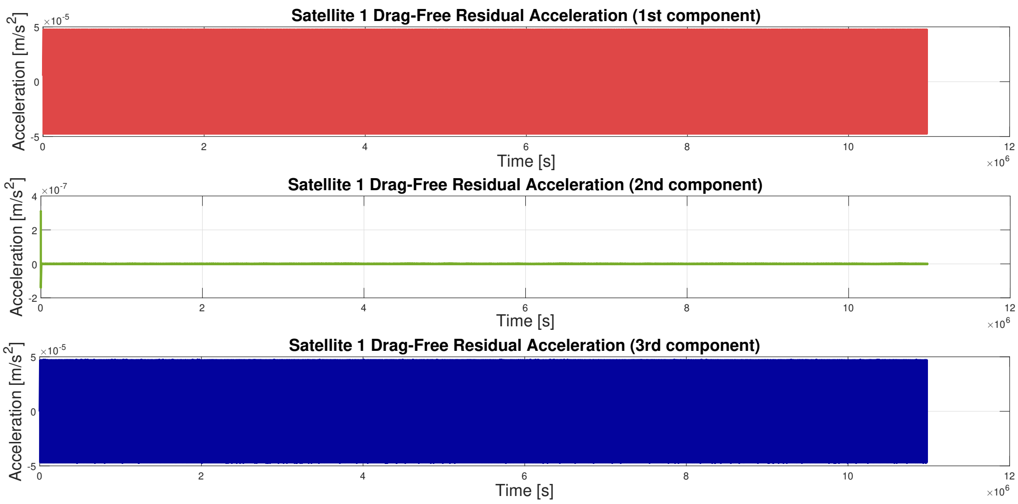

Figure 4.18: NMPC Configuration 1: Satellite 1 Body Residual Acceleration

in the figure follows the shape of the command action that with this configuration was always in saturation because of the very stringent input constraints. From Figure 4.18, we can notice that the maximum value of the drag-free residual acceleration obtained with this configuration is about 5×10^{-5} m/s^2. Even if this value is quite small, in order to furtherly increase the effectiveness of the developed orbit and formation control, several other NMPC configurations were tested during our simulation campaign.
The second presented NMPC configuration, whose parameters have been collected in Table 4.3, had the intent to improve the simulated results presented so far by reducing the input constraints in order to lower the residual acceleration. At this purpose, in the new configu-

Parameter	NMPC Configuration 2
T_s	400 s
T_p	4000 s
Q	$diag([1,1,1])$
P	$diag([1,1,1])$
R	$diag([1e17,1e17,1e15,1e14])$
L_b	[-αe-5, -αe-5, -5e-5, -5e-5]
U_b	[αe-5, αe-5, 5e-5, 5e-5]
Gravity	Order 2

Table 4.3: NMPC Configuration 2

ration the command lower and upper bounds have been modified in order to have smaller limits on the first two input components, namely u_{fx} and u_{fz}, while the diagonal elements of the R matrix, that is the one related to the command activity, have been chosen as large as possible with respect to the Q and P matrices, in order to penalize the control signal and try to stabilize the system with less weighted energy. Even in this case, the first sim-

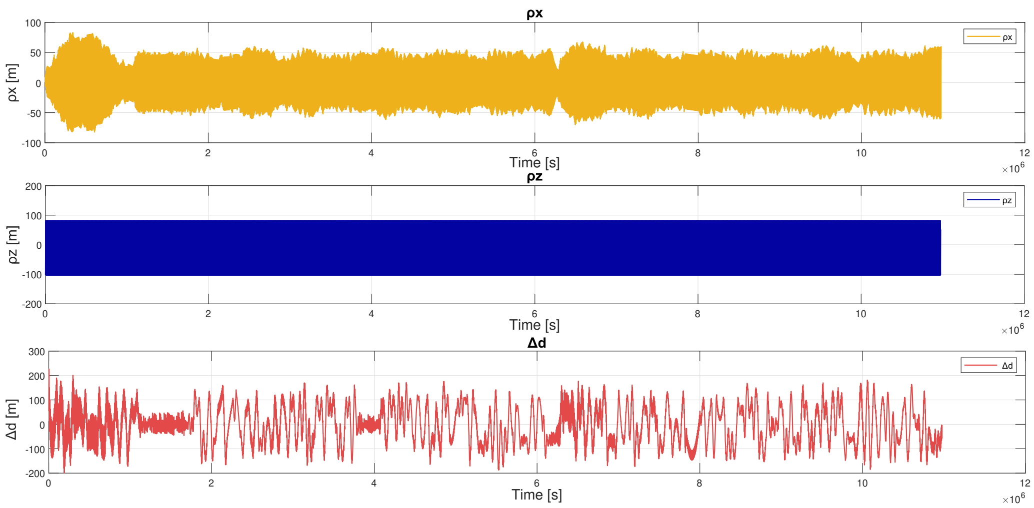

Figure 4.19: NMPC Configuration 2: Behaviour of the State Variables (Ideal Plant)

ulation was carried out considering the ideal situation (plant = prediction model), whose results have been reported in Figure 4.19. As it is evident, this time, even in the ideal case the developed NMPC framework is not able to guarantee the state convergence to zero but succeeds in any way in stabilizing the system maintaining limited the state variation. Introducing this second NMPC configuration on the nonlinear plant, the behaviour of the three output variables with their respective bounds have been reported in Figures 4.20, 4.21 and 4.22.

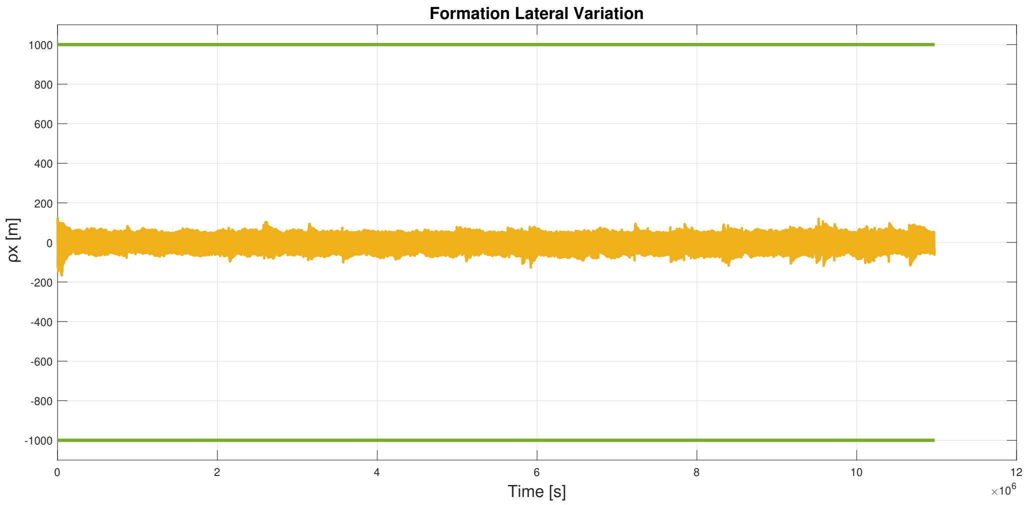

Figure 4.20: NMPC Configuration 2: Formation Lateral Variation

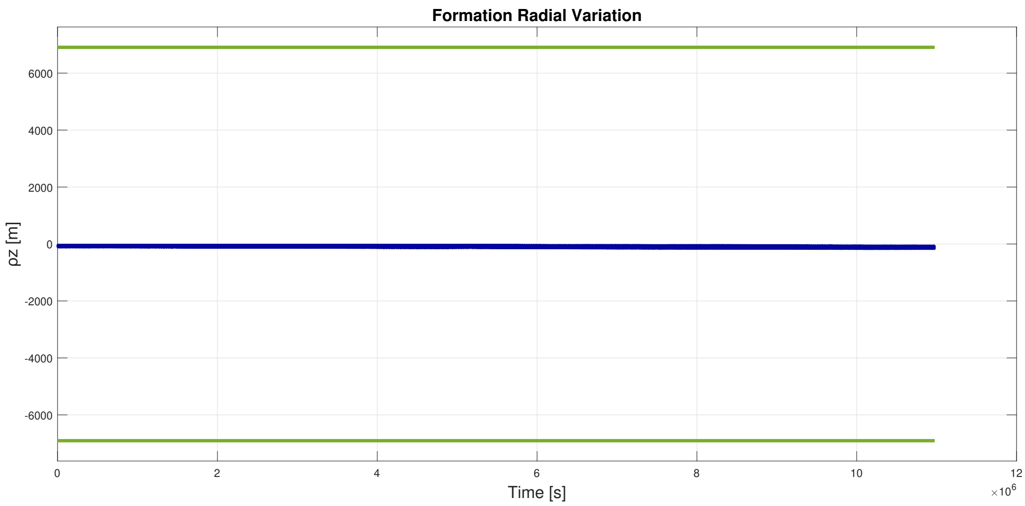

Figure 4.21: NMPC Configuration 2: Formation Radial Variation

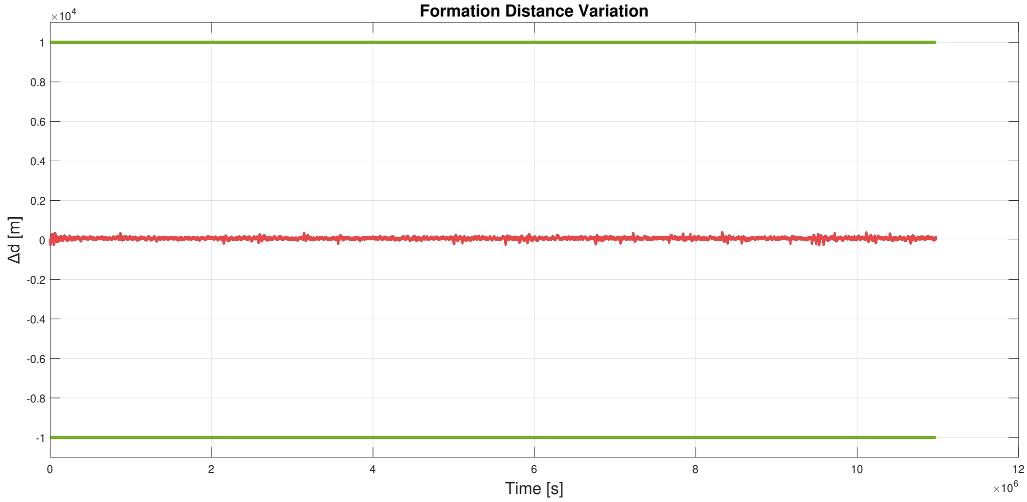

Figure 4.22: NMPC Configuration 2: Formation Distance Variation

As for the previous case, the state variables widely remain inside the green horizontal lines which represent for each variables the correspondent requirement of Table 4.1. In this way, the following figures are able to prove the capability of the new NMPC configuration of ensuring that the perturbations affecting the spacecraft altitude and the inter-satellite distance remain bounded during the mission lifetime. At this point, as previously done for the first configuration, the plot of the formation distance has been reported (Figure 4.23) in order to clearly show that even with these parameters the NMPC is able to ensure the formation stability and maintain the Satellite-to-Satellite Distance close to its reference value.

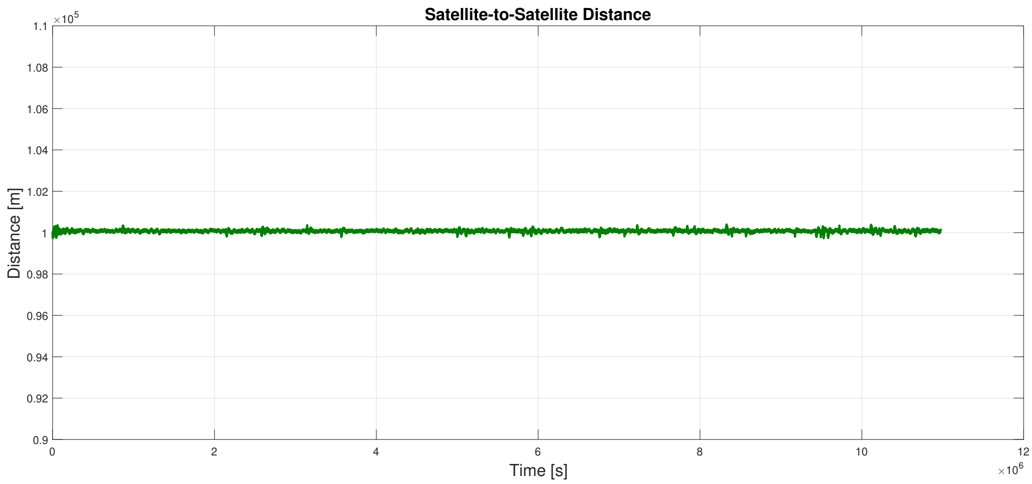

Figure 4.23: NMPC Configuration 2: Satellite-to-Satellite Distance

Further, besides guaranteeing the formation stability, this configuration is also able to improve the cancellation of the drag-free residual acceleration, whose plot in Figure 4.24, exhibits a maximum value a little smaller than before ($3.5 \times 10^{-5} m/s^2$), proving that reducing the command input it is possible to better counteract the drag-free residual acceleration.

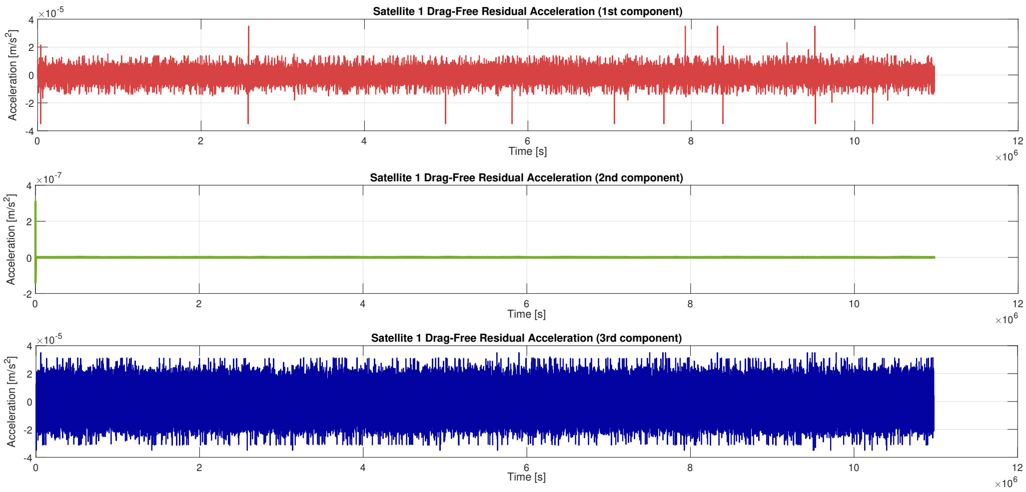

Figure 4.24: NMPC Configuration 2 : Satellite 1 Body Residual Acceleration

In order to have a more significant reduction of this quantity, a third NMPC configuration, reported in Table 4.4 was implemented. Taking into account the fact that the drag-free residual acceleration follows the behaviour of the command input, the command lower and upper bounds have been even more reduced, considering smaller limits also on the last two input components Δu_{fx} and Δu_{fz}. Nevertheless, in order to use such a stringent command constraint, it has become necessary to choose the diagonal elements of the R matrix smaller than those of the Q and P matrices, letting the input to saturate again as bigger elements were not able anymore to further lower the command action. Moreover, it is worth to point out that in order to compensate the introduction of a stricter input constraint and ensure the system stability a lower value of sampling time T_s has been adopted.

Parameter	NMPC Configuration 3
T_s	10 s
T_p	4000 s
Q	$diag$([1,1,1])
P	$diag$([1,1,1])
R	$diag$([0.5,0.5,0.5,0.5])
L_b	[-1e-7, -1e-7, -1e-7, -1e-7]
U_b	[1e-7, 1e-7, 1e-7, 1e-7]
Gravity	Order 2

Table 4.4: NMPC Configuration 3

Figure 4.25 represents the behaviour of the first three state variables in the ideal case (plant = prediction model). This time, the first two states, namely ρ_x and ρ_z, remain limited while the third state Δd slowly converges towards a value close to zero.

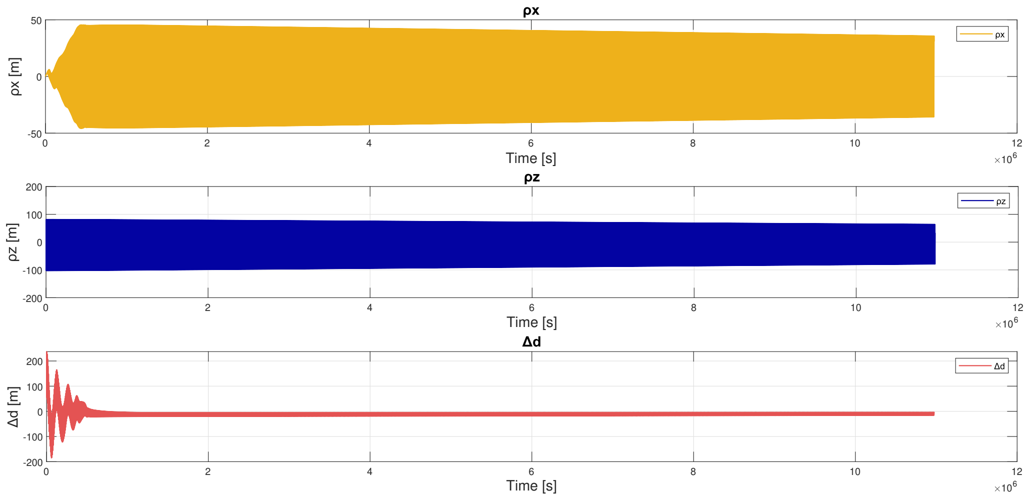

Figure 4.25: NMPC Configuration 3: Behaviour of the State Variables (Ideal Plant)

After this initial step, the NMPC configuration written above was embedded in the nonlinear model for performing the simulation in realistic conditions, whose results have been reported in Figures 4.26, 4.27 and 4.28. As it is evident, despite the larger oscillations introduced on the plot of third state, the implemented NMPC controller is still able to stabilize the system since its states remain inside the required bounds highlighted in green. The worsening with respect to the ideal case is obviously caused by the fact that in the realistic situation we are considering a nonlinear plant much more complex than the model used for the internal prediction of the control algorithm.

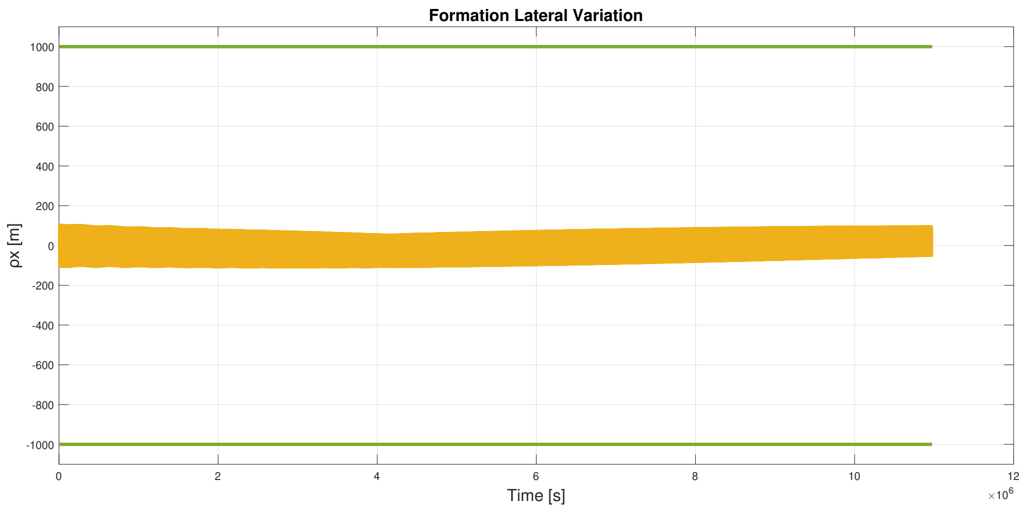

Figure 4.26: NMPC Configuration 3: Formation Lateral Variation

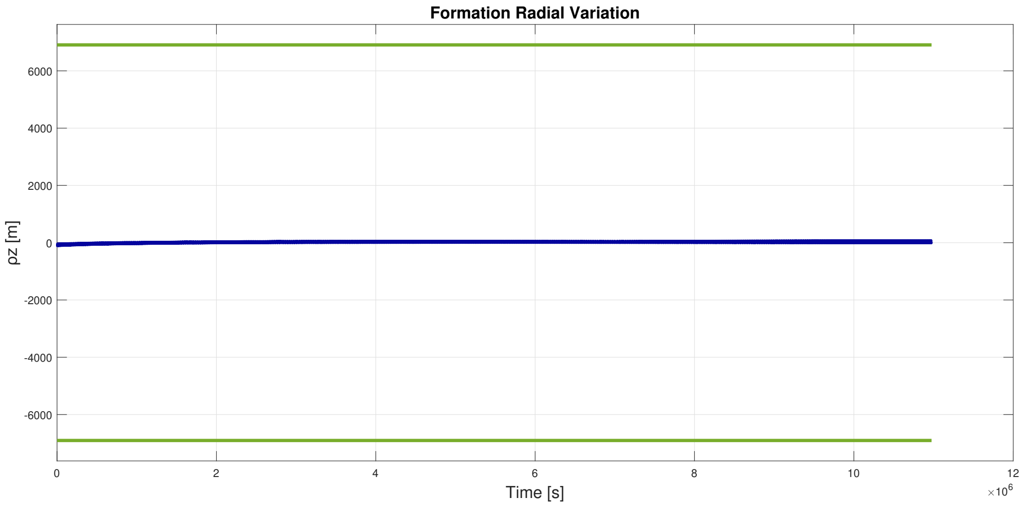

Figure 4.27: NMPC Configuration 3: Formation Radial Variation

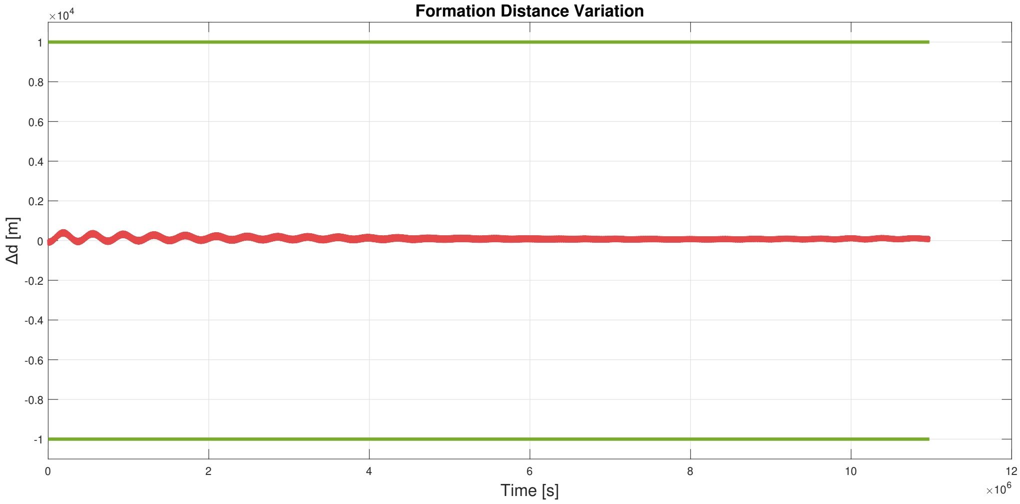

Figure 4.28: NMPC Configuration 3: Formation Distance Variation

The Satellite-to-Satellite distance behaviour obtained with this third NMPC configuration is shown in Figure 4.29, again with the aim to prove that, as in the previous cases, the implemented control system succeeds in maintaining the two satellites at the desired distance.
Finally, to verify that the new NMPC framework brings an improvement with respect to the previous configurations, the last thing to check is the value of the drag-free residual acceleration. According to what has been said before, having reduced the command input,

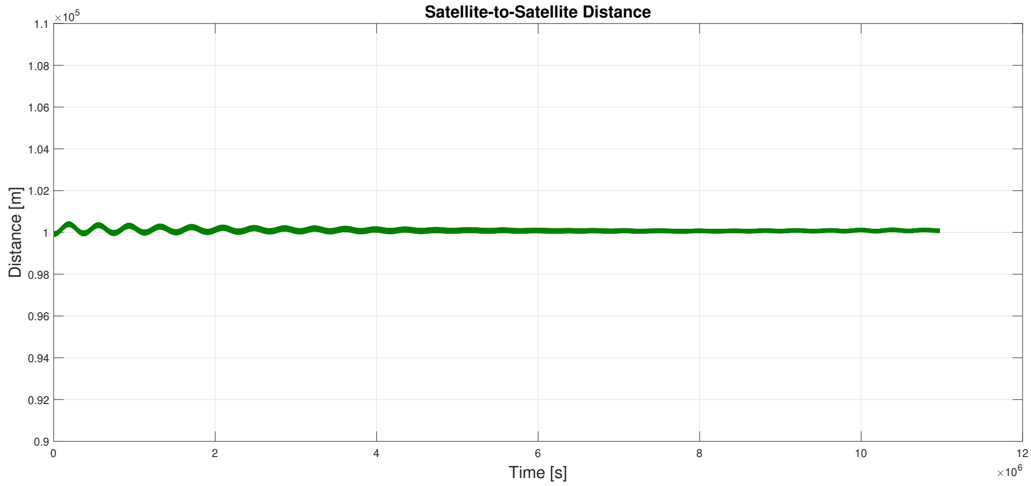

Figure 4.29: NMPC Configuration 3: Satellite-to-Satellite Distance

the plot of the drag-free residual acceleration should exhibit a behaviour that follows the shape of the control signal reaching a maximum level much smaller than before.
Figure 4.30 is the one related to the drag-free residual acceleration that, as expected, shows a clear improvement if compared to the previous cases. As a matter of fact, its amplitude oscillates between a minimum and a maximum value following the shape of the command input that goes always in saturation due to the small lower and upper bounds. The improvement is evident from the fact that the maximum value is reduced of an order of magnitude with respect than before ($6 \times 10^{-6} m/s^2$).

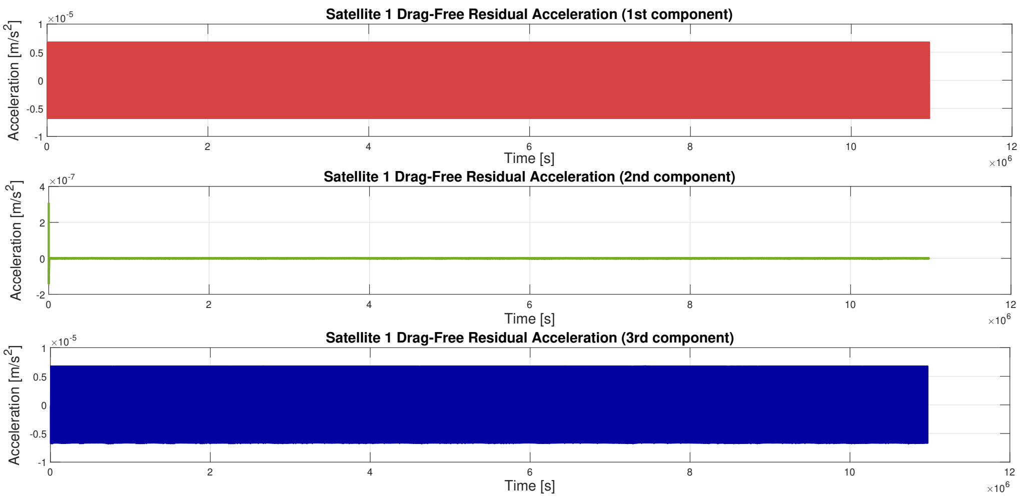

Figure 4.30: NMPC Configuration 3: Satellite 1 Body Residual Acceleration

Now, let's recall that in the simulations discussed so far a 2nd order gravity model was adopted for the nonlinear plant. J2 is certainly one of the most popular gravity models since it allows to consider the flattening of the Earth, differently from the spherical one. Nonetheless, even if it is widely adopted for a lot of space applications, we need to consider that this gravity model could result too approximated for the ambitious goal of our study, that is the measurement of the temporal variations of the Earth gravity field. Consequently, a more accurate gravity model needs to be adopted for the problem under study. At this purpose, the aim of the fourth and final configuration, whose parameters have been reported in Table 4.5, is to implement an NMPC framework able to guarantee the formation stability using a nonlinear model that exploits the 30th order of spherical harmonics for the derivation of the gravity potential.

Parameter	NMPC Configuration 4
T_s	10 s
T_p	4000 s
Q	$diag([1, 1, 1])$
P	$diag([1, 1, 1])$
R	$diag([0.5, 0.5, 0.5, 0.5])$
L_b	[-αe-5, -αe-5, -5e-5, -5e-5]
U_b	[αe-5, αe-5, 5e-5, 5e-5]
Gravity	Order 30

Table 4.5: NMPC Configuration 4

Obviously, increasing the order of the gravity model, the gap between the IFC model used for the internal prediction of the control algorithm and the nonlinear model used to simulate the plant, significantly increases. Indeed, because of this modification, it became necessary both to relax again the input constraints, restoring those of the second configuration, and to maintain the sampling time small as the one used in the third configuration.

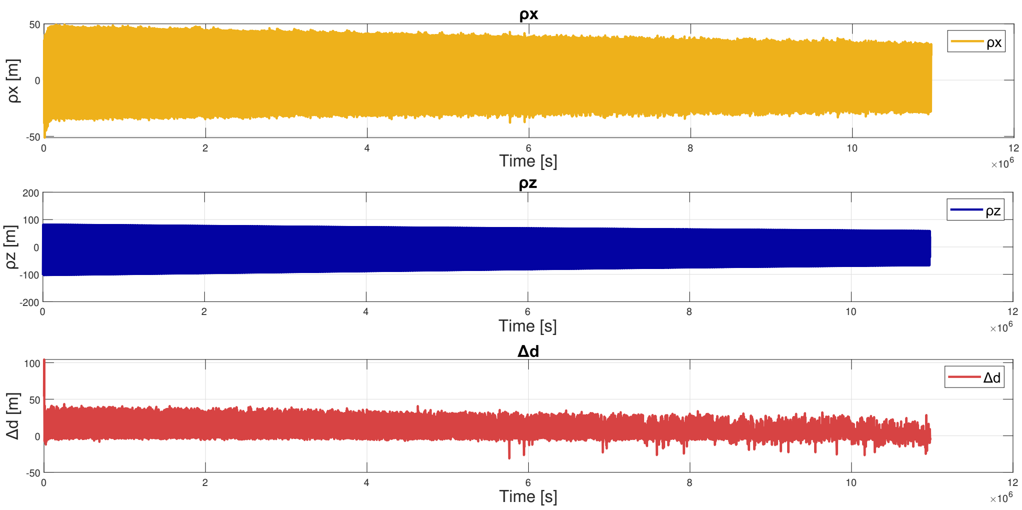

Figure 4.31: NMPC Configuration 4: Behaviour of the State Variables (Ideal Plant)

The simulations performed with this last NMPC framework have shown that the behaviour of the state variables in the ideal case (plant = prediction model), depicted in figure 4.31, is similar to the one obtained with the second configuration as the parameters adopted in the two cases are exactly the same apart from the sampling time T_s. In particular, with this configuration, it is possible to observe a slightly faster convergence of the state variables precisely because of the smaller value of the sampling time.
After the simulation with the ideal plant, we introduced the 30th order gravity term inside the nonlinear model and we performed the simulation in realistic conditions, whose results have been reported in Figures 4.32, 4.33 and 4.34 with their required bounds.

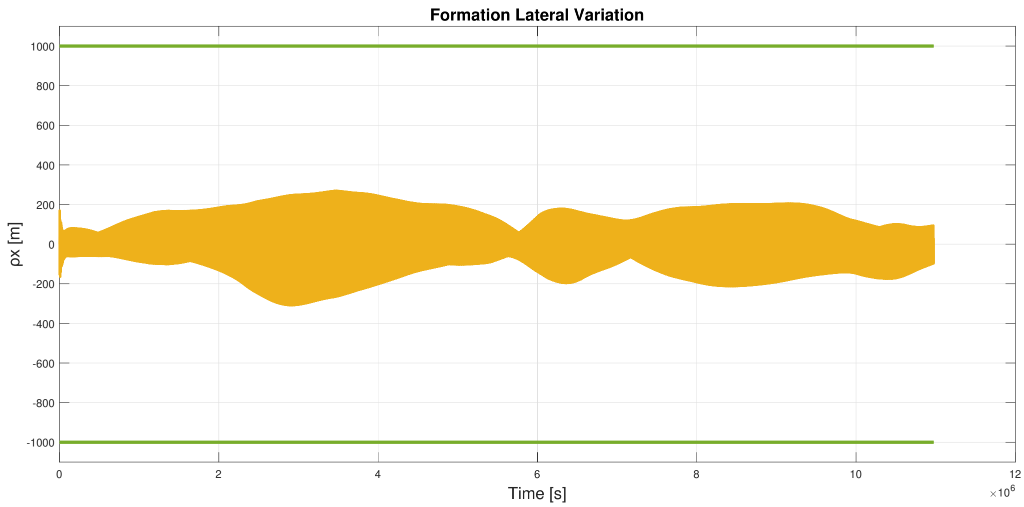

Figure 4.32: NMPC Configuration 4: Formation Lateral Variation

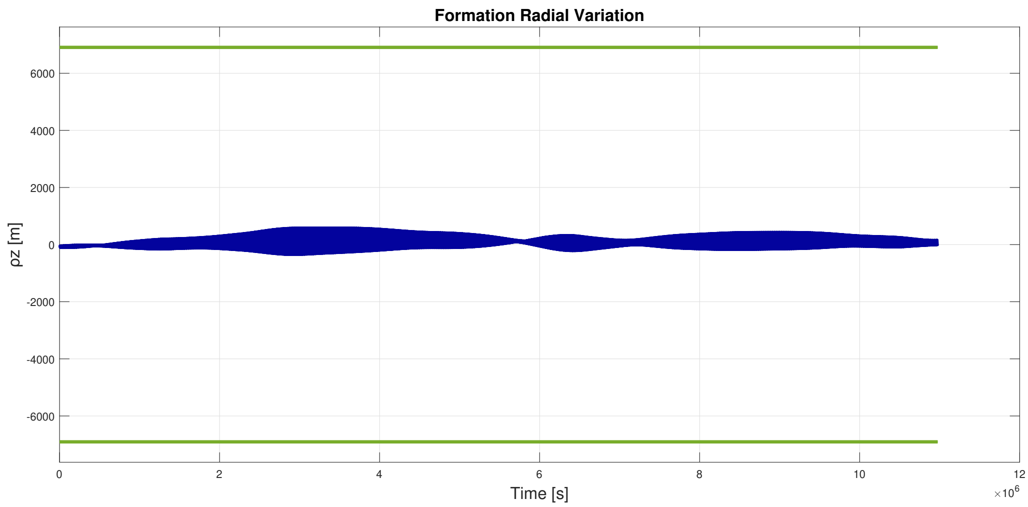

Figure 4.33: NMPC Configuration 4: Formation Radial Variation

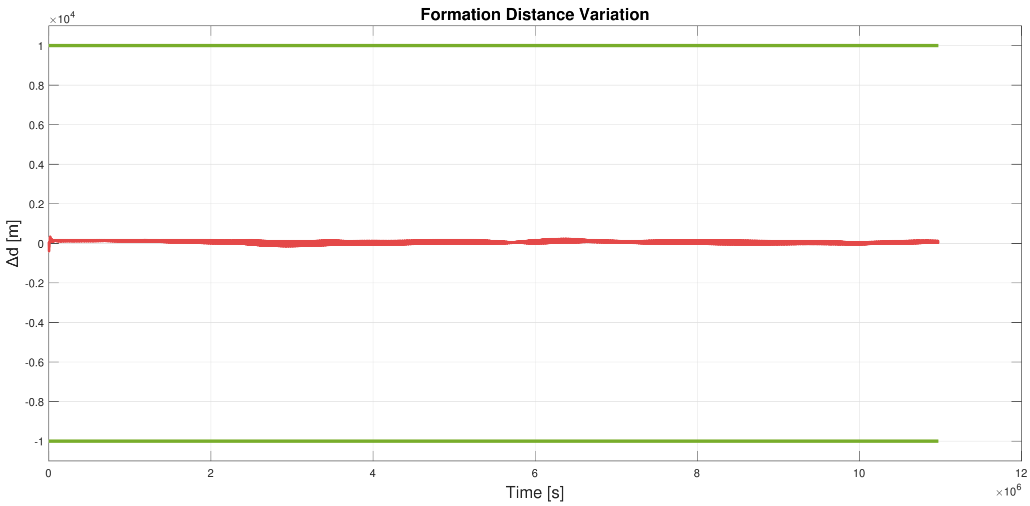

Figure 4.34: NMPC Configuration 4: Formation Distance Variation

As we can notice, this configuration brings some worsening in the states ρ_x and ρ_z that are now affected by greater fluctuations of the amplitude value, but hopefully these worsening do not impinge the NMPC capability of stabilizing the triangular virtual structure since it is still capable of ensuring that the perturbations affecting the formation altitude and the satellite-to-satellite distance remain bounded during the entire simulation time. Further, the plot on the formation distance in Figure 4.35 clearly shows that the the command action is able to avoid the natural divergence of this quantity, by forcing it to stay close to its nominal value $d_{nom} = 100\ km$.
Finally, even for this configuration we checked the capability of the implemented orbit and

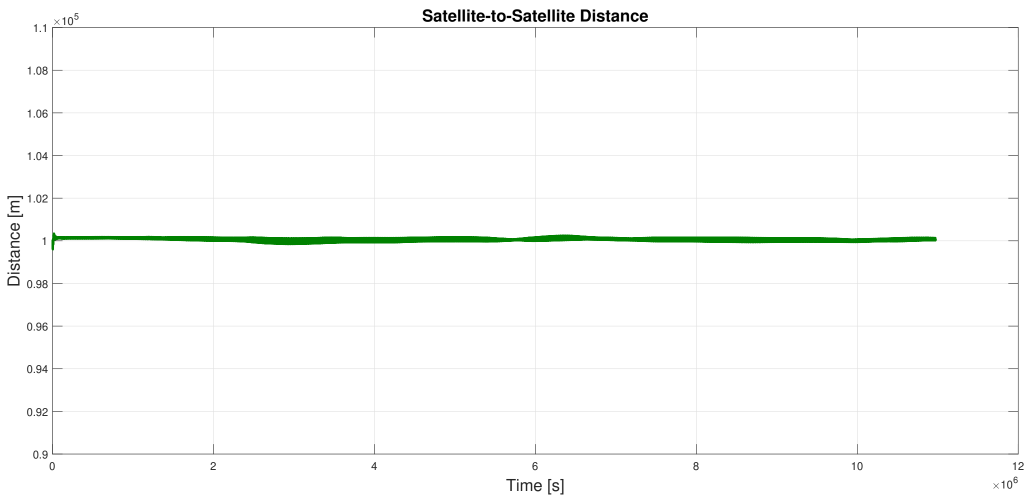

Figure 4.35: NMPC Configuration 4: Satellite-to-Satellite Distance

formation control to cancel the drag-free residual acceleration. In keeping with the considerations previously explained about the relation between the command input and the residual acceleration, the plot of this quantity in Figure 4.36 shows a maximum value of $3.5 \times 10^{-5} m/s^2$, equal to the one obtained with the second configuration. The reason of this similarity consists in the fact that the two configurations adopt the same input constraints. However, the shape of this signal is not exactly equal to that in Figure 4.24 because of the use of a different weight matrix R, which in this case is composed by very small diagonal elements that let the command to saturate.

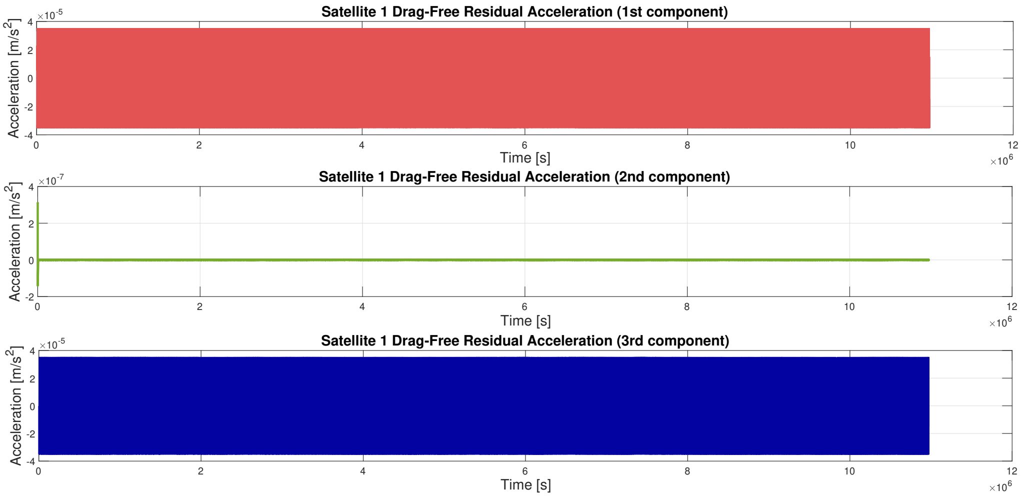

Figure 4.36: NMPC Configuration 4: Satellite 1 Body Residual Acceleration

Chapter 5

Formation Control with Orbit Propagators

This chapter is aimed at introducing the main modelling concepts regarding the development of a low-fidelity orbit propagator to be included inside the non-linear model of our system described in the previous chapters. The reason behind the realization of an orbit propagator consists in the need to take into account the difficulty that exists in the transmission of measurement data between one satellite and its companion due to the absence of a radio-frequency inter-satellite link that makes it necessary assuming long sampling times of measurements (e.g, one orbit).
Consequently, in order to make the simulator even more realistic, low-fidelity orbit propagators have been implemented with the objective of computing on board of each spacecraft the information about the position and velocity of the companion satellite during the time intervals in which no real-time information is available. Indeed, the term propagation concerns the determination of the motion of a body (e.g., a spacecraft) over time. According to the Newton's laws, the motion of a body depends on its initial state (i.e., its position and orientation at some known instant) and the forces acting upon it during its time evolution. The novelty of the propagators implemented in the following consists in their ability to compute accurately the companion satellite orbit, despite having been designed with a computational complexity as low as possible, as it is suggested by the term "low-fidelity" with which we have classified them. Indeed, these propagators do not include all the models of the disturbing forces acting on the satellite, but attempt to approximate the effects of some forces while completely disregarding others. Thanks to their simplicity, low-fidelity propagators are generally the fastest to use and the most appropriate for the proposed design scenario.
Technically, the nominal orbit of a spacecraft is influenced by all the atmospheric and gravitational effects described in Section 2.3, nevertheless for the modelling of these propagators, only the perturbation due to the gravity force has be taken into account, completely neglecting the other atmospheric disturbances. Moreover, to reduce the computational complexity, the gravity model adopted inside the orbit propagator only accounts for the secular variations of the orbital elements due to Earth's oblateness. At this purpose, the model

developed in the following adopts the 4th zonal coefficient of the Earth's gravitational potential (J4), as it is sufficient to obtain the calculation accuracy required for our purpose. Indeed, it is worth to underline that for the proposed design scenario accuracy is not a premium, since the main objective is to design a propagator able to integrate satellite velocity and position with the aim to compute the spacecraft orbit without impinging the capability of the control system to stabilize the formation virtual structure.
In the following, three types of orbit propagators will be implemented. Starting from the simplest one, presented in Section 5.1, we will proceed by trying to improve the way in which the satellite acceleration is derived in order to reduce the approximations and consequently realize a more reliable propagator despite maintaining low the computational complexity.

5.1 Basic Orbit Propagator

The approach adopted for the realization of the orbit propagator presented in the following consists in a cascade of two integrators through which to derive the satellite's propagated velocity and position starting from an approximated value of the satellite acceleration.
For simplicity, in the following we will consider only the orbit propagator of Satellite 2, which is present on board of Satellite 1, but obviously all the considerations that will be made hold also for the orbit propagator of Satellite 1 which is embedded on board of Satellite 2.
According to what has been previously said, due to the absence of a radio-frequency inter-satellite link, we need to assume a sampling time of measurement of at least one orbit; this means that the information about Satellite 2 position and velocity provided by GPS measurements becomes available on Satellite 1 once every orbital period. During the time intervals in which no real-time information is available, Satellite 2 position and velocity need to be computed by means of the orbit propagator. Consequently, the Satellite 2 orbit propagator is embedded inside the Satellite 1 block scheme and receives its input from the sensor measurements of Satellite 2, as it is shown in Figure 5.1. The outputs of the orbit propagator are the propagated Satellite 2 velocity and position which will be used to derive the Formation Variables on board of Satellite 1. In the same way, on Satellite 2 will be present the orbit propagator of Satellite 1, whose outputs will be used to derive the Formation Variables on board of Satellite 2. Since each spacecraft is able to see the real information about its own motion and the propagated information about its companion motion, the formation variables computed on board of each spacecraft are slightly different. As a consequence, it is necessary to embark on board of each satellite a block containing the developed NMPC-based orbit and formation control system which takes as input the formation variables, or more precisely the IFC state variables, computed by the spacecraft on which it is mounted. As it is depicted in Figure 5.1, the Formation Control block provides as output not only the acceleration command needed by the spacecraft on which it is embedded but also the acceleration command related to the other satellite. The orbit propagator presented in this section is the simplest one, thus the information about the acceleration command related to the companion satellite will be not used here, nevertheless it will be exploited for the improved versions presented later.

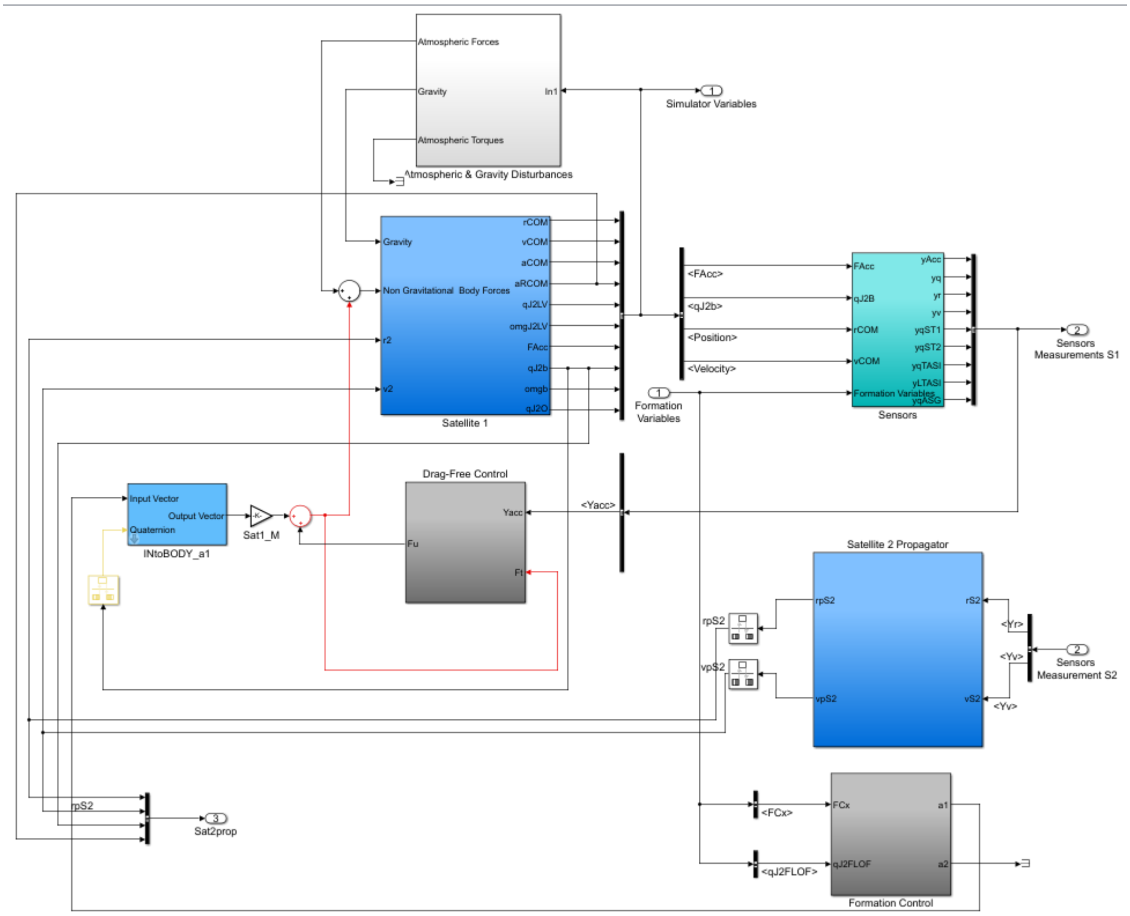

Figure 5.1: Satellite Block Scheme with Basic Orbit Propagator

As already mentioned, the proposed orbit propagators have been developed with the aim of reducing as much as possible the computational load. Consequently, only the perturbation caused by the gravity force has been taken into account neglecting all the other atmospheric disturbances. In this way, in the determination of the approximated value of the satellite acceleration, that is needed to compute the satellite velocity and position, only the term related to the gravitational field is considered while all the non-gravitational forces that actually influence the satellite dynamics are not taken into account. Inside the block of the orbit propagator, reported in Figure 5.2, it is present only the gravity model which takes as input the information provided every sampling time by the GPS measurements and gives as output the value of the gravity acceleration obtained using a 4th order of spherical harmonics. Indeed, this gravity model, being able to provide a quite good approximation of the actual gravitational field, has turned out to be the best trade-off between accuracy and computational complexity. In the Simulink scheme of our simulator, in order to account for the long sampling time of measurement data, two rate transition blocks are used. The sample time of these blocks is decided by a parameter called "propagatorRT" which is set according to the sampling time of the measurement data (e.g, one orbit or more).

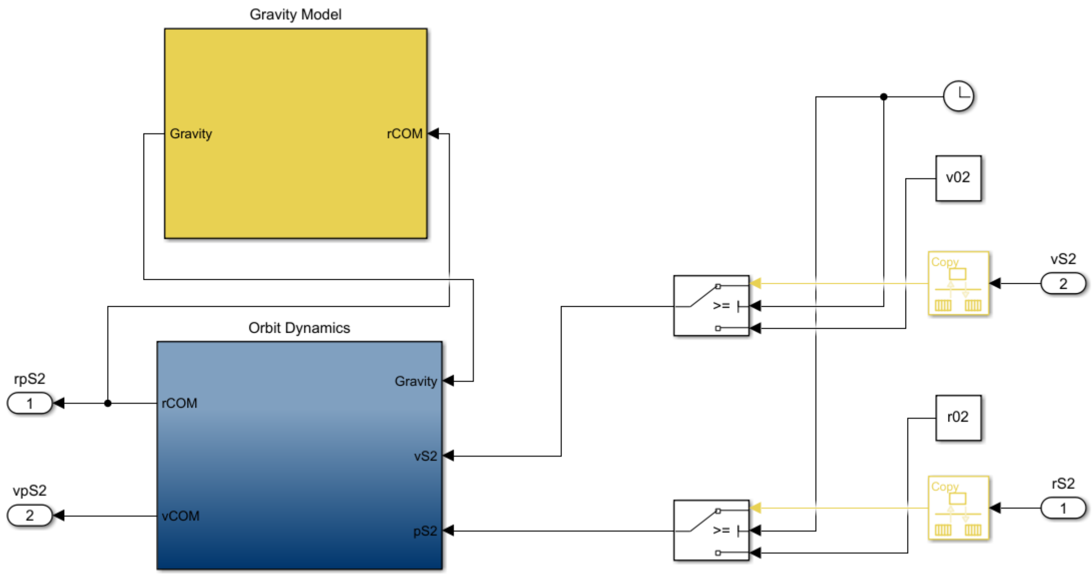

Figure 5.2: Basic Orbit Propagator

In the real satellite dynamics, detailed described in Section 2.2, a lot of contributions are involved. In particular, the satellite acceleration $\boldsymbol{a}_{CoM}$ is given by the sum of the negative gravity acceleration $\boldsymbol{g}$ and all the non-gravitational accelerations which include the atmospheric disturbances (e.g, drag force $\boldsymbol{f}_{drag}$ and solar pressure $\boldsymbol{f}_{sun}$) and the command actions of drag-free control $\boldsymbol{u}_{drag}$ and formation control $\boldsymbol{u}_{form}$:

$$\boldsymbol{a}_{CoM} = -\boldsymbol{g} + \frac{\boldsymbol{f}_{drag}}{m} + \frac{\boldsymbol{f}_{sun}}{m} + \frac{\boldsymbol{u}_{drag}}{m} + \frac{\boldsymbol{u}_{form}}{m} \tag{5.1}$$

Assuming that the drag-free control system is able to fulfill its task, the non-gravitational accelerations due to the atmospheric disturbances are zeroed by the drag-free command action, thus Eq. 5.1 becomes:

$$\boldsymbol{a}_{CoM} \simeq -\boldsymbol{g} + \frac{\boldsymbol{u}_{form}}{m} \tag{5.2}$$

Inside the propagator, in order to reduce the complexity, the satellite acceleration has been approximated only to the negative gravity term. However, it is worth noticing that the gravity model used inside the propagator is slightly different from the one adopted to simulate the real satellite orbital dynamics. Indeed, in the satellite nonlinear model the 30th order of spherical harmonics was used for the gravity force, while inside the orbit propagator a much more approximated gravity model has been considered. Consequently, the acceleration of the satellite CoM, inside the propagator is computed as:

$$\boldsymbol{a}_{CoMp} = -\boldsymbol{g}_{\boldsymbol{4}} \tag{5.3}$$

where $\boldsymbol{g}_{\boldsymbol{4}}$ is used to indicate the gravity acceleration derived by means the 4th order term of spherical harmonics.

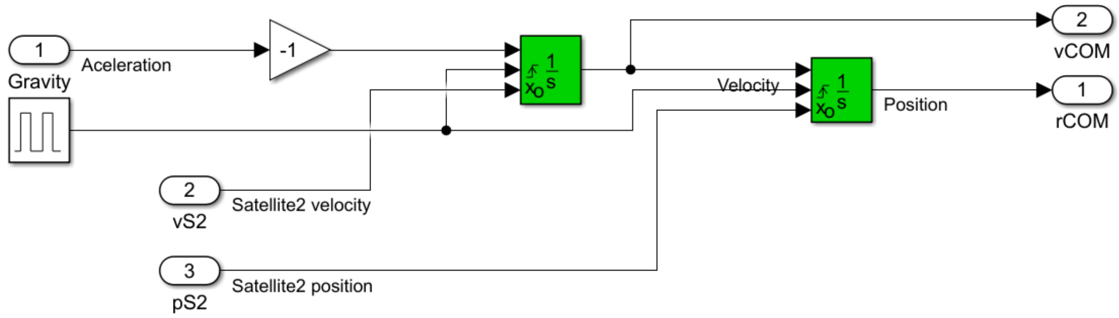

Figure 5.3: Basic Orbit Propagator - Orbit Dynamics

As depicted in Figure 5.3, the two integrators used to propagate the satellite velocity and position are driven by means of a pulse generator whose frequency is decided by the parameter called "PropagatorRT". This parameter is also used to decide when the integrators initial conditions need to be updated during the simulation according to the frequency with which the measurement data of the companion satellite become available on board of each spacecraft.
In the following are reported the plots obtained by the difference between real and propagated velocity and position of Satellite 2 with the intent to draw attention on the effectiveness of the proposed model in the computation of the satellite orbit. For the sake of brevity, Figures 5.4 and 5.5 are both referred only to Satellite 2 but the same considerations hold also for the real and propagated quantities of Satellite 1.

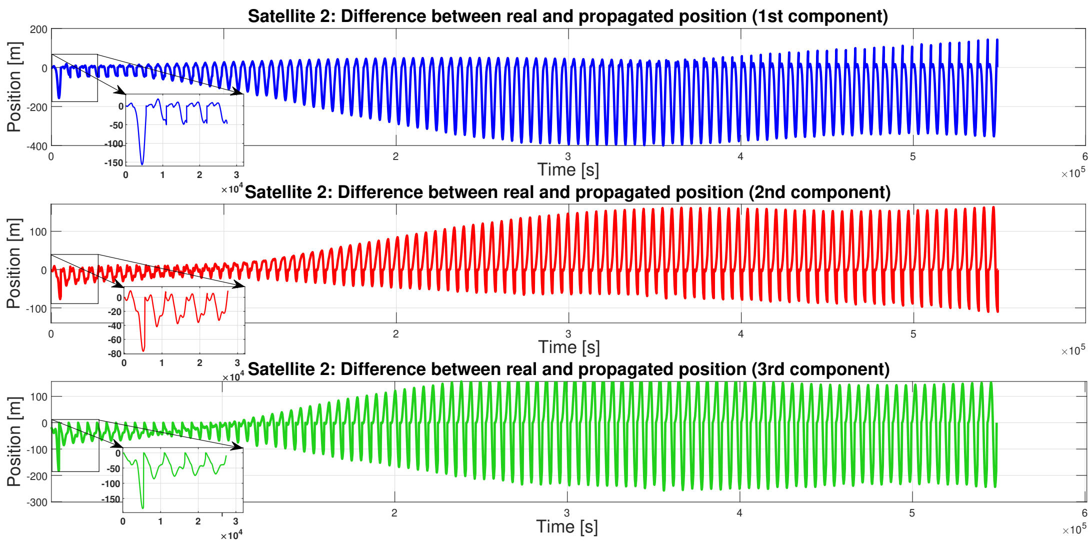

Figure 5.4: Difference Between Real and Propagated Position of Satellite 2

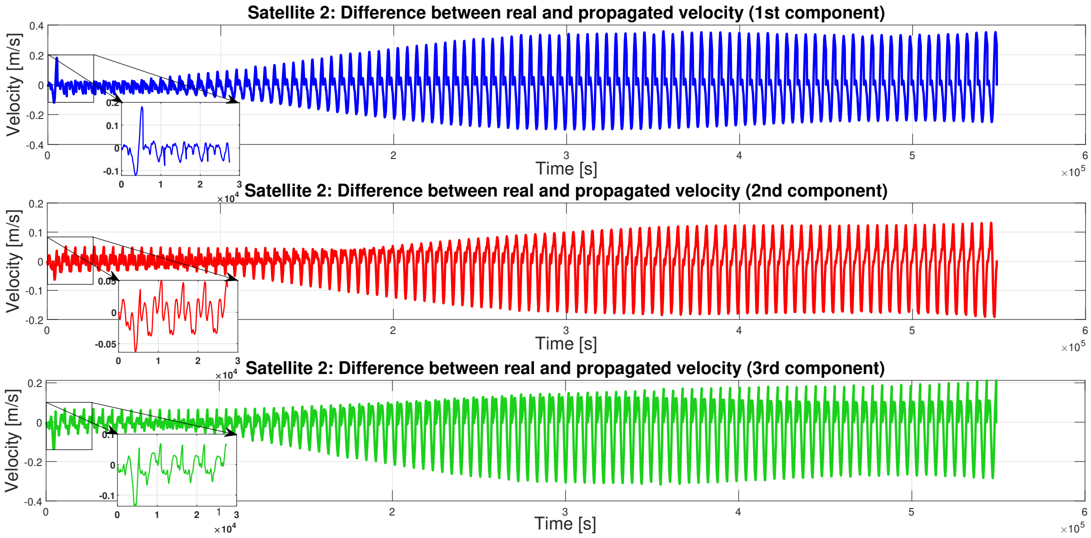

Figure 5.5: Difference between Real and Propagated Velocity of Satellite 2

The simulations performed to obtain the above figures assumed a sampling time of measurements of an orbital period, namely $P = 5487\ s$. Indeed, as we can notice from the zoomed sections, at the end of each orbit the three components of both plots reset to zero as a new data coming from the GPS measurement becomes available to be provided as new initial condition for the two integrators.
Further, the plots here reported, obtained by means of simulation lasting for 100 orbits, show that the developed orbit propagator is able to approximate the real satellite position and velocity maintaining the error quite low. Nevertheless some refinements may be needed due to the fact that each orbital period the error is subject to an increase that in the long run could impinge the control system capability to stabilize the satellite formation.

5.2 Orbit Propagator with Command Action

In order to improve the orbit propagator designed in the previous section, the idea is to compute the satellite acceleration used for the propagation, namely $\boldsymbol{a}_{CoMp}$, in such a way as to reduce to the extent possible the difference with respect to the real satellite acceleration $\boldsymbol{a}_{CoM}$, that is composed by all the quantities specified in Eq. 5.1.
Continuing to assume that the drag-free control is able to perfectly perform the task for which it has been designed, that is the cancellation of the atmospheric disturbances, it is possible to make $\boldsymbol{a}_{CoMp}$ closer to the value in Eq. 5.2 by introducing as input of the orbit propagator the command acceleration coming from the formation control, as shown in Figure 5.6. In this new version of the orbit propagator, the approximated value of the satellite CoM acceleration $\boldsymbol{a}_{CoMp}$ is computed as:

$$\boldsymbol{a}_{CoMp} = -\boldsymbol{g_4} + \frac{\boldsymbol{u}_{form}}{m}. \tag{5.4}$$

As we can notice, this quantity is very similar to the one in Eq. 5.2 with the only difference consisting in the model adopted for the computation of the gravity acceleration that, as we recall, adopts the 4th order of spherical harmonics instead of the 30th order used for the satellite nonlinear model. In this way it is possible to exploit the information about the acceleration command related to the companion satellite that is provided on board of each spacecraft by the Formation Control block.

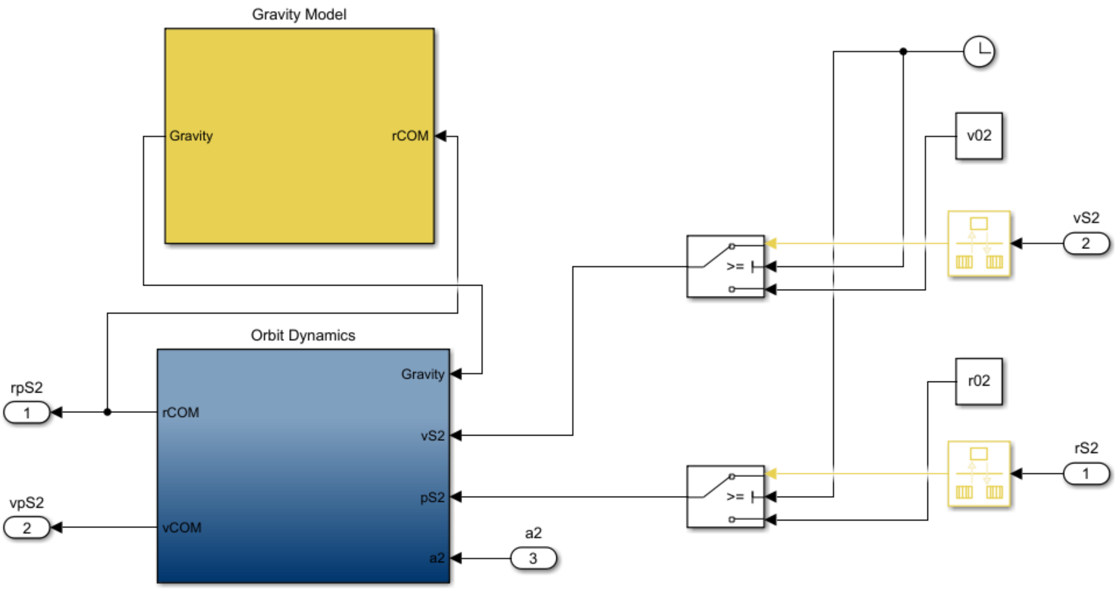

Figure 5.6: Orbit propagator with Command Action

Inside the Orbit Dynamics block of the propagator we find again the two integrators used to compute the satellite propagated velocity and position; the only difference with respect to the previous case consists in the way in which $\boldsymbol{a}_{CoMp}$ is obtained, as it is evident from Figure 5.7, where Eq. 5.4 has been implemented for the derivation of this quantity.

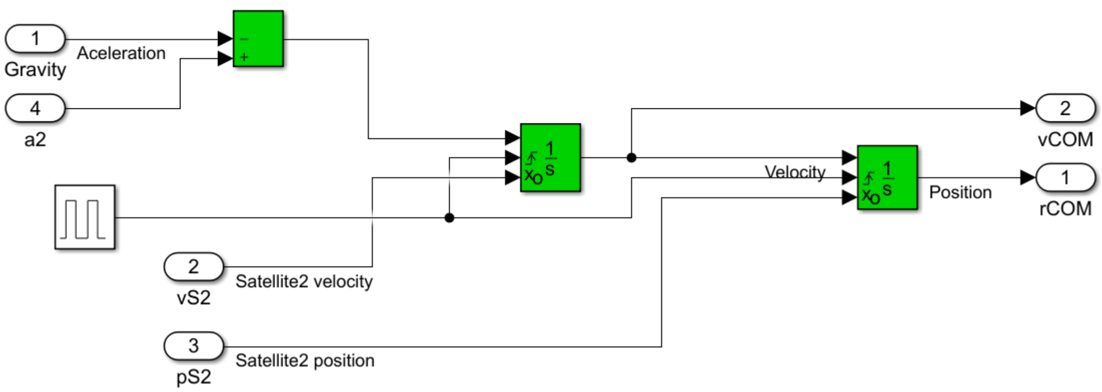

Figure 5.7: Orbit propagator with Command Action - Orbit Dynamics

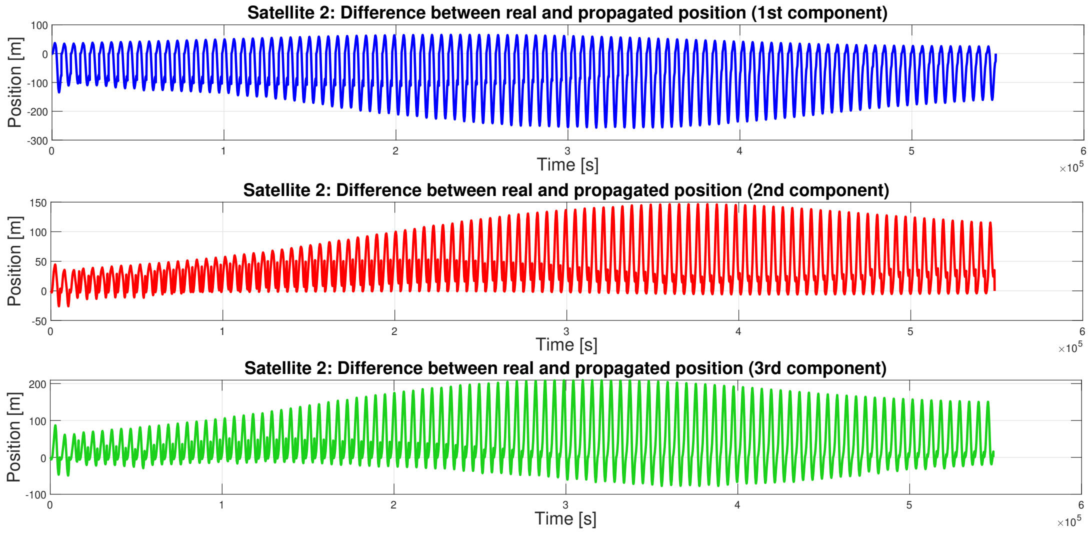

Figure 5.8: Difference between Real and Propagated Position of Satellite 2

After having refined the previous model by introducing the modifications described so far, here the simulated plots of the difference between real and propagated satellite velocity and position are reported with the intent to prove that the new version of orbit propagator is effectively able to bring an upgrade to the previous simulated results.

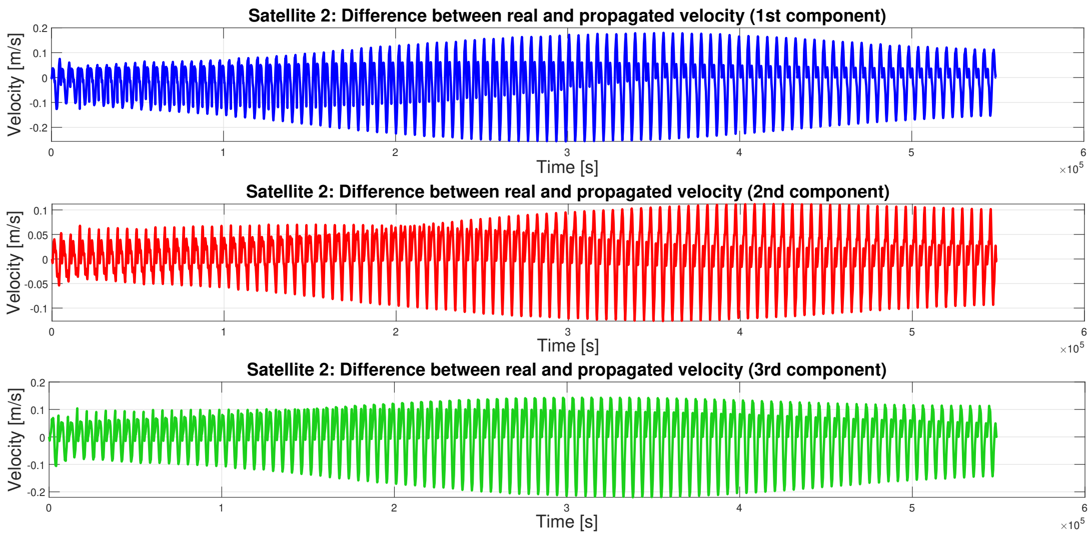

Figure 5.9: Difference between Real and Propagated Velocity of Satellite 2

Figures 5.8 and 5.9 refers both to Satellite 2 and have been obtained by means of a simulation lasting for 100 orbits. Comparing these plots with those reported in Figures 5.4 and 5.5, it is evident how the error committed by the propagator in the computation of the satellite orbit in this last case is much lower than before.

5.3 Orbit Propagator with Error Correction

The previous modification made on the model initially developed has displayed an improvement on the propagator capability of computing the satellite velocity and position. Such improvement has been made evident from the fact that, after the modification, the plots of the difference between real and propagated quantities have showed lower absolute values than before, indicating a better approximation of the satellite's orbit. This section is aimed at further refining the model described so far by exploiting the possibility to embark on board of each spacecraft two orbit propagators, one to compute the orbit of the companion spacecraft and the other one to provide the propagated velocity and position of the spacecraft on which the orbit propagator is mounted, as depicted in Figure 5.10. Let's look for example at the model of Satellite 1 in the figure, to which the orbit propagators of both Satellite 1 and its companion have been added. The idea of this further modification consists in exploiting the error $\boldsymbol{a}_{res}$ that exists between the real and propagated quantities of Satellite 1 to correct the orbit propagation of both satellites. This error, given by the difference between the real and the propagated satellite CoM accelerations, is introduced in both propagators as an additional input, as shown in Figure 5.11. From Eqs. 5.1 and 5.2 the following relation holds:

$$\begin{aligned}\boldsymbol{a}_{res} &= \boldsymbol{a}_{CoM} - \boldsymbol{a}_{CoMp} \\ &= -\boldsymbol{g} + \frac{\boldsymbol{f}_{drag}}{m} + \frac{\boldsymbol{f}_{sun}}{m} + \frac{\boldsymbol{u}_{drag}}{m} + \frac{\boldsymbol{u}_{form}}{m} + \boldsymbol{g_4} - \frac{\boldsymbol{u}_{form}}{m} \simeq -\boldsymbol{g} + \boldsymbol{g_4}.\end{aligned} \tag{5.5}$$

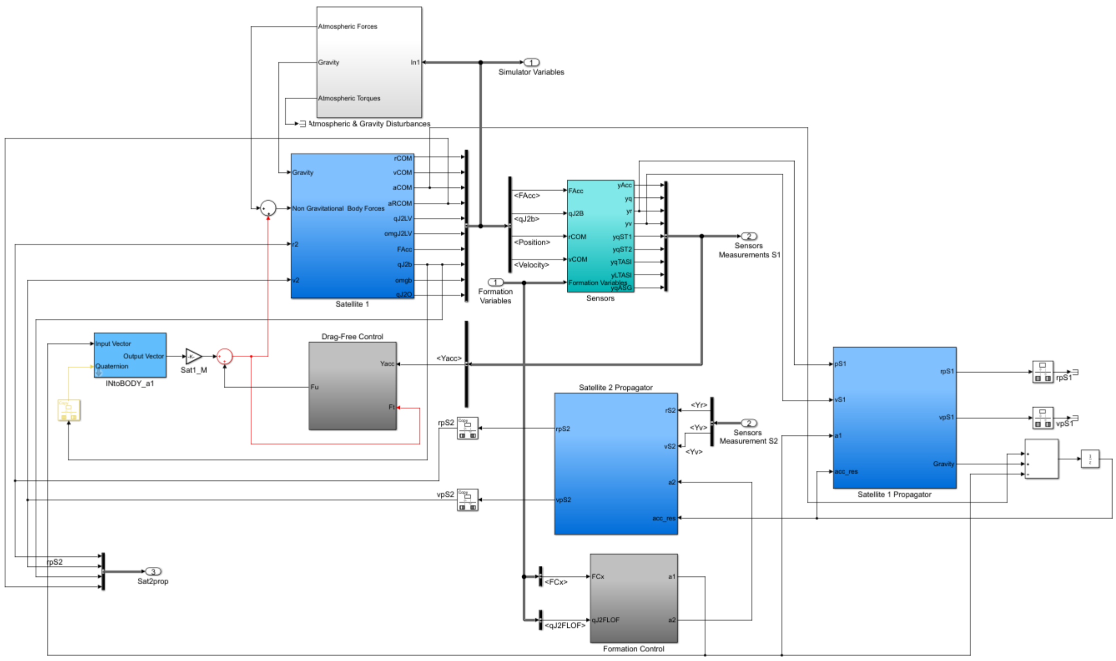

Figure 5.10: Satellite Block Scheme + Orbit Propagators with Error Correction

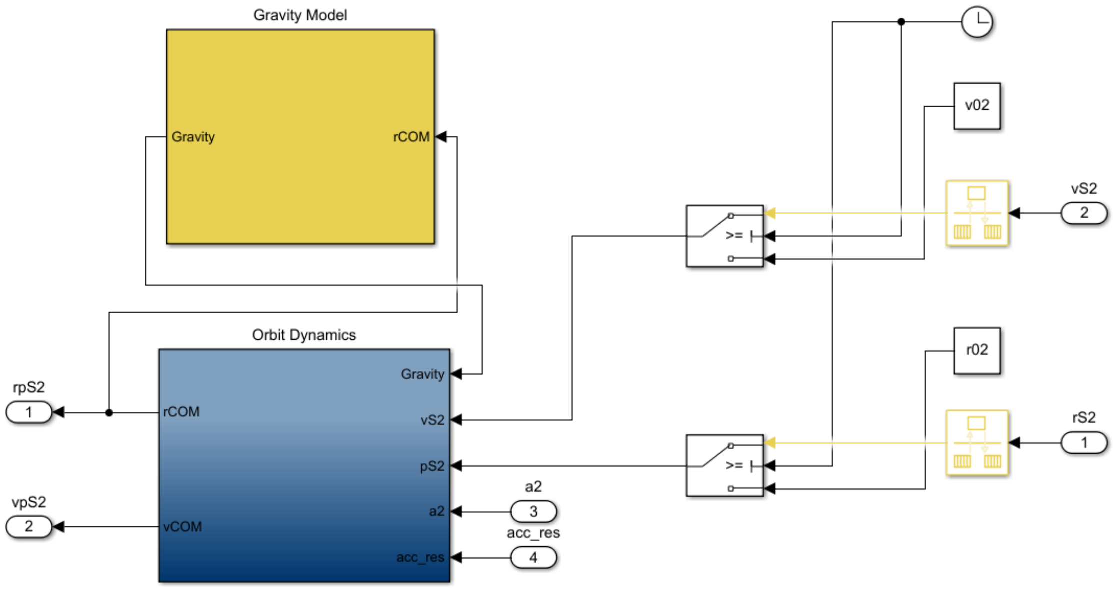

Figure 5.11: Orbit propagator with Error Correction

Thus, since we want the acceleration used inside the propagator to be as similar as possible to the real CoM acceleration $\boldsymbol{a}_{CoM}$, the idea here exploited is to correct $\boldsymbol{a}_{CoMp}$ by adding it the error $\boldsymbol{a}_{res}$ computed at the previous time instant, recalling that from Eq. 5.5 it results:

$$\boldsymbol{a}_{CoM} = \boldsymbol{a}_{res} + \boldsymbol{a}_{CoMp}. \tag{5.6}$$

What has been said so far is implemented in Figure 5.12, where this time the acceleration used as input of the first integrator has been computed as

$$\boldsymbol{a}'_{CoMp} = \boldsymbol{a}_{res} - \boldsymbol{g}_4 + \frac{\boldsymbol{u}_{form}}{m} \tag{5.7}$$

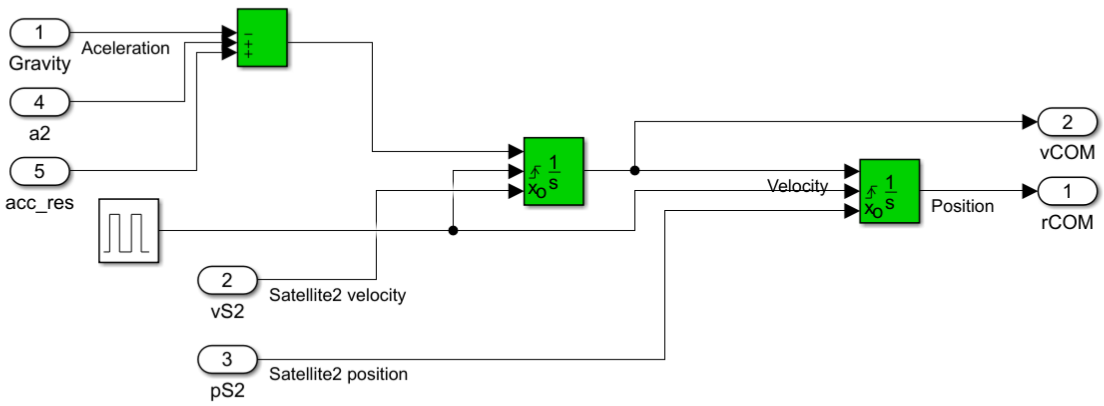

Figure 5.12: Orbit propagator with Error Correction - Orbit Dynamics

It is worth noticing that Figures 5.11 and 5.12 are referred to the orbit propagator of Satellite 2 which is embarked on board of Satellite 1, thus this orbit propagator exploits the same $\boldsymbol{a}_{res}$ computed for the Satellite 1 correction. In doing this operation we are therefore implicitly assuming that the errors committed by the two propagators are almost equivalent. It is for this reason in fact that it is possible to use the error made by the orbit propagator of Satellite 1 to correct also the propagation of motion of Satellite 2.
What has been said so far obviously applies in the same way to the model of Satellite 2, where will be present again the orbit propagators of both satellites. Here, the error existing between the real and propagated quantities of Satellite 2 is computed and then used to correct the propagated motion of Satellite 1.
As previously done for the other two versions, even in this case some simulated results are presented to make sure that the developed model is actually capable of accomplishing its task. At this purpose, Figures 5.13 and 5.14 report the plots of the difference between real and propagated velocity and position of Satellite 2. Making a comparison between these plots and those in Figures 5.8 and 5.9, it is possible to highlight the clear improvement introduced by the last modification. The following plots show a maximum absolute value of the error that is about an order of magnitude smaller than before, which implies a considerable upgrade in the computation of the satellite motion.
Further, looking at the figures, it is also possible to notice that, differently from the previous cases, in the long run the difference between real and propagated quantities begins to progressively decrease both in position and velocity. The simulations used to obtain the following figures were performed considering a simulation time of 100 orbits as for the previous cases.
Since this third variant of orbit propagators resulted to be the best in terms of performance, a new long-run simulation campaign was carried out with the aim to verify that the introduction of this last orbit propagator does not compromise the control system capability to fulfill its tasks.

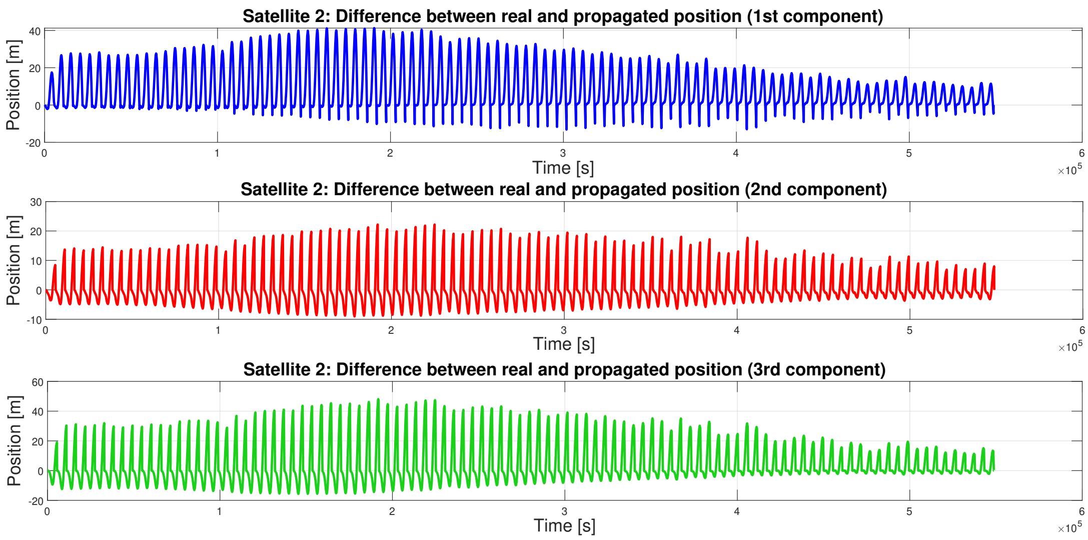

Figure 5.13: Difference between Real and Propagated Position of Satellite 2

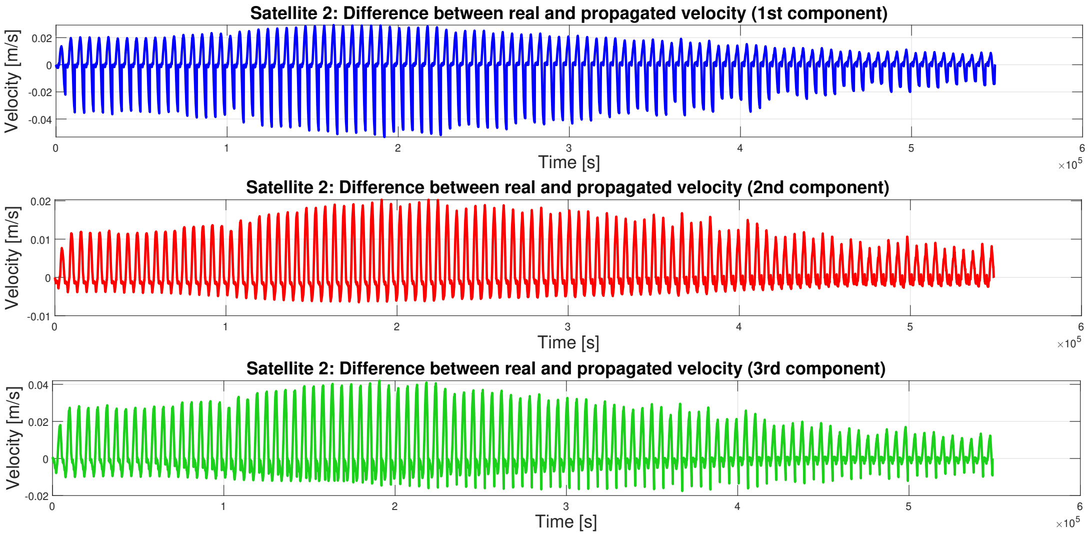

Figure 5.14: Difference between Real and Propagated Velocity of Satellite 2

5.4 Simulated Results

This section has the intent to collect and present the simulated results obtained from the long-run simulation campaign performed after the introduction of the third variant of orbit propagator described in Section 5.3. The configuration reported in Table 4.5 was taken into account for setting the parameters of the NMPC, since it places the simulation environment in the most realistic conditions possible by exploiting a gravity model composed by the 30th order of spherical harmonics.
For this new simulation campaign, the parameter to be changed among the different simulations is "PropagatorRT", which, as already mentioned, is the one related with the sampling time of measurements; it indicates the frequency with which the measurement data of the companion satellite becomes available on board of each spacecraft and consequently it is the parameter used to drive the update of the integrators initial conditions inside the orbit propagator. In order to account for the long sampling times of measurements needed because of the absence of a radio-frequency inter-satellite link, it was necessary to consider a value of "PropagatorRT" at least equal to one orbit. Consequently, the first simulation here reported makes use of a sampling time of measurement data equal to one orbital period, which implies PropagatorRT$= 5487$ s. All the tests were performed with a simulation time lasting for 2000 orbits.
In the following (Figures 5.15, 5.16 and 5.17), the behaviour of the first three state variables ρ_x, ρ_z and Δd of the IFC model, is presented with the aim to check the requirements on the formation lateral, radial and distance variations specified in Table 4.1 in terms of percentage with respect to the reference values of distance and altitude. In the same way as for the plots reported in the previous chapter, all the bounds imposed by the formation

requirements have been highlighted with green horizontal lines; in this way it is possible to make a comparison between these results and those obtained without orbit propagators (previously presented in Figures 4.32, 4.33 and 4.34).

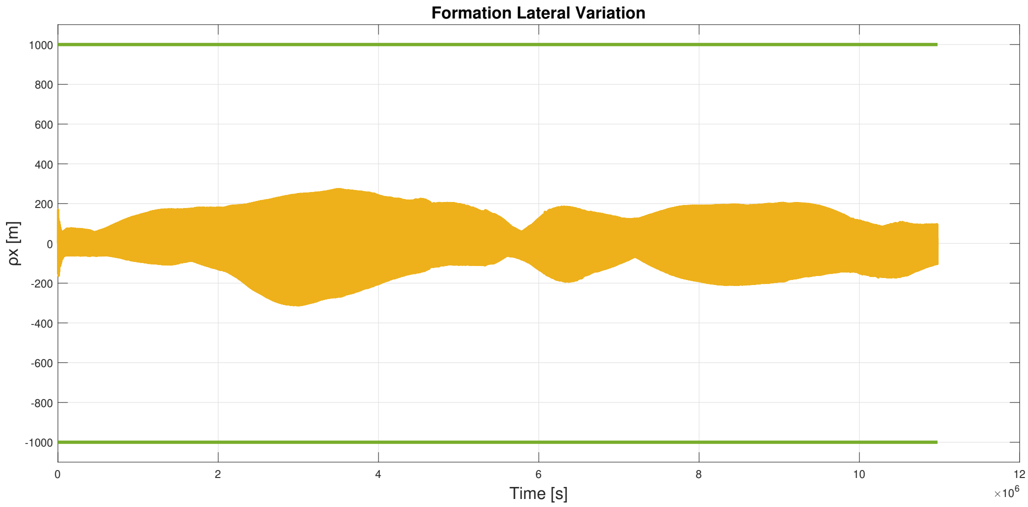

Figure 5.15: NMPC Configuration 4: Formation Lateral Variation with Orbit Propagators (PropagatorRT=1 orbit)

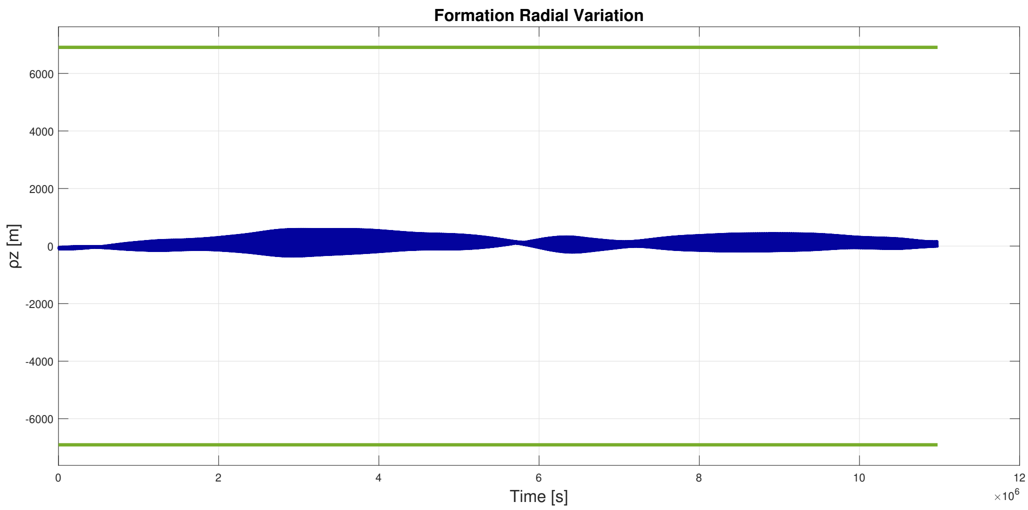

Figure 5.16: NMPC Configuration 4: Formation Radial Variation with Orbit Propagators (PropagatorRT=1 orbit)

By comparing the new plots with the ones reported in the previous chapter, it is possible to notice that the introduction of the orbit propagators inside the high-fidelity nonlinear model does not affect in any way the performance of the control system that remains able to fulfill its task despite the fact that it now receives input values that are partly supplied

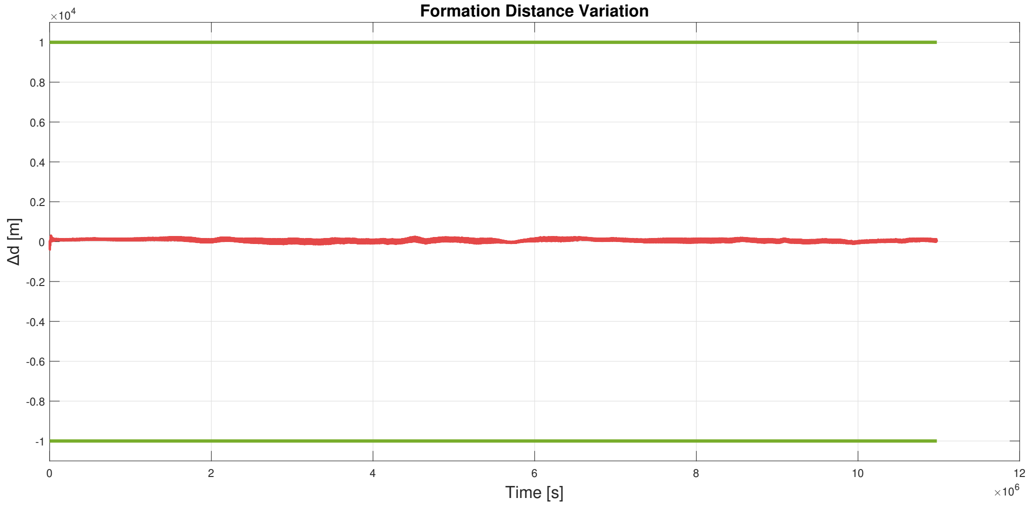

Figure 5.17: NMPC Configuration 4: Formation Distance Variation with Orbit Propagators (PropagatorRT=1 orbit)

by the propagator. This also prove once again that the developed model of orbit propagator well approximates the real satellite orbit, generating an error so small that it does not influence the behavior of the states in the least.
Moreover, the NGGM Satellite-to-Satellite distance shows the behaviour depicted in Figure 5.18 that, as it is evident, is very similar to the one obtained before the introduction of the orbit propagators.

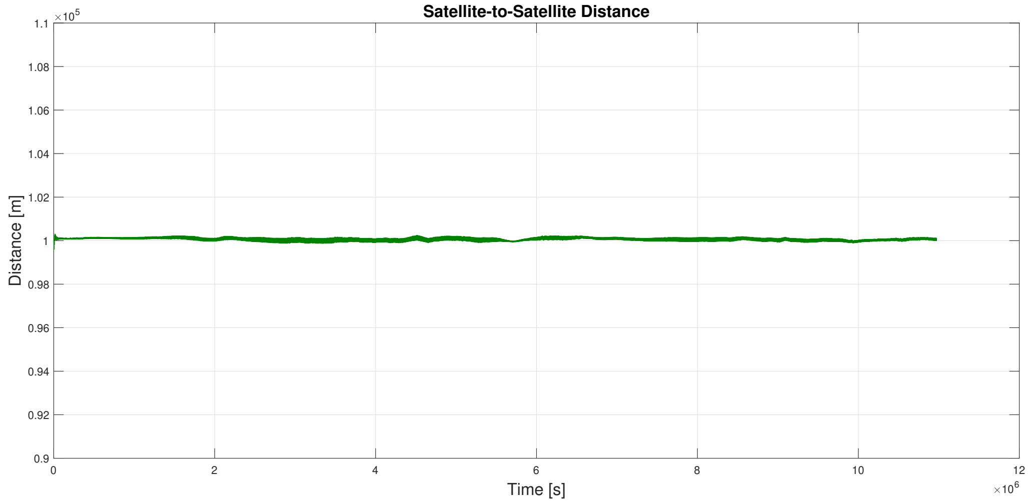

Figure 5.18: Satellite-to-Satellite Distance with Orbit Propagators (PropagatorRT=1 orbit)

After having verified that everything works well by using sampling times of measurements equal to one orbit, we can try to progressively increase the value of "PropagatorRT" until observing an evident performance degradation.

The plots shown below refer to a simulation carried out assuming a sampling time equal to 3 orbital periods, that implies PropagatorRT=3×5487 s. Again, in Figures 5.19, 5.20 and 5.21, the formation requirements on the first three perturbed states have been checked, showing the capability of the developed NMPC of still guaranteeing the orbit and formation long-term stability by maintaining limited the 'natural' fluctuations of these variables despite the increment of the sampling time of measurements.

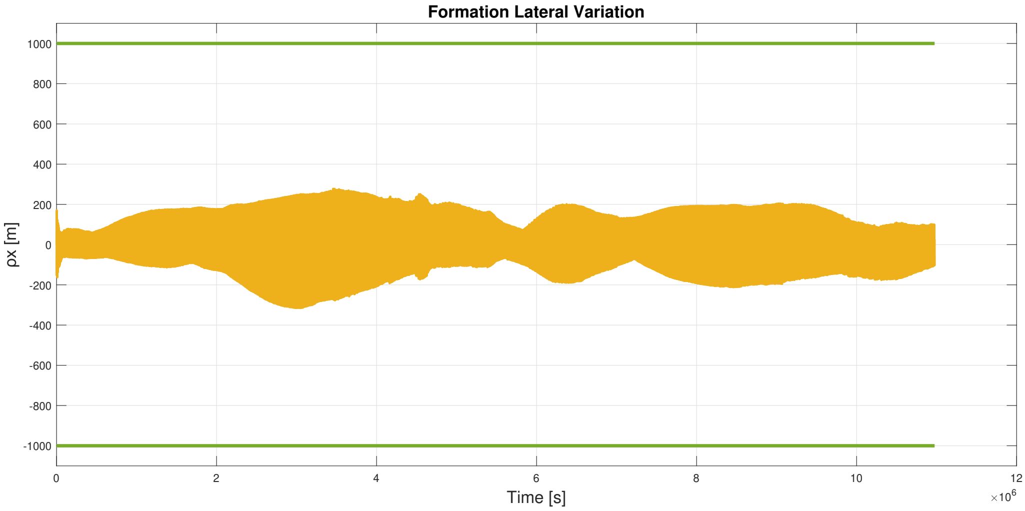

Figure 5.19: NMPC Configuration 4: Formation Lateral Variation with Orbit Propagators (PropagatorRT=3 orbit)

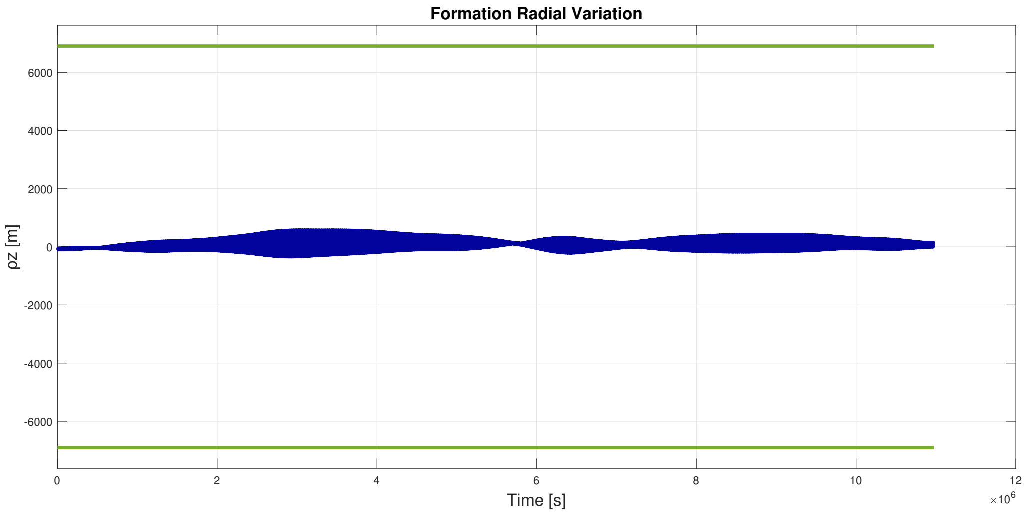

Figure 5.20: NMPC Configuration 4: Formation Radial Variation with Orbit Propagators (PropagatorRT=3 orbit)

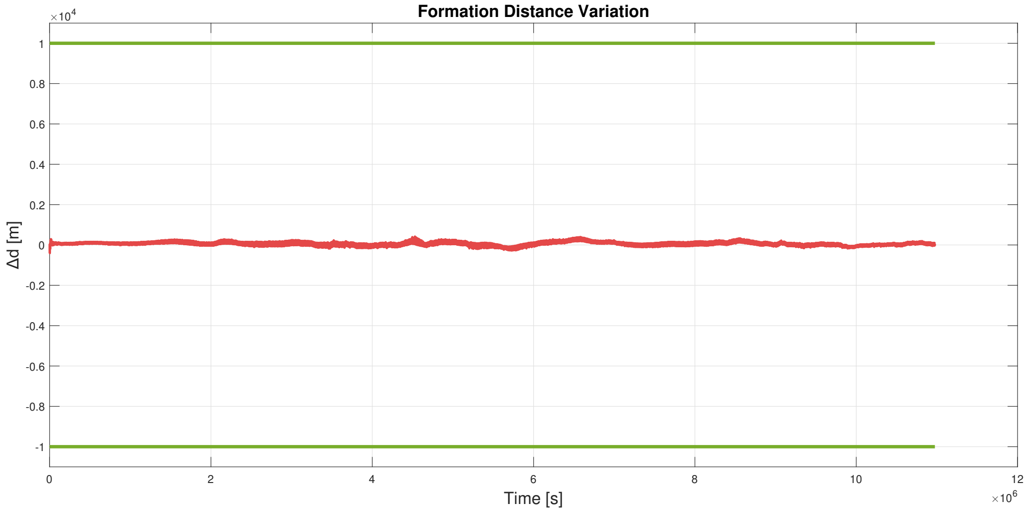

Figure 5.21: NMPC Configuration 4: Formation Distance Variation with Orbit Propagators (PropagatorRT=3 orbit)

Lastly, also in this case, we report below (Figure 5.22), the plot of the Satellite-to-Satellite Distance which is a further demonstration of the control system capability to maintain the formation stability despite the lack of measurement data for a longer time.

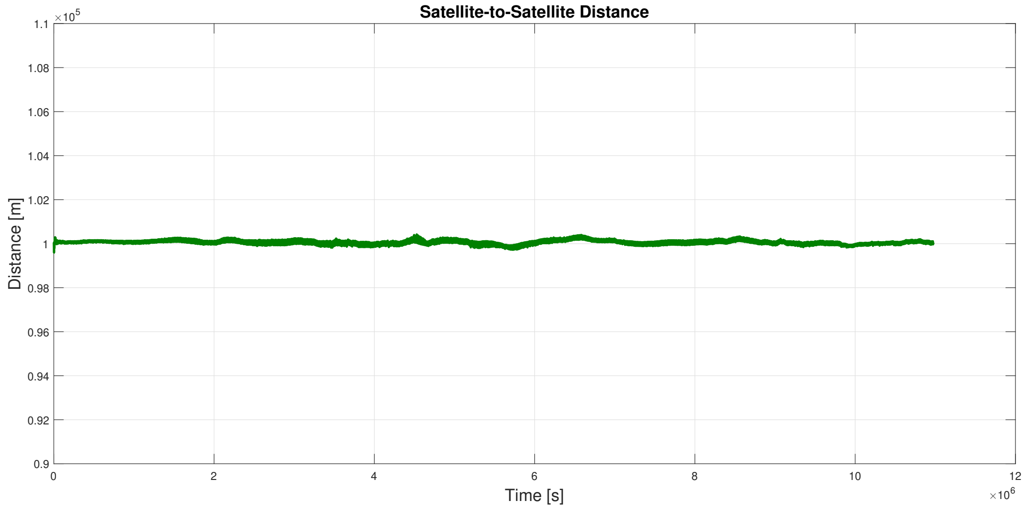

Figure 5.22: Satellite-to-Satellite Distance with Orbit Propagators (PropagatorRT=3 orbit)

During the simulation campaign an attempt was made to further increase the value of "PropagatorRT" by setting it equal to 5 orbits. For the sake of simplicity, we do not report here the obtained results which, however, continued to show the fulfillment of formation and stability requirements despite a bigger deterioration in performance.

Chapter 6

Conclusions and Future Work

To conclude this thesis work, let us now retrace what has been said in the previous chapters in order to draw some results. As mentioned at the beginning, the main objective of this research was to design, implement, and simulate an alternative orbit and formation control for a new type of gravimetric mission proposed by the European Space Agency after the successful studies conducted by GOCE and GRACE. The mission under assessment, namely the Next Generation Gravity Mission (NGGM), exploits two drag-free satellites flying in loose formation on a low-Earth orbit to accomplish its main task, that is the measure of the temporal variations of the Earth gravity field over a long time span. Within this background, a fully autonomous Nonlinear Model Predictive Control (NMPC) framework for orbit and formation control has been presented as alternative solution to the currently used Embedded Model Control, with the aim to explore the possibility of making improvements to the results obtained from the previous control strategy. In particular, for the development of the new NMPC-based control framework, the first thing to do was to look for the most suitable model to be used within the control algorithm for prediction purposes. Indeed, let's recall that the NMPC is an efficient and robust technique for model-based design which exploits an LTI model of the system to predict the future behaviour of the state variables and compute an optimal control action. In this context, such issue was addressed by comparing two possible LTI models, one based on the standard Hill-Clohessy-Wiltshire equations and the other one based on the Integrated Formation Control model. The first represents a model frequently used to analyse the relative motion of two spacecrafts in Earth-bound orbits while the second, specifically developed for the previous EMC-based orbit and formation control, involves a novel set of hill-type equations which allow the simultaneous description of both formation altitude and distance. From the comparison between the behaviour of the non-linear model, used to simulate the real plant, and that of the two LTI models mentioned so far, it emerged that the most suitable one for predictive purposes was the IFC model since it was able to guarantee a better approximation of the system dynamics. On the contrary, because of the too simplified assumptions made for development of the HCW equations, this model showed a very fast divergence of the spacecraft position from the nominal orbit, implying its inadequacy in describing the NGGM satellite formation system.

After having identified the IFC model as the most suitable one for the NMPC internal prediction, the control architecture has been designed with the aim to generate a control

input able to guarantee the stability of the satellite formation while meeting the demanding mission requirements defined by the NGGM science mode. Indeed, besides the constraints imposed on the formation variables, also the thruster saturation had to be taken into account. Thus, different NMPC configurations have been tested during the long-run simulation campaign with the aim to find the best trade-off between close-loop stability properties and capability of reducing the drag-free residual acceleration. As a matter of fact, it is worth to point out that a second important task of orbit and formation control consists in zeroing as much as possible the bias and drift of the drag-free residual accelerations. From the simulated results it emerged that the drag-free residual acceleration was directly proportional to the command action. As a consequence, in order to reduce as much as possible this quantity, it was necessary to use a very low thruster authority by imposing very stringent input constraints. Such stringent constraints, however, have made necessary to significantly reduce the sampling time which initially was set at a higher value in order to avoid interference with the wide-band drag-free control.
For each configuration, the presented simulated results have proven the capability of the designed NMPC control framework of ensuring the expected performances and the fulfilment of the main research objectives. In particular, the NMPC parameters written in Table 4.5, resulted to be the best trade-off for satisfying all the NGGM requirements in presence of a non-linear model that exploits the 30th order of spherical harmonics for the computation of the gravity potential.
The simulations carried out with this configuration have shown the effectiveness of the control strategy in guaranteeing the stability of NGGM formation, nevertheless some limitations and critical issues were still present. Specifically, the proposed NMPC configuration was able to reduce the drag-free acceleration till $35 \times 10^{-6}\ m/s^2$. This value is quite close to zero but since the purpose of this mission consists in the measure the Earth's gravity field, all non-gravitational contributions needs to be even more reduced. Moreover, it would be more appropriate to have a bigger sampling time in order to actuate the drag-free control and the orbit/formation control at different bands. As a result, future work should deal with the introduction of some improvements in the internal prediction model or in the parameterization of the command input in order to solve the still present criticalities which affect the developed control design. For example, it may be convenient to add to the model a filter chain after the state variables computation in order to clean the periodic orbital components from the differential navigation measurements and consequently avoid an extra-thrust authority. Moreover, other adjustments may concern the type of input parameterization used inside the NMPC control algorithm. For the proposed strategy a piece-wise constant input parametrization has been leveraged but one might think of developing a control with a polynomial parametrization.
The last part of this thesis was focused on the implementation of low-fidelity orbit propagators to be included inside the non-linear model with the aim to make the simulator even more realistic. The term "low-fidelity" refers to the fact that the novelty of these propagators consists in the ability to compute accurately the satellite orbit, despite being designed considering a low order gravity field and completely neglecting the other atmospheric disturbances. The need to include these devices on board of each spacecraft is due to the lack of information caused by the absence of a radio-frequency inter-satellite link and the long sampling time of the measurements data. The obtained results have proven the effectiveness of the orbit propagators mounted on board of each satellite of computing the position and

velocity information of the companion spacecraft. After having introduced these models inside the nonlinear simulator, another long-run simulation campaign has been performed showing the NMPC capability of guaranteeing long-term stability, although the lack of companion satellite information.
In conclusion, we have seen that the main advantage of using an NMPC control strategy consists in its ability to find an optimal control law managing at the same time state and input constraints and providing a real-time adaptation of the command input to the possible variations of process conditions. Nevertheless, although this research has shown the effectiveness of the proposed NMPC control strategy in achieving the NGGM formation objectives, it also emerged that this alternative strategy does not bring substantial improvements to the results obtained with the previous EMC-based one; on the contrary, the results obtained are quite similar proving that we are probably close to the maximum that can be achieved. In any case, the objective of making a contribution to the scientific phase of this mission by proposing a valid alternative strategy for the NGGM orbit and formation control has been reached. Indeed, the development of different possible alternatives is one of the main and necessary stages of the research phase of a real space mission.

Bibliography

[1] Klaus Abich et al. "In-Orbit Performance of the GRACE Follow-on Laser Ranging Interferometer". In: *Phys. Rev. Lett.* 123 (3 July 2019), p. 031101.

[2] F Allgöwer, Rolf Findeisen, and Z K Nagy. "Nonlinear model predictive control: From theory to application". In: *J. Chin. Inst. Chem. Engrs* 35 (May 2004), pp. 299–315.

[3] Peter Bender, D Wiese, and R Nerem. "A possible Dual-GRACE mission with 90 degree and 63 degree inclination orbits". In: Noordwijk, The Netherlands: ESA, 2008.

[4] Enrico Canuto. "Embedded Model Control: Outline of the theory". In: *ISA Transactions* 46.3 (2007), pp. 363–377.

[5] Enrico Canuto et al. "Orbit and formation control for low-earth-orbit gravimetry drag-free satellites". In: *Proceedings of the Institution of Mechanical Engineers, Part G: Journal of Aerospace Engineering* 229.7 (Sept. 2014), pp. 1194–1213.

[6] Enrico Canuto et al. "Satellite-to-satellite attitude control of a long-distance spacecraft formation for the Next Generation Gravity Mission". In: *European Journal of Control* 18 (Apr. 2015).

[7] Enrico Canuto et al. *Spacecraft Dynamics and Control.* Elsevier, 2018.

[8] Stefano Cesare et al. "The European way to gravimetry: From GOCE to NGGM". In: *Advances in Space Research* 57.4 (Feb. 2016), pp. 1047–1064.

[9] L Colangelo et al. "Orbit and Formation Control for the Next Generation Gravity Mission". In: *IFAC-PapersOnLine* 49.17 (2016), pp. 284–289.

[10] Luigi Colangelo. "Spacecraft Formation Control for the Next Generation Gravity Mission". PhD thesis. Politecnico di Torino, 2017.

[11] Luigi Colangelo et al. "Embedded model control GNC for the Next Generation Gravity Mission". In: *Acta Astronautica* 140 (2017), pp. 497–508.

[12] Assessment of satellite constellations for monitoring the variations in earth gravity field. Tech. rep. 4000108663/13/NL/MV. University of Stuttgart, Institute of Geodesy, Dec. 2015.

[13] Rolf Findeisen and Frank Allgöwer. *An Introduction to Nonlinear Model Predictive Control.* Jan. 2002.

[14] Willi Freeden, Volker Michel, and Helga Nutz. "Satellite-to-satellite tracking and satellite gravity gradiometry (Advanced techniques for high-resolution geopotential field determination)". In: *Journal of Engineering Mathematics* 43.1 (2002), pp. 19–56. ISSN: 1573-2703.

[15] Roger Haagmans et al. "ESA's next-generation gravity mission concepts". In: *Rendiconti Lincei. Scienze Fisiche e Naturali* 31 (Jan. 2020).

[16] G Heinzel et al. "LISA interferometry: recent developments". In: *Classical and Quantum Gravity* 23.8 (Mar. 2006), S119–S124.

[17] Jean-Pierre Marque, Bruno Christophe, and Bernard Foulon. "Accelerometers of the GOCE Mission: Return of Experience from One Year of In-Orbit". In: *ESA Living Planet Symposium*. Ed. by H. Lacoste-Francis. Vol. 686. ESA Special Publication. Dec. 2010, p. 57.

[18] Sergio Mottini et al. "Laser metrology for a next generation gravimetric mission". In: *International Conference on Space Optics — ICSO 2008*. Ed. by Josiane Costeraste, Errico Armandillo, and Nikos Karafolas. Vol. 10566. International Society for Optics and Photonics. SPIE, 2017, pp. 450–458.

[19] B S Sheard et al. "Intersatellite laser ranging instrument for the GRACE follow-on mission". In: *Journal of Geodesy* 86.12 (2012), pp. 1083–1095. ISSN: 1432-1394.

Acknowledgements

At the end of this thesis, I would like to extend my sincere acknowledgment to all those people who, directly or not, have supported me in my university journey. First of all, I would like to express my deepest appreciation to my supervisor Prof. Carlo Novara and the Eng. Sabrina Dionisio who gave me the opportunity to work on a topic that fully reflects my interests, merging my passions for control systems and aerospace applications. Thanks to their help and availability I could take part to this project in collaboration with Thales Alenia Space, and develop new knowledge in this fascinating research field that I hope to be able to deepen in my future working.
Secondly, I am ineffably indebted to my co-supervisors Carlos and Mattia, since without their active guidance, cooperation and encouragement it would have been impossible to make progress on this ambitious project. I am grateful for all the theoretical explanations and the practical tips they provided me during these months. Despite the distance caused by the pandemic, I have always been able to count on their presence and their excellent suggestions.
The sincerest acknowledgment goes to my parents, who allowed me to grow and empower myself, accepting to keep me away from home but always supporting me with their constant presence, capable of being felt even from miles away. Behind the scenes of this path, invisible but fundamental, there is the trust that they have responded in me, holding my hand every time I needed it and letting me walk alone on my way as soon as I felt ready.
Last but not least, my gratitude goes to all the friends who have been by my side over these years, in particular to those met in Turin who have been able to lighten the endless days of study and make more fun the discovering of this wonderful city that today I consider as a second home thanks also to their contribution.
This moment marks the end of an amazing experience, but it is also the beginning of a future waiting to be discovered. I look forward to embracing new challenges with the same commitment and dedication that have always distinguished me.

Thank you all,
Patrizia